Image analysis methods for dynamic hepatocyte-specific contrast enhanced MRI

Zhang, Tian

DOI
10.4233/uuid:0af59938-45cc-444d-bd62-289a662f854d

Publication date
2019

Document Version
Final published version

Citation (APA)
Zhang, T. (2019). *Image analysis methods for dynamic hepatocyte-specific contrast enhanced MRI*. [Dissertation (TU Delft), Delft University of Technology]. https://doi.org/10.4233/uuid:0af59938-45cc-444d-bd62-289a662f854d

Image Analysis Methods for Dynamic Hepatocyte-specific Contrast Enhanced MRI

IMAGE ANALYSIS METHODS FOR DYNAMIC HEPATOCYTE-SPECIFIC CONTRAST ENHANCED MRI

Proefschrift

ter verkrijging van de graad van doctor
aan de Technische Universiteit Delft,
op gezag van de Rector Magnificus prof. dr. ir. T.H.J.J. van der Hagen,
voorzitter van het College voor Promoties,
in het openbaar te verdedigen op woensdag 20 maart 2019 om 15:00 uur

door

Tian ZHANG

Master of Engineering in Optical Engineering
Zhejiang University, Hangzhou, China
geboren te Jiangsu, China.

Dit proefschrift is goedgekeurd door de

promoters: Prof. dr. ir. L. J. van Vliet, Prof. dr. J. Stoker and Dr. F. M. Vos
copromoters: Dr. C. Lavini

Samenstelling promotiecommissie:

Rector Magnificus,	voorzitter
Prof. dr. ir. L. J. van Vliet,	Technische Universiteit Delft
Prof. dr. J. Stoker,	Academisch Medisch Centrum Amsterdam
Dr. F. M. Vos,	Technische Universiteit Delft
Dr. C. Lavini,	Academisch Medisch Centrum Amsterdam
Onafhankelijke leden:	
Prof. dr. ir. J. W. van Wingerden	Technische Universiteit Delft
Prof. dr. ir. M.J.P. van Osch	Leiden University Medical Center
Dr. M. Staring	Leiden University Medical Center
Dr. S. Sourbron	University of Leeds
Prof. dr. A.M. Vossepoel	Technische Universiteit Delft, reservelid

The work in this dissertation was conducted at the Quantitative Imaging Group (QI), Faculty of Applied Sciences, Delft University of Technology.

Printed by: Ridderprint BV

ISBN 978-94-6375-351-7

An electronic version of this dissertation is available at
http://repository.tudelft.nl/.

CONTENTS

SUMMARY

Patients with colorectal cancer are frequently presented with liver metastases for which (partial) resection is often the best therapy. However, the future remnant liver, the remaining part of the liver after resection, should allow adequate liver function to avoid liver failure. This thesis presents novel methods for the accurate voxel-wise estimation of the future remnant liver's function based on pharmacokinetic modeling of dynamic contract-enhanced (DCE) MRI.

The methods comprise a variety of novel techniques for DCE-MRI of the liver: 1) 4D registration of the DCE series; 2) delineation of the liver, the liver vasculature and the liver's anatomical segments; 3) pharmacokinetic (PK) modeling of the perfusion based on the intra-cellular contrast agent Gd-EOB-DTPA (Primovist); 4) assessment of the relation between DCE-MRI and hepatobiliary scintigraphy (HBS).

Spatial alignment of the voxels in the 4D DCE-MRI is an important requirement for PK modeling. We exploit the proximity of deformation fields to sequentially register images in an ordered fashion. The global liver displacement helps in predicting the deformation 'tendency' along the time axis. The deformation tendency allows us to obtain a better starting point for the registration. Such a method aims to start the registration optimization close to the optimum and avoid getting trapped in a local minimum.

We apply a liver-specific contrast agent, due to which the liver shows a higher signal intensity than the surrounding organs. Maximal contrast is achieved by subtracting the registered first image of the series from the last image. Subsequently, the liver is delineated based on the resulting "contrast" volume by means of a level set approach. For identifying the liver vasculature, a region growing method is applied to identify the hepatic vein (HV), the portal vein (PV) and inferior vena cava (IVC) from the liver. Differing from conventional region growing methods, it calculates the Pearson correlation between the time intensity curves (TICs) of a seed and all voxels and regards the correlation as a distance measurement. After the identification of the liver vasculature, skeletons of the vessels are regarded as landmarks to partition functional liver segments. Finally the liver partitioning is achieved according to the Couinaud classification.

We propose an improved pharmacokinetic model, which we named COS-FLAC to assess the liver DCE MRI data. Two novelties are introduced in the PK modeling. First, the arterial input function proposed by Orton is integrated into Sourbron's dual inlet PK model. This enables that the arrival times of contrast from the portal vein and the hepatic artery are separately included in the model and estimated simultaneously with the PK model parameters. Secondly, the deformation and displacement of the liver is estimated and used to correct for changes in signal intensity such as the ones caused by B_1-inhomogeneities.

Finally, DCE-MRI perfusion parameter liver uptake rate (Ki) derived from our COS-FLAC model is correlated with the liver's uptake rate of ^{99m}Tc-mebrofenin (MUR) in HBS. Strong correlations are found between uptake parameters derived from DCE-MRI and HBS for both total and FRL function (Pearson $r = 0.70$, $P = 0.001$ and $r = 0.89$, $P < 0.001$

respectively). There is a strong agreement between the functional share determined with both modalities (ICC = 0.944, 95%-CI: 0.863-0.978, n = 20). There is a significant negative correlation between liver aminotransferases and bilirubin for both MUR and Ki. The results indicate that DCE-MRI with Gd-EOB-DTPA has the potential to measure similar functional information in the liver as HBS with ^{99m}Tc-mebrofenin.

1

INTRODUCTION

1

1.1. THE LIVER

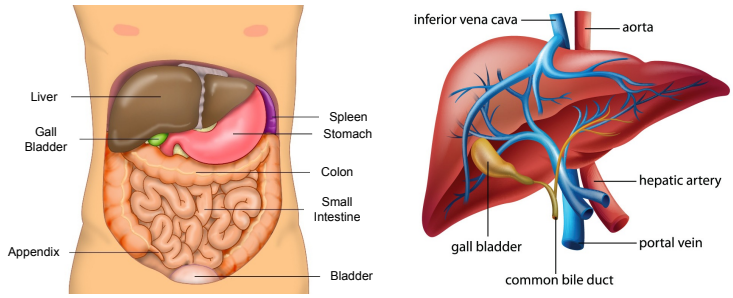

(a) (b)

Figure 1.1: (a) Abdominal anatomy [1]; (b) The blood supply of the liver [2].

THE liver is the largest gland in the human body and normally weighs 1.44–1.66 kg [3]. It is located in the right upper quadrant of the abdominal cavity, below the diaphragm, and partially hidden behind the rib cage. The liver is surrounded by multiple vital organs, including the stomach that lies on its left, the gallbladder is just below the edge of the liver, and the small and large intestines travel along its lower border, see Fig. 1.1(a). The liver consists of two parts, a bigger right lobe and a smaller left one, see Fig. 1.1(b).

The liver is responsible for several important functions, including but not limited to detoxification, converting substances, storage, and production of essential proteins for body functioning. It produces bile that helps with fat digestion, has a very important role in immunity, and produces clotting factors to prevent bleeding [4].

A difference that distinguishes liver from other organs is its unique blood supply; see Fig. 1.1(b). Particularly, the liver receives blood from the hepatic artery and hepatic portal vein. The hepatic artery carries oxygen-rich blood from the aorta, whereas the portal vein carries blood rich in digested nutrients from the entire gastrointestinal tract and also from the spleen and pancreas. The portal vein supplies approximately 75% of the liver's blood.

Because of its rich, dual blood supply, the liver is a common site for metastatic disease. Liver metastases often arise from primary tumors in organs such as colon, breast, lung, pancreas and stomach [5]. Computed tomography (CT) [6] is clinically used to determine the presence/absence of hepatic metastases and provide a gross estimate of liver tumor burden due to its wide availability and high scan efficiency. However, magnetic resonance imaging (MRI) using liver-specific contrast media is increasingly performed in patients with known hepatic malignancy (primary or secondary) when liver resection is being considered [7]. Dynamic contrast-enhanced (DCE) MRI enables accurate identification of the number and locations as well as characterization of liver metastases [8]. As such, surgeons can determine whether the patient is suitable to receive a liver resection.

Liver diseases and cancers may have a large influence on liver function which is important information for the surgeon. Several methods have been proposed to evaluate the liver function. Conventional tests include but are not limited to the Child-Pugh Score [9, 10], ICG (Indocyanine Green) Clearance test [11], ^{99m}Tc-GSA (Galactosyl Serum Albumin) Scintigraphy [12] and the ^{99m}Tc-mebrofenin Hepatobiliary Scintigraphy [13]. A limi-

tation of the aforementioned methods is that they can only evaluate the total liver function and some of them even rely on ionizing radiation. Recently, DCE-MRI with Gd-EOB-DTPA (a gadolinium based, liver specific contrast agent) has been proposed as a useful test to assess liver function, offering liver function test without radiation burden [14–17].

1.2. MAGNETIC RESONANCE IMAGING (MRI)

1.2.1. SPIN DYNAMICS

MAGNETIC resonance imaging is a medical imaging technique used in radiology to form images of the anatomy and of the physiological processes of the body in both health and disease [18]. Essentially, MRI is based on the fact that in an external magnetic field, the intrinsic angular momentum (spin) of a (Hydrogen) proton precesses at the "Larmor frequency" [19] around the external magnetic field's main axis. The Larmor frequency is proportional to the magnitude of the external field [20] and in the case of MRI lies in the range of radio frequency (about 10-300 MHz, according to the applied magnetic field). The spins will resonate when they are subjected to an oscillating electromagnetic field of the same frequency as their Larmor frequency. From a macroscopic perspective, the magnetization vector will tip away from the external magnetic field axis by a certain flip angle α, where the time-integral of the amplitude of the RF-pulse determines the size of the flip angle.

The transverse component of the precessing spins generate an oscillating electromagnetic field, which, according to Faraday's law of induction, can induce an electromotive force in a receive coil placed nearby. Before applying the RF-pulse, the transverse components of the spins have an arbitrary phase, and as a result, the transverse components of the net magnetization are zero, i.e. no signal is detected. After the RF-pulse is applied, the net transverse magnetization is no longer zero, which means a signal can be detected.

1.2.2. T_1, T_2 AND T_2^* RELAXATION TIMES

After spins have been excited by an RF-pulse, they will gradually relax back to their equilibrium state. Three independent mechanisms are involved in this process. First, energy is exchanged between the hydrogen nuclei and their surroundings (the "lattice"). This process is called spin-lattice interaction [21]. From a macroscopic perspective, this mechanism causes the longitudinal component of the net magnetization M_z to recover to equilibrium in an exponential fashion. A time constant known as T_1-relaxation time characterizes this recovery, which is defined as the time it takes for the longitudinal magnetization to recover approximately 63% [1-(1/e)] of its initial value after being flipped into the magnetic transverse plane by a 90° radiofrequency pulse.

Second, the spins also exchange energy among each other. This process is called spin-spin interaction [21]. It causes the relative phase of individual nearby spins to disperse, which results in the transverse components of the net magnetization M_{xy} decaying to zero. This is again an exponential process, characterized by the T_2-relaxation time. i.e. the time it takes for the magnetic resonance signal to irreversibly decay to 37% (1/e) of its initial value after tipping the longitudinal magnetization towards the magnetic transverse plane by a 90° radiofrequency pulse.

Third, spins may experience static fluctuations in magnetic field strength, due to global

variation in the B_0 field, or susceptibility effects. As a consequence, these spins will precess with a slightly varying frequency. Similar to the spin-spin interaction, this causes the individual spins to dephase, again resulting in an exponential decay of the transverse magnetization. This is characterized by the relaxation time T_2'. Since the T_2 and T_2' effects both affect the transverse magnetization, they are often combined into one value known as ${T_2}^*$:

$$\frac{1}{{T_2}^*} = \frac{1}{T_2} + \frac{1}{T_2'} \tag{1.1}$$

1.2.3. TYPICAL MRI SCANNER AND SEQUENCES

If the external field is made to spatially vary along one or more dimensions, then the Larmor frequencies of the proton spins in the object are, in turn, spatially varying. This principle enables the localization of the spins by means of frequency-based spatial-encoding. As such, it is possible to visualize the internal structures of bodies in a non-invasive manner based on the fact that different tissues in the body have different T_1 and T_2 relaxation times. With this idea, Lauterbur and Mansfield acquired the first MR image in 1973 [21] and were awarded the Nobel Prize in 2003 for their discoveries concerning "magnetic resonance imaging" [22].

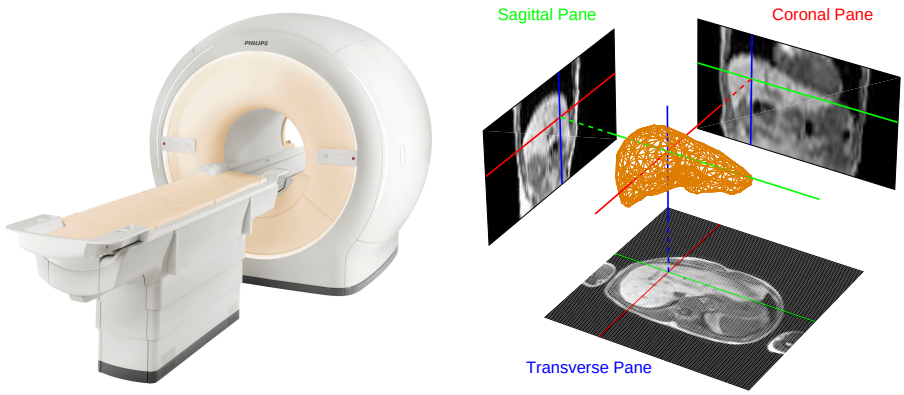

(a) (b)

Figure 1.2: (a) A typical MRI scanner [23]; (b) T_1-weighted MR images of the liver in three orthogonal planes.

A typical clinical MRI scanner is based on the aforementioned idea. It consists of a large superconducting magnet (usually cylindrical) with a radiofrequency generating system and magnetic field gradient coils as represented in Fig. 1.2(a). Inside the tunnel various coils can be placed to receive the signal generated by the body in response to the applied radiofrequency. Unlike Computed Tomography (CT), which makes use of X-rays, MRI only adopts electromagnetic waves at low, non-ionizing energies to acquire the image, and as such does not expose patients to ionizing radiation.

The timing and order of applying RF-pulses, applying gradient fields, and reading the MR signal, is called a sequence. The gradient echo sequence (described below) is one of

the most basic sequences, and can provide images whose contrast depends on the local Proton Density (PD), T_1 and ${T_2}^*$. The amount of T_1 and ${T_2}^*$ weighting can be chosen by simply tuning the repetition time and echo time of the sequence, respectively.

The Fast Spoiled Gradient Echo (FSPGR) sequence (also known as T_1 weighted Fast Field Echo - FFE, or Fast Low Angle Shot – FLASH on scanners from different manufacturers) is a fast sequence that produces T_1 weighted images. The FSPGR sequence is a gradient echo sequence with very short T_R and T_E (in the order of several ms) where, before each RF-pulse is applied, any transverse magnetization remaining from the previous repetition is removed, or 'spoiled'. This is done by either applying a gradient, which dephases the spins, or by applying each successive RF-pulse in a randomized direction, which prevents build-up of transverse magnetization.

After a number of repetitions, the recovery of the longitudinal magnetization via the T_1 relaxation process is exactly countered by the reduction of the longitudinal component caused by the application of the RF-pulse. This is called the steady state case, during which the signal generated by the spins is given by:

$$S = N \sin(\alpha) \frac{1 - \exp(-T_R/T_1)}{1 - \cos(\alpha)\exp(-T_R/T_1)} \exp\left(-T_E/T_2^*\right) \tag{1.2}$$

This sequence has a very short repetition time, and therefore facilitates a high temporal resolution. For this reason, and for its T_1-weighting, the FSPGR sequence is commonly used for Dynamic Contrast Enhanced MRI. Typical MR images acquired on a 3T MRI scanner via a 3D FSPGR sequence can be seen in Fig. 1.2(b).

1.3. DYNAMIC CONTRAST ENHANCED MRI

OVER the past decades, Dynamic Contrast Enhanced MRI (DCE-MRI) has been widely used for assessing properties of the perfusion in organs. DCE-MRI starts with an intravenous injection of a contrast agent. After that, a series of 3D T_1-weighted images is acquired in several minutes, resulting in a 3D+t dataset. The time-dependent change in the measured signal intensity determined by the contrast agent is used as an indicator for tissue integrity.

1.3.1. CONTRAST AGENTS

The contrast agents used for DCE-MRI are gadolinium-based; they consist of a molecule (the chelate) encapsulating an otherwise toxic gadolinium ion. The strongly paramagnetic gadolinium ion can interact with the hydrogen contained in a water molecule and shortens the spin-lattice (T_1) relaxation time. When applying a suitable T_1-weighted imaging sequence, this process leads to an increase of the signal intensity in the tissues where the gadolinium has leaked and, hence, to an increase of the image contrast of certain tissues [24]. Common contrast agents used in DCE-MRI can be seen in Table 1.1 [25].

Most contrast agents in Table 1.1 are gadolinium-based contrast agents (GBCA) that are excreted by glomerular filtration in the kidneys instead of hepatobiliary system to a large extend. For example, Gd-BOPTA has a predominantly renal excretion (95%-97%) and low hepatobiliary excretion (3%-5%). Alternatively, Gd-EOB-DTPA, a liver-specific GBCA,

[1] In Europe it is named Primovist, and Eovist in the USA.

Table 1.1: Common contrast agents.

Trade Name	Generic Name	Acronym	Manufacturer
Gadovist	Gadobutrol	Gd-DO3A-butrol	Bayer
Primovist / Eovist[1]	Gadoxetic acid, disodium	Gd-EOB-DTPA	Bayer
Resovist	Ferucarbotran	SH U 555 A	Bayer
Prohance	Gadoteridol	Gd-HP-DO3A	Bracco
Multihance	Gadobenate dimeglumine	Gd-BOPTA	Bracco
Dotarem	Gadoterate meglumine	Gd-DOTA	Guerbet

has 50% hepatocytic uptake and biliary excretion in the normal liver [14]. It can not only diffuse in the extracellular space but also is actively transported into functioning hepatocytes and subsequently excreted into the bile [15]. The hepatocyte uptake and biliary excretion of Gd-EOB-DTPA mainly occur via the organic anion transporting polypeptides OATP1B1 and OATP1B3 located at the sinusoidal membrane and the multidrug resistance-associated proteins MRP2 at the canalicular membrane, respectively. Such characteristics make that Gd-EOB-DTPA behaves similarly to non-specific GBCA during the initial dynamic phase, and adds substantial information during the hepatobiliary phase, improving the detection and characterization of focal liver lesions and diffuse liver disease. In summary, the advantages of Gd-EOB-DTPA-enhanced MR imaging include absence of ionizing radiation, combined anatomical and functional assessment, and the ability to quantitatively assess hepatic perfusion and function [16][17]. For this reason, Gd-EOB-DTPA (Primovist® Bayer B.V., Mijdrecht, The Netherlands) is applied in this thesis.

1.3.2. HOW DCE-MRI WORKS

In Fig. 1.3 it is shown how, for each voxel in the Field of View (FOV), the signal intensity is plotted as a function of time, generating what is known as the Time Intensity Curve (TIC). The TIC reflects how the concentration of the contrast agent in the image voxels (tissue) changes following its delivery through the blood supply. Different profiles of TICs correspond to different physiological properties of tissues. Several enhancement types of TIC have been observed, see Fig. 1.4 [26]. A more comprehensive study of TICs can be done by applying proper pharmacokinetic models, in which the parameters to estimate reflect physiological properties of tissues.

Pharmacokinetic modeling is a mathematical modeling technique for predicting the absorption, distribution, metabolism and excretion (ADME) of synthetic or natural chemical substances in humans and other animal species. In DCE-MRI, it refers to formulating a model that describes how the MRI signal changes as a result of the tissue's reaction to the contrast agent. Quantitative parameters that are directly related to the intrinsic physiological properties of tissues can be extracted when fitting the pharmacokinetic model to the measured DCE-MRI data, i.e. TICs in the organs being studied. Generally speaking, the complete model includes a physiological (pharmacokinetic) component (e.g. how the contrast agent behaves in the tissues), and a physical component (i.e., how the contrast agent affects the MRI signal). Several pharmacokinetic models haven been proposed to model various tissue types, different organs, and types of contrast agent [27].

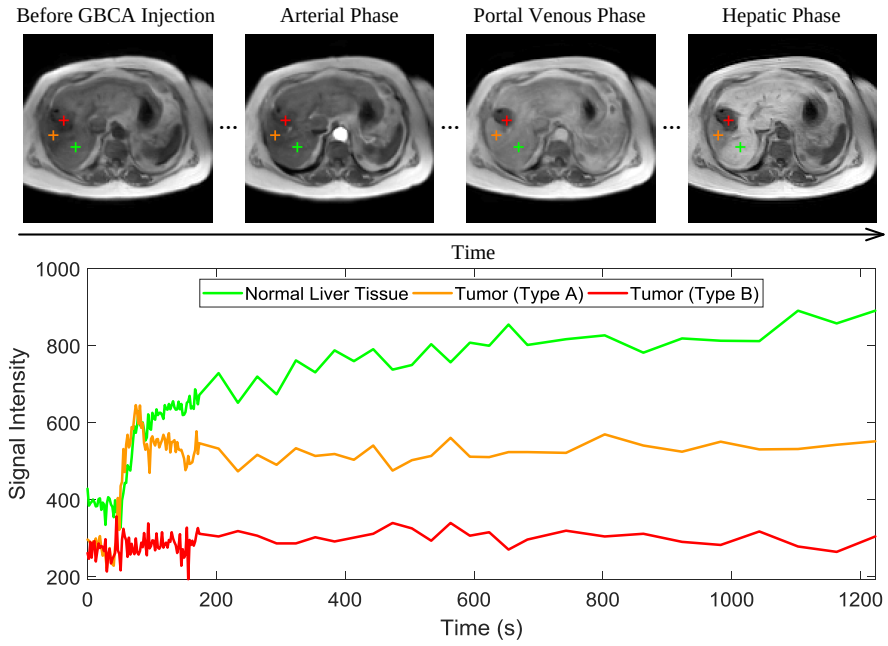

Figure 1.3: Different TIC profiles of healthy liver tissue and liver tumors.

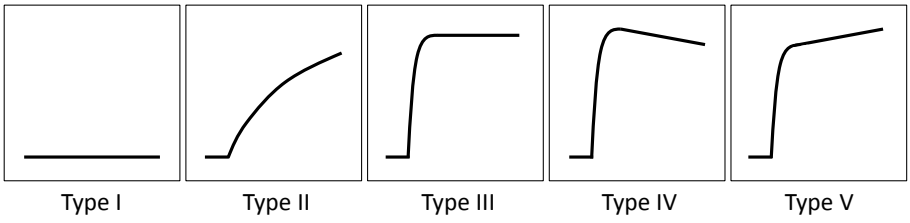

Figure 1.4: Diagram shows classification for subjective assessment of time–signal intensity curves: Type I, no enhancement; Type II, gradual increase of enhancement; Type III, rapid initial enhancement followed by a plateau phase; Type IV, rapid initial enhancement followed by a washout phase; And type V, rapid initial enhancement followed by sustained late enhancement.

1.3.3. DCE-MRI OF THE LIVER

In contrast to all other organs, DCE MRI of the liver can be done with a specially developed Gd-based contrast agent that, contrary to all the other Gd-contaning contrast media, is metabolized by the cells. The dynamics of these liver specific contrast agents in the liver differs therefore from those in all other organs.

In Fig. 1.3, the TIC of healthy liver tissue (the green line) shows a rapid initial enhancement followed by sustained late enhancement, which reflects that Gd-EOB-DTPA molecules leak into the extravascular-extracellular space (EES) and then are taken up by hepatocytes. However, the TIC of liver tumor type A (the orange line) shows an initial fast

uptake, then followed by no uptake in the hepatocytes. This profile indicates that the tumor might be highly vascularized. Moreover, the TIC of liver tumor type B (the red line) shows only very limited signal enhancement, which implies the tissue in the tumor does not take up the contrast agent.

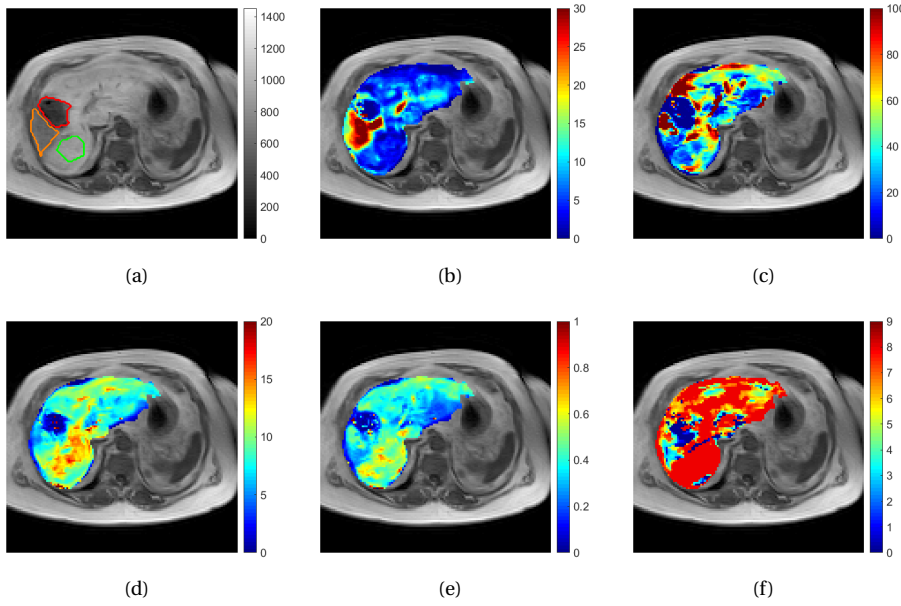

Figure 1.5: (a) A post-contrast DCE-MR image with three region of interest (ROI) delineated, which represent healthy liver tissue (green), tumor type I (orange) and type II (red), respectively. (b)-(f) represent PKM parameter maps which are overlaid on image (a). (b) and (c) are F_A and F_V, i.e. the arterial and venous plasma flows, respectively (in milliliters per minute per 100 mL). (d) shows K_I, the liver uptake rate (in per minute). (e) represents extravascular extracellular compartment K_I (in milliliters per 100 mL). (f) stands for T_A, the time delay of the Gd-EOB-DTPA's arrival between in the aorta and liver (in second).

Table 1.2: Values of measured parameters for healthy liver tissue and tumors. The numbers present the mean value and the standard deviation (std).

	Normal liver tissue	Tumor type I	Tumor type II
F_A (ml/min/100ml)	3.814 (0.882)	25.054 (5.529)	11.148 (12.311)
F_V (ml/min/100ml)	38.502 (11.229)	70.617 (65.428)	5.683 (14.948)
K_I (/100/min)	12.123 (1.973)	7.933 (1.827)	3.368 (2.841)
V_E (ml/100ml)	0.526 (0.059)	0.354 (0.077)	0.201 (0.157)
T_A (sec)	7.934 (2.359E-14)	4.623 (1.807)	3.047 (3.253)

With the help of pharmacokinetic modeling, TICs such as in Fig. 1.3 can be modeled and several pharmacokinetic model (PKM) parameters are estimated. Here the same DCE-MR image as in Fig. 1.3 is adopted for illustration; see Fig. 1.5(a). Besides, Fig. 1.5(a)

- 1.5(f) show all the parameters that a liver PKM is able to estimate.

In order to quantitatively assess perfusion and function with Gd-EOB-DTPA, three regions of interest (ROI's) including different type of tissues are manually delineated in Fig. 1.5(a). Mean and standard derivation values of each perfusion parameters are summarized in Table 1.2. Significant difference between the normal liver tissue and tumors regarding each perfusion parameter is observed.

1.3.4. STUDY PROTOCOL

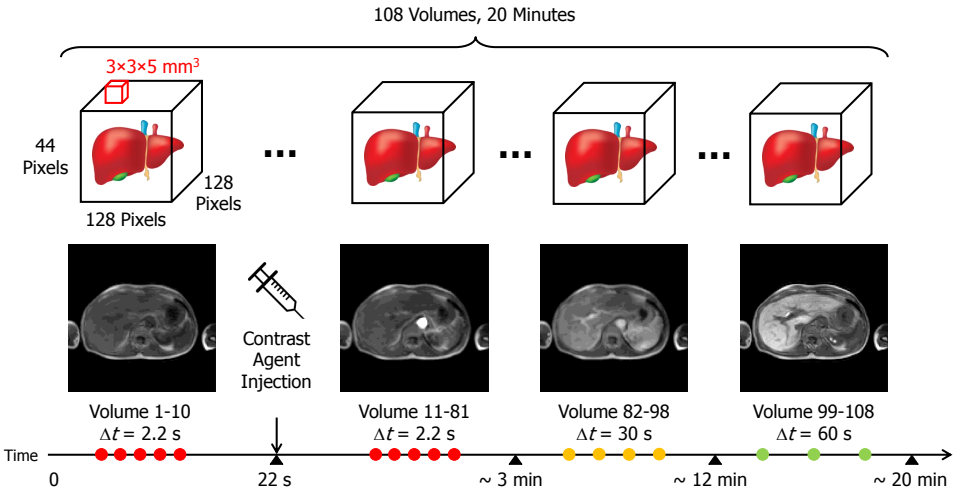

Figure 1.6: The DCE-MRI scanning protocol in our project.

The DCE-MRI scanning protocol of our project is illustrated in Fig. 1.6. Our data were acquired on a 3T Philips Ingenia whole-body scanner (Philips Healthcare, Best, The Netherlands) via a 3D FSPGR (or T_1-w FFE) sequence. The acquisition parameter settings were T_E/T_R = 2.3/3.75 ms, FA = 15°, matrix size = 128×128×44, voxel size = 3×3×5 mm^3, acquisition time = 2.141 s for each volume; sampling interval (between images) was 2.141 s for volumes 1-81, 30 s for volumes 82-98, and 60 s for volumes 99-108. The total imaging time was approximately 20 minutes. Subjects held their breath during the acquisition of volumes 13-22, 33-42, 61-70 and 79-108. Upon acquisition of dynamic 11 (i.e. 21 seconds after the start of the DCE acquisition), a bolus of Gd-EOB-DTPA (Primovist®, Bayer B.V., Mijdrecht, The Netherlands) at a standard dose of 0.025 mmol/kg (i.e, 0.1 mL/kg) was administered at 2 mL/s and flushed with 20 mL of saline at the same rate through an antecubital intravenous cannula, see Fig. 1.6.

1.4. CHALLENGES

CANCER which has spread from other organs to the liver, the so-called liver metastasis, is more common than primary liver cancer [28]. Patients with liver metastases of a primary colorectal cancer are often treated with (partial) resection. However, the future

remnant liver, the remaining part of the liver after resection, should allow adequate liver function to avoid liver failure. Therefore, accurate estimation of the future remnant liver's function is a crucial step before liver surgery. This assessment now includes a volumetric characterization, which is relatively easy to perform but is less important than the functional status of the future remnant liver, i.e. hepatocyte extraction function. Although DCE-MRI is able to assess the hepatocyte extraction function in a voxel-wise manner, it still remains challenging in many cases.

1.4.1. REGISTRATION

Movement of the liver during the acquisition procedure (that lasts about 20 minutes) is one of the most important challenges.

Image registration is the process of achieving spatial correspondence of partially overlapping images acquired by one or more modalities at a single or multiple time points [29]. In DCE-MRI, image registration is important because misalignment of the dynamic images would severely affect the subsequent quantification of the vascular integrity based on pharmacokinetic models (PKMs). However, image registration in abdominal DCE-MRI is challenging because the liver always shows a mixed motion pattern, including translation and deformation due to respiration, cardiac contractions and bowel peristalsis. Registration algorithms tend to get trapped into local minima easily [30]. Moreover, since the signal intensity varies in different dynamic images due to the enhancement effect of contrast agents, finding correspondences between voxels is inherently complicated [31]. Therefore, image registration is a far from trivial preprocessing step in order to obtain reliable results.

1.4.2. SEGMENTATION

When analyzing the liver function, the future remnant liver has to be segmented from 3D abdominal MRI volumes. However, the liver is usually wedge-shaped and becomes even more irregularly-shaped when liver tumors are present. Furthermore, the liver's signal intensity is not very different from adjacent organs in T_1-weighted MR images. Especially, when the spatial resolution is low, the border of the liver might be blurry due to partial volume effects [32]. These two issues hinder segmentation algorithms such as active contours [33]. Therefore, liver segmentation is often a challenging task before estimating the liver function.

In fact, a refined segmentation of the liver is desired. During liver surgery, resection of lesions inevitably goes at the expense of healthy liver tissue. To reduce this loss as much as possible and to limit the mortality rates after surgery, the Couinaud classification of liver anatomy was introduced [34]. This classification system partitions the liver into eight segments, each with an independent circulatory system. The partitioning result guides the surgeon to resect only that segment in which the tumor is localized, without damaging the liver parenchyma of adjacent segments [35]. Accurately partitioning the liver according to Couinaud's classification of liver anatomy would contribute to make better surgery plans but remains challenging since the spatial resolution of DCE-MR images is low.

1.4.3. PHARMACOKINETIC MODELING

Accurate pharmacokinetic models applied to DCE-MRI data enable reliable quantification of the vascular integrity in tissues. Tofts' model [36] is one of the most popular PKMs used over the last decades. It assumes that a voxel of tissue is comprised of three compartments: cells, plasma and interstitial space. The contrast agent arrives through the blood plasma, and it will diffuse into the interstitial space through pores in the capillary walls, driven by the difference in contrast agent concentration. Eventually, the contrast agent will diffuse out of the tissues again, finally to be excreted by the kidneys. However, this model is no longer valid in the liver because of two issues. The first one is that the liver has two vascular inputs whereas the Tofts' model only considers a single input; The second one is that the intra-cellular contrast agent Gd-EOB-DTPA can enter into hepatocytes whereas the Tofts' model the cells do not interact with the contrast agent. Although Sourbron *et al.* [17] tried to solve the aforementioned two issues by modifying the Tofts' model, limitations still remain in his model.

The first limitation is that Sourbron's model lacks of modeling of the input functions from two blood supply. Simply adopting the raw discrete time series of the blood supply as the input functions would introduce unpredicted error when estimating the kinetic parameters. The second limitation comes from B_1-inhomogeneity. As a DCE-MRI scan of the liver with this contrast agent typically takes 20 minutes, during which the liver experiences large displacement due to breathing, the signal intensity of the liver can be affected by B_1-inhomogeneities. Park *et al.* [37] and Sengupta *et al.* [38] conducted a simulation and an experimental study respectively to show that a small degree of B_1-inhomogeneity can cause a significant error in estimating pharmacokinetic parameters in DCE-MRI. Therefore, accurate pharmacokinetic modeling on liver is very challenging.

In this thesis new MR image analysis methods are developed to predict the functional status of the future remnant liver based on DCE-MRI. This will be combined with quantitative, MRI-based methods that allow segmental assessment of liver function.

1.5. THESIS OUTLINE

In **chapter** 2, a registration method called autocorrelation of local image structure (ALOST) [31] is extended. Particularly, an explicit segmentation of liver is introduced into the ALOST technique, in order to emphasize our region of interest during registration. We verify the liver mask extraction method and evaluate the registration performance of the proposed framework compared to the original ALOST approach.

In **chapter** 3, we present two novel frameworks for registration of DCE-MRI series of the liver. Both frameworks rely on an initial segmentation of the liver. Essentially, these two frameworks target to bring the registration close to the global optimum. The proposed methods were verified by using the root mean square error (RMSE) of fitting Sourbron's pharmacokinetic model to the signal in the liver, the mean target registration error (MTRE) of synthetically induced deformations, as well as the dice coefficient (DC) and mean surface distance (MSD) of the liver segmentation.

In **chapter** 4, we present an improved pharmacokinetic model for the liver. This model integrates vascular input functions and liver displacement to accelerate the fitting procedure and correct for B_1-inhomogeneity, respectively. We evaluate the model by using the root mean square error (RMSE) of fitting it to the signal in the liver and three model se-

lection techniques, namely, the Akaike Information Criterion (AIC), Bayesian Information Criterion (BIC) and Information Complexity (ICOMP).

In **chapter** 5, we present a segmentation framework for partitioning the liver according to Couinaud's classification of liver anatomy based on 4D dynamic contrast-enhanced magnetic resonance imaging (DCE-MRI) data. These data have high temporal resolution, but limited spatial resolution . We will show that our framework facilitates the segmentation of the liver vessels and in turn enables the segmentation of the eight liver segments. The Average Symmetric Surface Distance (ASSD), the Modified Hausdorff Distance (MHD) as well as the Dice Coefficient (DC) are adopted to evaluate the segmentation algorithm.

In **chapter** 6, a comparison study is conducted between DCE-MRI and Hepatobiliary Scintigraphy (HBS), which is the golden standard in a clinical setting for evaluating the liver function. The liver uptake rate is estimated from DCE-MRI using the pharmacokinetic model described in chapter 4. Meanwhile, the liver clearance rate is also extracted from HBS. We correlate the aforementioned two key indicators based on a dataset of 20 patients.

Finally, **chapter** 7 gives the summary and discussion of the presented work, and also proposes several future challenges.

REFERENCES

[1] W. Commons, *File:Anatomy Abdomen Tiesworks.jpg — Wikimedia Commons{,} the free media repository,* (2018).

[2] D. G. H. of Athens, *Laparoscopic Hepatectomies,* (2018).

[3] V. Kumar, A. K. Abbas, N. Fausto, and J. C. Aster, *Robbins and Cotran pathologic basis of disease, professional edition* (Elsevier Health Sciences, 2014).

[4] V. S. A. V. S. Associates, *Liver Ablation,* (2017).

[5] N. B. Ackerman, *The blood supply of experimental liver metastases. 1. The distribution of hepatic artery and portal vein blood to small and large tumors,* Surgery **66**, 1067 (1967).

[6] J. Hsieh, *Computed tomography: principles, design, artifacts, and recent advances* (SPIE Bellingham, WA, 2009).

[7] M. R. Oliva and S. Saini, *Liver cancer imaging: Role of CT, MRI, US and PET,* Cancer Imaging **4**, S42 (2004).

[8] E. Van Cutsem, H. M. W. Verheul, P. Flamen, P. Rougier, R. Beets-Tan, R. Glynne-Jones, and T. Seufferlein, *Imaging in colorectal cancer: progress and challenges for the clinicians,* Cancers **8**, 81 (2016).

[9] C. G. Child, *Surgery and portal hypertension,* The liver and portal hypertension (1964).

[10] R. Pugh, I. M. Murray-Lyon, J. L. Dawson, M. C. Pietroni, and R. Williams, *Transection of the oesophagus for bleeding oesophageal varices,* British Journal of Surgery **60**, 646 (1973).

[11] G. R. Cherrick, S. W. Stein, C. M. Leevy, and C. S. Davidson, *Indocyanine green: observations on its physical properties, plasma decay, and hepatic extraction,* The Journal of clinical investigation **39**, 592 (1960).

[12] A. Kwon, S. K. Ha-Kawa, S. Uetsuji, T. Inoue, Y. Matsui, and Y. Kamiyama, *Preoperative determination of the surgical procedure for hepatectomy using technetium-99m-galactosyl human serum albumin (99mTc-GSA) liver scintigraphy,* Hepatology **25**, 426 (1997).

[13] W. de Graaf, K. P. van Lienden, T. M. van Gulik, and R. J. Bennink, *99mTc-mebrofenin hepatobiliary scintigraphy with SPECT for the assessment of hepatic function and liver functional volume before partial hepatectomy,* Journal of Nuclear Medicine **51**, 229 (2010).

[14] B. E. Van Beers, C. M. Pastor, and H. K. Hussain, *Primovist, eovist: What to expect?* Journal of Hepatology **57**, 421 (2012).

[15] A. Frydrychowicz, M. G. Lubner, J. J. Brown, E. M. Merkle, S. K. Nagle, N. M. Rofsky, and S. B. Reeder, *Hepatobiliary MR imaging with gadolinium-based contrast agents,* (2012), arXiv:NIHMS150003 .

[16] H. Nilsson, A. Nordell, R. Vargas, L. Douglas, E. Jonas, and L. Blomqvist, *Assessment of hepatic extraction fraction and input relative blood flow using dynamic hepatocyte-specific contrast-enhanced MRI,* Journal of Magnetic Resonance Imaging **29**, 1323 (2009).

[17] S. Sourbron, W. H. Sommer, M. F. Reiser, and C. J. Zech, *Combined Quantification of Liver Perfusion and Function with Dynamic Gadoxetic Acid-enhanced MR Imaging,* Radiology **263**, 874 (2012).

[18] W. Contributors, *Magnetic resonance imaging — Wikipedia{,} The Free Encyclopedia,* (2018).

[19] M. H. Levitt, *Spin dynamics: basics of nuclear magnetic resonance* (John Wiley & Sons, 2001).

[20] L. N. Hand and J. D. Finch, *Analytical mechanics* (Cambridge University Press, 1998).

[21] R. W. Brown, E. M. Haacke, Y.-C. N. Cheng, M. R. Thompson, and R. Venkatesan, *Magnetic resonance imaging: physical principles and sequence design* (John Wiley & Sons, 2014).

[22] W. Contributors, *The Nobel Prize in Physiology or Medicine for 2003 - Press Release,* (2003).

[23] Philips, *MRI system / for full-body tomography / high-field / wide-bore Ingenia 1.5T,* .

[24] *Data Sheet PRIMOVIST - Medsafe,* (2018).

[25] M. Rohrer, H. Bauer, J. Mintorovitch, M. Requardt, and H. J. Weinmann, *Comparison of magnetic properties of MRI contrast media solutions at different magnetic field strengths,* Investigative Radiology **40**, 715 (2005), arXiv:arXiv:1011.1669v3 .

[26] C. S. P. van Rijswijk, M. J. A. Geirnaerdt, P. C. W. Hogendoorn, A. H. M. Taminiau, F. van Coevorden, A. H. Zwinderman, T. L. Pope, and J. L. Bloem, *Soft-tissue tumors: value of static and dynamic gadopentetate dimeglumine–enhanced MR imaging in prediction of malignancy,* Radiology **233**, 493 (2004).

[27] S. P. Sourbron and D. L. Buckley, *Classic models for dynamic contrast-enhanced MRI.* NMR in biomedicine **26**, 1004 (2013).

[28] B. Stewart, C. P. Wild, and Others, *World cancer report 2014,* Health (2017).

[29] Zhang Li, *Image registration for assessment of Crohn's disease severity,* Ph.D. thesis, Delft University of Technology (2015).

[30] M. P. Heinrich, M. Jenkinson, M. Brady, and J. A. Schnabel, *MRF-Based deformable registration and ventilation estimation of lung CT,* IEEE Transactions on Medical Imaging **32**, 1239 (2013).

[31] Z. Li, D. Mahapatra, J. A. W. Tielbeek, J. Stoker, L. J. Van Vliet, and F. M. Vos, *Image Registration Based on Autocorrelation of Local Structure,* IEEE Transactions on Medical Imaging **35**, 63 (2016).

[32] M. Á. González Ballester, A. P. Zisserman, and M. Brady, *Estimation of the partial volume effect in MRI,* Medical Image Analysis **6**, 389 (2002).

[33] T. F. Chan and L. a. Vese, *Active contours without edges.* IEEE transactions on image processing : a publication of the IEEE Signal Processing Society **10**, 266 (2001).

[34] C. Couinaud, *Le foie: {é}tudes anatomiques et chirurgicales* (Masson & Cie, 1957).

[35] E. M. Pauli, K. F. Staveley-O'Carroll, M. V. Brock, D. T. Efron, and G. Efron, *A handy tool to teach segmental liver anatomy to surgical trainees,* Archives of Surgery **147**, 692 (2012).

[36] P. S. Tofts, G. Brix, D. L. Buckley, J. L. Evelhoch, E. Henderson, M. V. Knopp, H. B. W. Larsson, T.-Y. Lee, N. A. Mayr, G. J. M. Parker, and Others, *Estimating kinetic parameters from dynamic contrast-enhanced T 1-weighted MRI of a diffusable tracer: standardized quantities and symbols,* Journal of magnetic resonance imaging **10**, 223 (1999).

[37] B. Park, B. S. Choi, Y. S. Sung, D.-C. Woo, W. H. Shim, K. W. Kim, Y. S. Choi, S. J. Pae, J.-Y. Suh, H. Cho, and Others, *Influence of B1-Inhomogeneity on Pharmacokinetic Modeling of Dynamic Contrast-Enhanced MRI: A Simulation Study,* Korean Journal of Radiology **18**, 585 (2017).

[38] A. Sengupta, R. K. Gupta, and A. Singh, *Evaluation of B1 inhomogeneity effect on DCE-MRI data analysis of brain tumor patients at 3T,* Journal of translational medicine **15**, 242 (2017).

2

Improved Registration of DCE-MR Images of the Liver Using a Prior Segmentation of the Region of Interest

In Dynamic Contrast-Enhanced MRI (DCE-MRI) of the liver, a series of images is acquired over a period of 20 minutes. Due to the patient's breathing, the liver is subject to a substantial displacement between acquisitions. Furthermore, due to its location in the abdomen, the liver also undergoes marked deformation. The large deformations combined with variation in image contrast make accurate liver registration challenging.

We present a registration framework that incorporates a liver segmentation to improve the registration accuracy. The segmented liver serves as region-of-interest to our in-house developed registration method called ALOST (autocorrelation of local image structure). ALOST is a continuous optimization method that uses local phase features to overcome space-variant intensity distortions. The proposed framework can confine the solution field to the liver and allow for ALOST to obtain a more accurate solution. For the segmentation part, we use a level-set method to delineate the liver in a so-called contrast enhancement map. This map is obtained by computing the difference between the last and registered first volume from the DCE series. Subsequently, we slightly dilate the segmentation, and apply it as the mask to the other DCE-MRI volumes during registration. It is shown that the registration result becomes more accurate compared with the original ALOST approach.

Published in Proc. SPIE, **9784**, 978443 (2016) [1].

2.1. INTRODUCTION

DYNAMIC Contrast-Enhanced MRI (DCE-MRI) is widely used to investigate the functioning of many organs. Important parameters quantifying the capillary permeability can be extracted from the time intensity data using pharmacokinetic models. However, DCE-MRI of the abdomen is hindered by motion due to breathing, and the resulting dynamic images are not aligned to each other. Many algorithms have been proposed to solve similar registration problems, e.g. based on normalized mutual information (NMI) [2] and the modality independent neighborhood descriptor (MIND) [3]. However, the outcome of these general approaches on DCE images can be inaccurate due to large spatial deformations and variations in the image contrast due to the inflow of contrast agent. A registration method called autocorrelation of local image structure metric (ALOST) [4] has been shown to efficiently deal with contrast variations. Still, the problem remains challenging due to the large magnitude of prevalent deformations.

In this paper, the focus is on liver imaging. We introduce an explicit segmentation of the organ into the ALOST technique, in order to emphasize our region of interest during registration. The segmentation is obtained by applying a level-set method to a so-called contrast enhancement map. We will show that the initial segmentation improves the registration precision by restricting the search space.

In this paper we first briefly introduce the registration method ALOST, the liver segmentation method and a model for determining the intracellular uptake rate of the contrast agent. Subsequently, we evaluate the liver mask extraction method and evaluate the registration performance of the proposed framework compared to the original ALOST approach.

2.2. METHODOLOGY

2.2.1. REGISTRATION BY AUTOCORRELATION OF LOCAL IMAGE STRUCTURE (ALOST)

THE modality independent neighborhood descriptor (MIND) method [3] is a state-of-the-art registration technique for multi-modal image registration. Essentially, it relies on a patch-based descriptor of the structure in a local neighborhood:

$$MIND(I,\mathbf{x},\mathbf{r}) = \frac{1}{n}\exp\left(-\frac{D_p(I,\mathbf{x},\mathbf{x}+\mathbf{r})}{V(I,\mathbf{x})}\right) \tag{2.1}$$

in which I is an image, $\mathbf{r}$ is an offset in neighborhood R of size $R{\times}R$ around position $\mathbf{x}$ and n a normalization constant; D_p is the distance between two image patches $(2p+1)^d$ (with image dimension d), measured by the sum of squared differences (SSD):

$$D_p(I,\mathbf{x_1},\mathbf{x_2}) = \sum_{\mathbf{p}\in P}\left(I(\mathbf{x}_1+\mathbf{p}) - I(\mathbf{x}_2+\mathbf{p})\right)^2 \tag{2.2}$$

and $V(I,\mathbf{x})$ is the mean of the patch distances in a small neighborhood N:

$$V(I,\mathbf{x}) = \frac{1}{num(N)}\sum_{\mathbf{n}\in N} D_p(I,\mathbf{x},\mathbf{x}+\mathbf{n}) \tag{2.3}$$

Recently, we have introduced a novel registration metric that relies on the monogenic signal [5]. The monogenic signal is a generalization of the so-called analytic signal from one to higher dimensions based on the Riesz transform. The analytic representation of a signal applies the concept that negative frequency components of a 1-D, real-valued signal are essentially superfluous due to the Hermitian symmetry of the Fourier Spectrum.

The monogenic signal is an efficient tool to describe the local image structure by means of local phase. Particularly, the mean phase (MP), i.e. the average phase calculated over several scales, serves as an identifier for the type of image feature. For example, a step corresponds to $\phi = 0$ and a peak to $\phi = \pi$. Furthermore, it has been recognized that salient features are perceived at points in an image where the Fourier components are in phase. Several measures for phase congruency (PC) [6] have been developed expressing that if all scale components are in phase, PC = 1; alternatively, if there is no coherence of phase, then PC = 0.

The mean phase and phase congruency extracted from the monogenic signal share the same advantage that they are insensitive to space-variant intensity distortions, e.g. the intensity difference due to contrast enhancement and the MRI bias field. This ability is what the MIND approach lacks [4]. Therefore, we have integrated MP and PC into MIND to extract local image information into a descriptor called ALOST [4]:

$$ALOST(I,\mathbf{x},\mathbf{r}) = [MIND(MP(I),\mathbf{x},\mathbf{r}), MIND(PC(I),\mathbf{x},\mathbf{r})] \tag{2.4}$$

Essentially, the registration is performed by minimizing the next energy function

$$E(\mathbf{w}) = E_{ALOST}(\mathbf{w}) + \alpha E_R(\mathbf{w}) \tag{2.5}$$

where α is a weighting coefficient that balances the two terms of our energy function:
1. Data term

$$E_{ALOST}(\mathbf{w}) = \int_{\Omega} \left[ALOST_m(\mathbf{x}+\mathbf{w}(\mathbf{x})) - ALOST_f(\mathbf{x})\right]^2 d\mathbf{x} \tag{2.6}$$

2. Regularization term

$$E_R(\mathbf{w}) = \int_{\Omega} [\nabla u(\mathbf{x})]^2 + [\nabla v(\mathbf{x})]^2 + [\nabla w(\mathbf{x})]^2 d\mathbf{x} \tag{2.7}$$

where $\mathbf{w} = [u,v,w]$ is the 3D deformation field. The subscript m and f represent moving and fixed images, respectively. Ω is the entire image for integration. More details on the ALOST approach can be found in [4]. In this paper, the last volume in DCE-MRI was regarded as the fixed image. As such, the other volumes were registered to the fixed image pair-wisely.

In our DCE-MRI scan, the total imaging time was approximately 20 minutes (more details are given below). During imaging, we let the patient hold his/her breath, especially around the time when the contrast agent arrived in the liver. We did this to limit images distortion by intra-scan motion, as these images are crucial for accurate pharmacokinetic imaging. However, we have observed that these images show large distortions compared to images acquired during regular breathing, i.e. acquired at the beginning and the end of the DCE series.

As ALOST could not cope with such distortion, we restrict the search space of the registration by using a prior segmentation of the liver as a region of interest.

2.2.2. SEGMENTATION

The liver shows the strongest contrast enhancement at the end of the DCE series (considering a DCE-MRI sequences of 20 minutes). This is generally termed the hepatic phase, as the uptake rate of the contrast agent into the liver cells reaches its maximum at that time. Accordingly, subtraction of the registered first volume from the last volume yields an image in which the liver is maximally "enhanced", whereas other organs are suppressed:

$$CE_{liver} = I_{post} - I_{pre} \tag{2.8}$$

Notice that the shape and location of the liver are more or less the same in the two images since the patient is breathing rather shallowly at the very beginning and at the end of the DCE series. Therefore, good registration accuracy can be achieved by applying ALOST even without a mask.

In the CE_{liver} map, the liver is very clearly visible (e.g. Fig. 2.2(d))). We use a level-set method to segment the liver in order to obtain the mask. Among several level-set methods, the geodesic [7] and the Chan-Vese [8] models are the benchmarks with respect to boundary- and region-based methods. The hybrid method proposed by Y. Zhang *et al.* [9] takes boundary as well as region information into consideration while minimizing the next data term:

$$E(\phi) = -\int_{\Omega} (I-\mu)\, H(\phi)\, d\Omega + \beta \int_{\Omega} g \left|\nabla H(\phi)\right| d\Omega \tag{2.9}$$

where I is the image, g represents the gradient of the image, β is a weighting coefficient, Ω is the entire image for integration, $H(\phi)$ is the Heaviside function, and μ is a parameter that represents the lower bound of the gray-level in the segmented object. In this model, an active contour is embedded implicitly as a constant set in a function defined in a higher dimensional space. The function is called embedding function and denoted as ϕ. Essentially, the first term integrates the (negated) intensity inside the segmented region and the second term integrates the derivative along the boundary of the segmented region.

When the liver mask M_{liver} has been extracted, we dilate it somewhat ($M_{liver}^{dilated}$) to make sure that the liver boundary is included in the mask in most images.

In summary, our approach reduces to the following steps: (1) we register the first volume to the last one, and calculate the contrast enhancement via Eq. 2.8; (2) we segment the liver in the CE_{liver} map and obtain the mask; (3) we dilate the mask somewhat, so that the boundary of the liver is included in the mask (i.e. the most salient information); (4) we apply the dilated mask to the entire image series, while optimizing Eq. 2.5. As such, Eq. 2.5 is only evaluated over the a priori segmented region. We do so while registering the entire DCE series to the last image since that image shows the largest contrast and has been acquired during shallow breathing.

2.2.3. MODELED SIGNAL IN THE LIVER

In order to evaluate the benefit of our approach we will fit a model to the time-intensity signal in the segmented region. The residual of the fit will be considered a measure of the registration accuracy. Therefore, we adopt the liver model proposed by S. Sourbron *et al.* [10], henceforth referred to as "the Sourbron model". This dual-inlets two-compartment uptake model was especially designed for the intracellular hepatobiliary contrast agent Gadoxetate disodium (Primovist^{TM}, Bayer pharmaceutical). The diagram in Fig. 2.1 sketches

the model. The arterial input function (AIF) and venous input function (VIF) are the dual inlets since blood is supplied to the liver by the hepatic artery as well as the portal vein. The AIF and VIF represent the contrast agent concentration in the blood plasma of the hepatic artery and portal vein respectively. These were obtained by averaging the top three time intensity curves having the highest contrast enhancement measured voxel-wise in regions manually delineated in the aorta (cranially from the hepatic artery) and the portal vein. T_A and T_V represent time delays and F_A and F_V are arterial and venous plasma flows, respectively. Furthermore, in the gray rectangle denoting liver tissue, the left circle represents the extracellular compartment and the right circle stands for the intracellular compartment, i.e. corresponding to the hepatocytes. As such, V_E is the extracellular volume and K_I represents the uptake rate of the hepatocytes represented by a volume V_I.

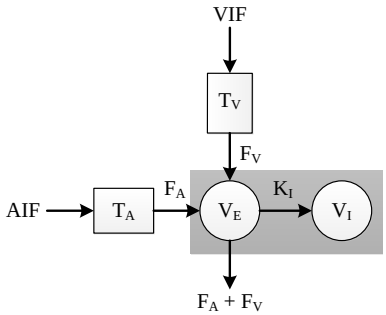

Figure 2.1: The Sourbron model: a dual-inlets two-compartment uptake model for Primovist in the liver. The AIF and VIF are dual inlets into the liver, representing the concentration of the contrast agent over time entering from the hepatic artery and the portal vein. T_A and T_V are time delays. F_A and F_V are the arterial and venous plasma flows, respectively (in mL per minute per 100 mL). In the gray rectangle representing the liver, the left circle represents the extravascular extracellular compartment V_E (in mL per 100 mL) and the right circle stands for the hepatocyte compartment. K_I (per minute) is the liver uptake rate.

Let C_E and C_I be the contrast agent concentrations in the extravascular, extracellular compartment and hepatocytes, respectively. Defining C_A and C_V as the concentrations of the AIF and VIF, the mass transport between the two compartments can be expressed as

$$\begin{cases} V_E \dfrac{dC_E}{dt}(t) = F_A C_A(t - T_A) + F_V C_V(t - T_V) - (F_A + F_V + K_I) C_E(t) \\ V_I \dfrac{dC_I}{dt}(t) = K_I C_E(t) \end{cases} \tag{2.10}$$

and the solution for the total liver tissue concentration ($C_T = V_E C_E + V_I C_I$) is

$$C_T(t) = \left[T_E \delta(t) + \frac{K_I}{F_A + F_V + K_I} \right] * \frac{e^{-\frac{t}{T_E}}}{T_E} * [F_A C_A(t - T_A) + F_V C_V(t - T_V)] \tag{2.11}$$

where * is the convolution operator and $T_E\,(V_E / [F_A + F_V + K_I])$ represents the extracellular mean transit time.

2.3. RESULTS

THIS study included 8 patients diagnosed with colorectal liver metastasis (2), hepatocellular carcinoma (2) and benign (4). All scans were operated between December 2014 and May 2015. The final cohort (age range, 43 - 70 years; mean age, 59.8 years) included 6 men (age range, 50–70 years; mean age, 61.2 years) and 2 women (age range, 43 - 48 years; mean age, 55.5 years). The study was approved by the ethical review board of the Amsterdam University Medical Centers and registered under ID NL45755.018.13. Informed consent was obtained from all individual participants included in the study.

DCE-MRI data were acquired on a 3T Philips Ingenia whole-body scanner via a 3D SPGR sequence. The acquisition parameter settings were T_E/T_R = 2.3/3.75 ms, FA = 15°, matrix size = 128×128×44, voxel size = 3×3×5 mm^3, acquisition time = 2.141 s for each volume; the sampling interval (between images) was 2.141 s for volumes 1-81, 30 s for volumes 82-98 and 60 s for volumes 99-108. The total imaging time was approximately 20 minutes. Patients held their breath during the acquisition (about 3 s) of volumes 13-22, 33-42, 61-70 and 79-108. Upon acquisition of dynamic 11 (i.e. 21 seconds after the start of the DHCE acquisition), a bolus of Gd-EOB-DTPA (Primovist®, Bayer B.V., Mijdrecht, The Netherlands) at a standard dose of 0.025 mmol/kg (i.e, 0.1 mL/kg) was administered at 2 mL/s and flushed with 20 mL of saline at the same rate through an antecubital intravenous cannula. In chapter 4, appendix 3 of section 4.5 shows how to convert DCE-MR signal to tissue concentration.

All algorithms were implemented in MATLAB (version R2015b; Mathworks, Natick, USA). The nonlinear least-squares fitting routine *lsqcurvefit* was used to perform the model fits; 19 cores were adopted for parallel computing on a HPC equipped with two Intel(R) Xeon(R) CPU E5-2698 v4 clocked at 2.20GHz and 256GB RAM memory.

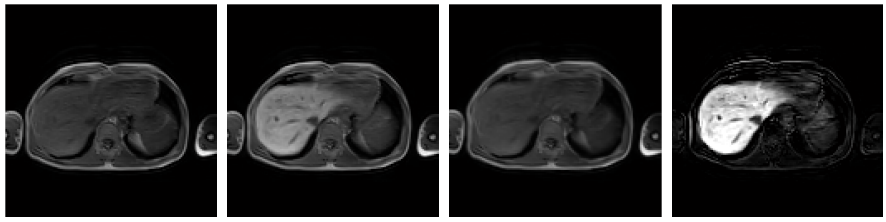

(a) (b) (c) (d)

Figure 2.2: (a) Pre-contrast image (the first volume); (b) Post-contrast image (the last volume); (c) the registered image of (a) by ALOST without liver mask; (d) The CE_{liver} map.

Exemplary pre-contrast and post-contrast images are shown in Fig. 2.2(a) and Fig. 2.2(b), respectively. Obviously, the liver is highly enhanced in the post-contrast image. Fig. 2.2(c) is the outcome of registering Fig. 2.2(a) to 2.2(b) by ALOST without applying a mask. Actually, in Fig. 2.2(a) and 2.2(d) the location and shape of the liver are almost the same since the patients breathed quietly at the very beginning and at the end of the acquisition series. Fig. 2.2(d) is the CE_{liver} map, which is calculated by Eq. 2.8. In this image, the liver is highlighted while the other organs in the abdomen display a very low intensity.

Fig 2.3 and 2.4 show the 3D liver mask (i.e. the segmentation) and 2D cross-sections of the mask boundary overlaid on the CE_{liver} map. Clearly, the mask matches the liver very well.

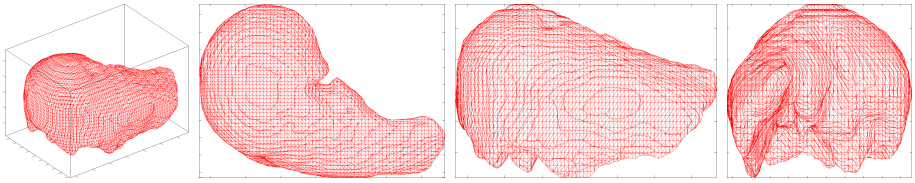

(a) (b) (c) (d)

Figure 2.3: 3D mask (segmentation) of the liver. (a) 3D view; (b) The front view; (c)Tthe top view; (d) The right side view.

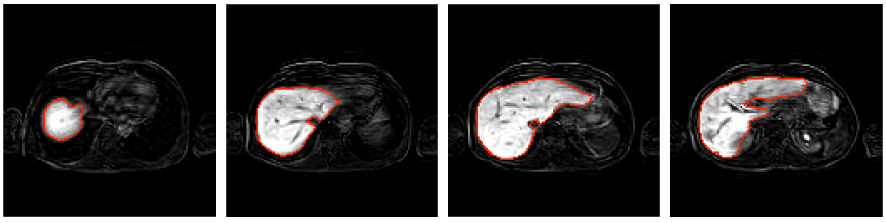

(a) (b) (c) (d)

Figure 2.4: Overlay of CE_{liver} map and the liver mask's boundary. (a) Slice 36; (b) Slice 31; (c) Slice 27; (d) Slice 21.

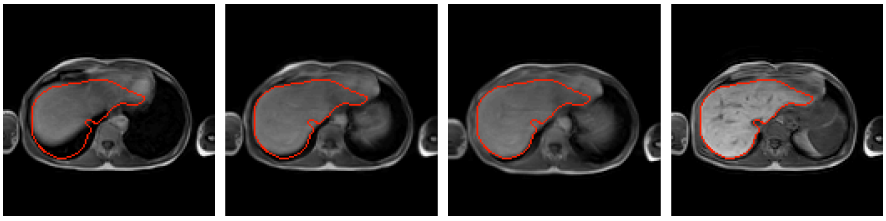

(a) (b) (c) (d)

Figure 2.5: (a) Moving image; (b) Registered image by ALOST alone; (c) Registered image by ALOST supported by the dilated liver mask; (d) Fixed image

The registration improvement by application of a mask is illustrated in Fig. 2.5. The moving image and the fixed image are shown in Fig. 2.5(a) and 2.5(d), respectively. We also drew the outline of the liver mask in 2.5(d) and copied it to the other sub figures to facilitate the comparison. The registration result obtained by ALOST alone can be seen in Fig. 2.5(b). Compared with the moving image, the liver in 2.5(b) is more similar to

Fig. 2.5(d), but near the bottom of the liver mask, the mismatch, indicated by the red arrow, shows that the registration is still off. Fig. 2.5(c) shows that ALOST supported by the dilated liver mask produces a more accurate registration outcome.

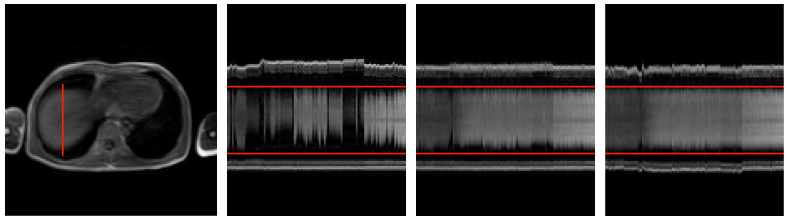

(a) (b) (c) (d)

Figure 2.6: (a) Transverse plane of slice 34. (b)-(d) Intensity as a function of time along the red line: (b) Raw DCE data (prior to registration); (c) ALOST registration without the dilated liver mask; (d) ALOST registration with the dilated liver mask.

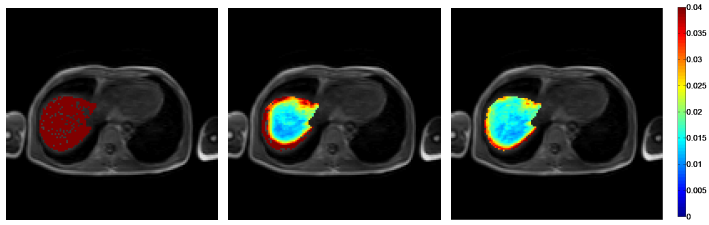

(a) (b) (c)

Figure 2.7: RMSE of fitting the liver model function to the intensity data from each pixel: (a) Raw DCE data; (b) ALOST data without the dilated liver mask; (c) ALOST data with the dilated liver mask.

Furthermore, we chose another slice and selected a line segment through the liver to investigate the intensity as a function of time, see Fig. 2.6(a). In Fig. 2.6(a)-2.6(d) the edge of the dilated liver mask is also drawn for reference. Large fluctuations can be observed over time along this line prior to registration, see Fig. 2.6(b). Most of the fluctuations are compensated by ALOST, see Fig. 2.6(c), but some mismatches are still visible. The most accurate outcome is generated by ALOST supported by the dilated liver mask, as demonstrated in Fig. 2.6(d).

Fig. 2.7 shows the distribution of the root mean square error (RMSE) that remains after fitting the Sourbron model to the time intensity curves (TICs). One can see that the RMSE is huge when no registration is performed, see Fig. 2.7(a). In Fig. 2.7(b), produced by ALOST registration without the liver mask, the RMSE is only large near the boundary of the liver, where there is large fluctuation in signal intensity due to mis-registration. The smallest RMSE is provided by ALOST registration supported by the dilated liver mask, see Fig. 2.7(c). Notice that the RMSE is especially reduced near the edge of the liver.

Henceforth, we focus on investigating the registration performance near the liver boundary. Therefore, the liver mask was eroded by a 26-connected 3×3×3 kernel and then sub-

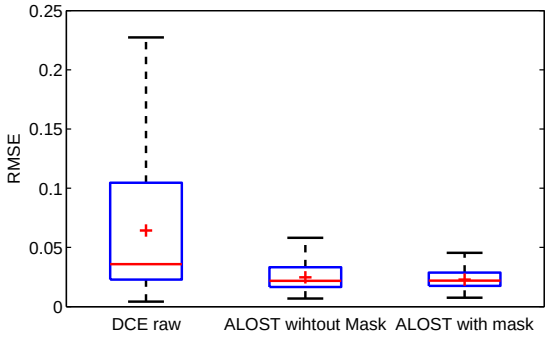

Figure 2.8: Box-and-whisker plots of the root mean squared error (RMSE) of the model fits at the liver boundary prior to registration (DCE raw) and after registration without and with support of the dilated liver mask.

tracted from the original liver mask. As a result, a mask is obtained of the liver boundary. Fig. 2.8 shows how the RMSE measure varies at the boundary of liver in the first patient prior to registration and after registration without and with support of the dilated liver mask.

Table 2.1: Evaluation of the registration performance on 8 abdominal DCE-MRI datasets by ALOST without and with the support of the dilated liver mask. The performance was measured by the RMSE that remains after fitting the Sourbron model to TICs near the liver boundary. The numbers report the mean value and the standard deviation (std) between brackets. The numbers printed in boldface are the best result per row.

Case	Raw DCE	ALOST without Mask	ALOST with Mask
1	0.0643 (0.0607)	0.0248 (0.0116)	**0.0228 (0.0075)**
2	0.0361 (0.0254)	0.0230 (0.0114)	**0.0215 (0.0083)**
3	0.0326 (0.0191)	0.0289 (0.0163)	**0.0282 (0.0141)**
4	0.0570 (0.0352)	0.0518 (0.0263)	**0.0484 (0.0214)**
5	0.0366 (0.0171)	0.0289 (0.0139)	**0.0276 (0.0116)**
6	0.0676 (0.0557)	0.0367 (0.0191)	**0.0313 (0.0132)**
7	0.0445 (0.0317)	0.0299 (0.0178)	**0.0272 (0.0129)**
8	0.0573 (0.0444)	0.0324 (0.0186)	**0.0302 (0.0141)**

Apparently, ALOST with support of the dilated liver mask achieves the smallest RMSE value and standard deviation. The same approach applied to all 8 patients yields the outcomes shown in Table 2.1. It demonstrates that ALOST with support of the dilated liver mask achieves the best registration accuracy.

2.4. CONCLUSION

THE framework proposed by us integrates a liver segmentation into the ALOST registration framework. This segmentation method was based on the so-called contrast enhancement map. The prior segmentation supports ALOST by restricting the search space. The improved registration was demonstrated by better fits of the Sourbron model to the

time intensity data after registration. The proposed framework can be easily adapted to other DCE-MRI applications with different contrast agents provided that a segmentation of the organ of interest is available.

REFERENCES

[1] T. Zhang, Z. Li, J. H. Runge, C. Lavini, J. Stoker, T. van Gulik, L. J. van Vliet, and F. M. Vos, *Improved registration of DCE-MR images of the liver using a prior segmentation of the region of interest,* (2016).

[2] C. Studholme, D. Hill, and D. Hawkes, *An overlap invariant entropy measure of 3D medical image alignment,* Pattern Recognition **32**, 71 (1999).

[3] M. P. Heinrich, M. Jenkinson, M. Bhushan, T. Matin, F. V. Gleeson, S. M. Brady, and J. A. Schnabel, *MIND: Modality independent neighbourhood descriptor for multi-modal deformable registration,* Medical Image Analysis **16**, 1423 (2012).

[4] Z. Li, D. Mahapatra, J. A. W. Tielbeek, J. Stoker, L. J. Van Vliet, and F. M. Vos, *Image Registration Based on Autocorrelation of Local Structure,* IEEE Transactions on Medical Imaging **35**, 63 (2016).

[5] M. Felsberg and G. Sommer, *The monogenic signal,* IEEE Transactions on Signal Processing **49**, 3136 (2001).

[6] P. Kovesi, *Edges Are Not Just Steps,* ACCV202: The 5th Asian Conference on Computer VIsion , 23 (2002).

[7] V. Caselles, R. Kimmel, and G. Sapiro, *Geodesic Active Contours,* International Journal of Computer Vision **22**, 61 (1997).

[8] T. F. Chan and L. a. Vese, *Active contours without edges.* IEEE transactions on image processing : a publication of the IEEE Signal Processing Society **10**, 266 (2001).

[9] Y. Zhang, B. J. Matuszewski, L.-K. Shark, and C. J. Moore, *Medical Image Segmentation Using New Hybrid Level-Set Method,* in *2008 Fifth International Conference BioMedical Visualization: Information Visualization in Medical and Biomedical Informatics* (2008) pp. 71–76.

[10] S. Sourbron, W. H. Sommer, M. F. Reiser, and C. J. Zech, *Combined Quantification of Liver Perfusion and Function with Dynamic Gadoxetic Acid-enhanced MR Imaging,* Radiology **263**, 874 (2012).

3

Improved Initialization Frameworks for 4D Registration of DCE-MR Images of the Liver based on a Prior Segmentation

Dynamic contrast-enhanced MRI (DCE-MRI) enables quantification of vascular integrity based on pharmacokinetic modeling. Accurate alignment of the anatomical structures of interest is a prerequisite, which is especially challenging in abdominal DCE-MRI. The registration of these images is problematic as the optimization can easily get trapped in a local minimum.

In this paper, we propose a local and a global 4D registration frameworks aiming at reducing the sensitivity to local minima in the registration of the liver. Liver segmentation is incorporated into these frameworks to obtain the mean relative liver displacement. In the local framework, we impose an ordering to the registration of dynamics by the distance in the superior-inferior direction from a reference image. The images are sequentially registered to the reference image starting with the images with the shortest distance. Essentially, the registration of one image is brought close to the solution by means of its registration to the preceding image combined with the registration of the latter to the reference. In the global framework, a linear relation between the mean relative liver displacement and the displacement of individual points in the liver is initially asserted. It also targets to bring the registration close to the global optimum by iteratively adjusting an initial registration based on this assumed relation.

Submitted to IEEE Transactions on Biomedical Engineering.

The proposed methods were compared to two state-of-the-art methods that also aim to avoid local minima. The performance of the registration methods was quantitatively assessed using the root mean square error (RMSE) of fitting Sourbron's pharmacokinetic model to the signal in the liver as well as the mean target registration error (MTRE) of synthetically induced deformations. We found that the proposed frameworks outperformed the existing methods in all but a minority of the cases.

3.1. INTRODUCTION

DYNAMIC contrast-enhanced MRI (DCE-MRI) is a technique that can be used to assess properties of the perfusion in organs such as the liver and kidneys [1]. Particularly, pharmacokinetic models (PKM's) enable quantification of the vascular integrity [2]. However, abdominal DCE-MRI is hindered by motion due to respiration, heart beating and bowel peristalsis. The PKM analysis can be severely affected by misalignment of the dynamic images. Therefore, image registration is often a crucial preprocessing step in order to obtain reliable results.

Typically, a registration method consists of three key parts: a deformation model, an objective function and an optimization strategy [3]. An efficient optimization strategy is pivotal since it helps the registration to converge to a global optimum instead of getting trapped into one of many local minima. In this paper, we focus on registering DCE-MRI data of the liver. This registration problem is challenging because the liver experiences large displacement due to respiration.

We will introduce two novel registration frameworks that target convergence in the global optimum. These frameworks integrate a state-of-the-art objective function with new initialization strategies: a sequential, local one and a global one.

3.1.1. RELATED WORK

Many objective functions were previously proposed to determine the similarity between two DCE-MRI images, e.g. mutual information (MI) [4], normalized gradient fields (NGF) [5] and the modality independent neighborhood descriptor (MIND) [6]. Among these methods, MIND is a state-of-the-art multi-modal registration technique that relies on the concept of image self-similarity. MIND was shown to be robust against global intensity variation between images, which makes it suitable to register DCE images. Particularly, MIND had better registration performance than other state-of-the-art techniques such as conditional mutual information (CMI) and normalized mutual information (NMI) [6]. More recently, an improved version of MIND was proposed called the self-similarity context (SSC), which reduces the strong dependency of the original descriptor on the central pixel of applied patches [7].

Optimization strategies can be divided into two categories: continuous and discrete [3]. Continuous optimization typically deals with real-valued variables. The most often used continuous methods are gradient descent based, such as steepest descent [8], conjugate gradient descent [9], Quasi-Newton [10] and Gauss-Newton [11]. Among those techniques, Gauss-Newton method is widely applied since it avoids calculating second derivatives and has good convergence speed [3]. However, all continuous methods are sensitive to the initial condition and can get stuck in a local minimum. In order to avoid this, discrete optimization methods adopt a global search. Many discrete optimization approaches have been proposed, such as graph cuts [12], belief propagation [13] and linear programing [14]. Essentially, discrete optimization involves a reduction of the search space to a limited, discrete number of potential solutions. The best solution of this discrete search space is expected to lie close to the global optimum. Therefore, the method is especially suitable to deal with large deformations. Recently a dense displacement sampling (DEEDS) in combination with a discrete optimization strategy based on belief propagation was proposed [15]. A dense stochastic displacement sampling was adopted on the

similarity term to avoid local minima. Moreover, a sophisticated message passing technique contributed to finding the global solution.

While much research has focused on developing new continuous and discrete methods that involve two images, there has been relatively little attention for the registration of 4D DCE series.

Previously, modeling the periodic motion over time was used to support the registration of dynamics. For instance, Metz *et al.* [16] took both spatial and temporal smoothness of the transformations into consideration using free-form B-spline deformation model. Furthermore, Xu *et al.* [17] proposed a symmetric 4D registration algorithm that involves forward and an inverse 4D B-spline functions to keep inverse consistency. Li *et al.* [18] employed template selection and retrospective gating to compensate for respiratory and peristaltic motions in abdominal DCE-MRI. A limitation of these methods is that the patients must be freely breathing while the images are acquired, which may lead to artifacts. Additionally, the time interval between adjacent images must be sufficiently small for an appropriate sampling during the breathing cycle to make sure that the B-spline fitting is reliable.

In our DCE-MRI scans of the liver, the time sampling is not constant. At the very beginning of the scan, the time interval is small, i.e. 2 s, in order to capture the rapid change in signal during the inflow of the contrast agent. Subsequently, the time interval increases to 60 s while the changes in signal intensity become smaller. Furthermore, the patients were instructed to hold their breath during various stages of the scanning process. For these reasons the aforementioned techniques are not applicable to our data.

Alternatively, some authors aimed to warp the registration problem into another domain or space to exploit the relation of images along the time axis. For instance, Hamm *et al.* [19] implemented a geodesic registration on anatomical manifolds. A kNN graph was constructed to find the shortest paths between all pairs of images. To do so, an initial pairwise registration step was taken to build the kNN graph. However, this is time-consuming, especially for series consisting of a large number of images. Furthermore, Feng *et al.* [20] relied on Robust Principal Component Analysis (RPCA) to register an image series residing on a low-dimensional manifold. Feng split the image series into low rank and sparse components similar to Robust Data Decomposition Registration (RDDR) [21]. A limitation of these methods is that they are purely 2D registration approaches. In order to register 3D images, the registration has to be performed in a slice-by-slice fashion. As such these method only hold as long as the scan slices are thick and/or the motion across the slices is relatively small. In order to overcome this problem, Huizinga *et al.* [22] proposed a PCA-based group-wise method to deal with 4D data. It is based on the assumption that a low-dimensional signal model can describe intensity changes in quantitative MRI. Furthermore, the group-wise formulation of this method avoids having to choose a reference image in the 4D series, which should reduce registration bias. However, a shortcoming of this method is its low time efficiency. As indicated by the author, by default 1000 iterations and 2048 random coordinate samples were required for each resolution. As a result, registering a 4D dataset took hours of computing time.

3.1.2. OBJECTIVE

In this paper we present two novel frameworks for registration of DCE-MRI series of the liver. Both frameworks rely on an initial segmentation of the liver. In the first we exploit the proximity of deformation fields to sequentially register images in an ordered fashion. In the second framework the global liver displacement helps in predicting the deformation 'tendency' along the time axis. The deformation tendency allows us to obtain a better starting point for the registration. As such both methods aim to start registration close to the optimum and avoid getting trapped in a local minimum. Both techniques rely on SSC as the registration engine.

3.2. METHOD

3.2.1. OBJECTIVE FUNCTION

THE self-similarity context (SSC) is a patch-based descriptor of the structure in a certain neighborhood layout N, defined as:

$$SSC\left(I,\mathbf{x},\mathbf{y}\right)=\exp\left[-\frac{D\left(I,\mathbf{x},\mathbf{y}\right)}{V\left(I,\mathbf{x}\right)}\right]\mathbf{x},\mathbf{y}\in N \tag{3.1}$$

in which I is an image, $\mathbf{x}$ and $\mathbf{y}$ are the center locations of two patches within N, and D is the distance between the two image patches measured by the sum of squared differences (SSD):

$$D\left(I,\mathbf{x_1},\mathbf{x_2}\right)=\sum_{\mathbf{y}\in N}\left[I\left(\mathbf{x}_1+\mathbf{y}\right)-I\left(\mathbf{x}_2+\mathbf{y}\right)\right]^2 \tag{3.2}$$

and $V(I,N)$ is the mean of the patch distances in neighborhood N:

$$V\left(I,N\right)=\frac{1}{num\left(N\right)}\sum_{\mathbf{x},\mathbf{y}\in N}D\left(I,\mathbf{x},\mathbf{y}\right) \tag{3.3}$$

The initial descriptor, MIND [6], included the distances of a center patch to its six connected neighbors. Instead, the SSC operator is based on all distances in a six neighborhood (with a Euclidean distance of $\sqrt{2}$ between them), while the central pixel is excluded from N.

SSC registration can be described as

$$\mathbf{u}^*=\arg\min_{\mathbf{u}}\left\{\sum_{\mathbf{x}}\left[\frac{1}{|R|}\sum_{\mathbf{r}\in R}|SSC\left(I,\mathbf{x},\mathbf{r}\right)-SSC\left(J,\mathbf{x},\mathbf{r}\right)|\right]+\alpha|\nabla\mathbf{u}\left(\mathbf{x}\right)|^2\right\} \tag{3.4}$$

where $\mathbf{u}=(u,\ v,\ w)$ is the deformation field and α the regularization parameter, i.e. a coefficient that weighs the regularization term.

In this paper we follow the default setup as introduced in [7]: $R=3$, $N=N_6$, i.e. a six-connected neighborhood, patch size $D=3$, and the regularization coefficient $\alpha=0.1$.

3.2.2. LIVER SEGMENTATION METHOD

We adopted the liver segmentation method that we proposed previously [23]. Essentially, after the contrast agent (Gadoxetate disodium, Primovist^{TM}, Bayer) is injected, the signal intensity in the liver will keep increasing due to accumulation of the contrast agent inside the hepatocytes, reaching a peak in the hepatobiliary phase (~20 min after the injection). However, it is still difficult to segment the liver in the hepatobiliary phase, as shown in Fig. 3.1(b), because the contrast with the surrounding organs is not very high. However, as we apply a liver-specific contrast agent, the surrounding organs do show smaller enhancement. Maximal contrast is therefore achieved by registering the pre-contrast image (the first image) to an image acquired in the hepatobiliary phase (post-contrast, the last image), and obtain a liver contrast enhancement (CE) map by

$$CE_{liver} = I_{hepatobiliary\ phase} - I_{pre\ contrast} \tag{3.5}$$

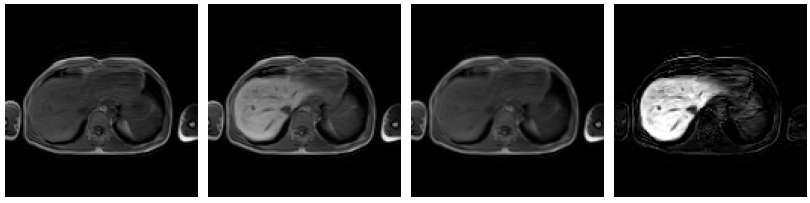

(a) (b) (c) (d)

Figure 3.1: (a) Pre-contrast image (the first volume); (b) Post-contrast image (the last volume); (c) The registered image of (a) by conventional registration; (d) The CE_{liver} map.

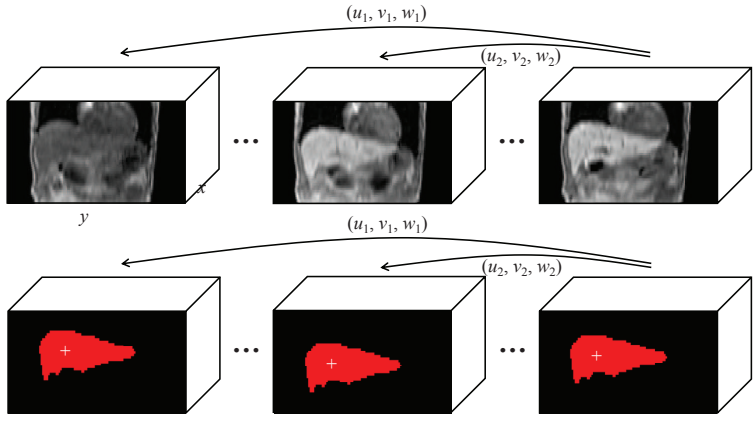

Figure 3.2: Schematic diagram illustrating how a coarse delineation of the liver is obtained: (1) The last volume is registered to each other dynamic volume of the DCE-MRI series; (2) The obtained deformation field is applied to warp the liver segmentation obtained from the contrast enhanced image to each time point.

Fig. 3.1(d) shows that the liver clearly stands out because surrounding structures are

suppressed by the subtraction. Then, we apply a level-set approach [24] to segment the liver resulting in a liver mask. Among several level-set methods, the geodesic [25] and the Chan-Vese [26] models are benchmarks with respect to boundary- and region-based methods. The hybrid method proposed by Y. Zhang *et al.* [24] takes boundary as well as region information into consideration while minimizing this data term:

$$E(\phi) = -\int_{\Omega} (I-\mu)\, H(\phi)\, d\Omega + \beta \int_{\Omega} g\, |\nabla H(\phi)|\, d\Omega \tag{3.6}$$

where I is the image, g represents the gradient of the image, β is a weighting coefficient, $H(\phi)$ is the Heaviside function, and μ is a parameter that represents the lower bound of the gray-level in the segmented object. Essentially, the first term integrates the (negated) intensity inside the segmented region and the second term integrates the derivative along the boundary of the segmented region.

The obtained mask accurately segments the liver in the two registered images. Simultaneously, it facilitates a coarse segmentation of the liver in the other volumes of the DCE-MRI series. To do so, the last image is registered to each dynamic volume individually. Subsequently, the obtained transformations are applied to the liver mask to yield a liver segmentation in each dynamic volume as shown in Fig. 3.2. Furthermore, the liver's mean relative displacement in a dynamic volume with respect to the last image is estimated by the center of mass of the transformed liver mask.

3.2.3. FRAMEWORK I: THE SEQUENTIAL, LOCAL 4D REGISTRATION FRAMEWORK

Because the registration of images with large (local) deformations is prone to getting trapped in a local minimum, this framework aims to order the volumes in the sequence such that adjacent volumes exhibit only small deformation. Subsequently, the volumes are registered in this order by using the previous deformation field as starting point.

The displacement of the liver is largest in the superior-inferior direction due to breathing motion. Furthermore, since the liver's motion is quasi-periodic and continuous in this direction, pairs of dynamic volumes with comparable superior-inferior displacement appear very similar. Therefore, we sort all dynamic volumes in ascending order of superior/inferior displacement resulting in two ordered strands: one in superior and one in inferior direction.

One should observe that although our fixed image is the last image in the original DCE series, it may show up anywhere in a sorted strand (see Fig. 3.3(a)). This is due to the unpredictable phase of the breathing cycle – and hence the liver position – during which the last image was acquired. After the initial ordering, the two strands are now once more registered to the fixed image in an iterative way. In our explanation we focus on the images with a displacement in the superior direction, i.e. the part on the left from the fixed image in Fig. 3.3(a). The images with positive displacement are registered in the same way, but in reverse order.

Let us refer to the fixed image as image m in the sorted series, see Fig. 3.3(b). Initially, image $m-1$ in the series is registered to the fixed image (m) yielding a transformation $T(m-1, m)$. As explained above this registration is not sensitive to local minima in the objective function. Subsequently, image $m-2$ is registered to image $m-1$ to yield

transformation $T(m-2, m-1)$. Unfortunately, the concatenation of the transformations $T(m-2, m-1)$ and $T(m-1, m)$ does not yield optimal registration of image $m-2$ to the fixed image (m). This is due to the accumulation of small registration errors. However, it does bring image $m-2$ close to the optimum. As such, it is good starting point for the actual registration of image $m-2$. Next, $T(m-3, m-2)$ is concatenated with the ensuing transformation $T(m-2, m)$ to register image $m-3$ and this scheme is repeated until all images are registered to the fixed image.

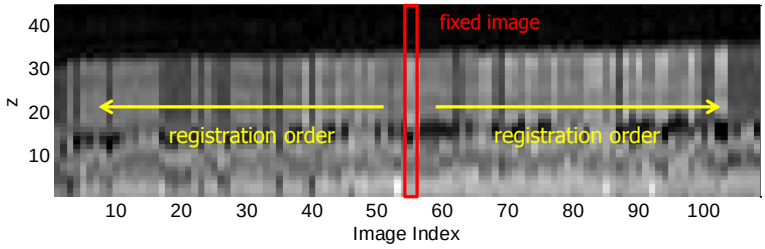

(a)

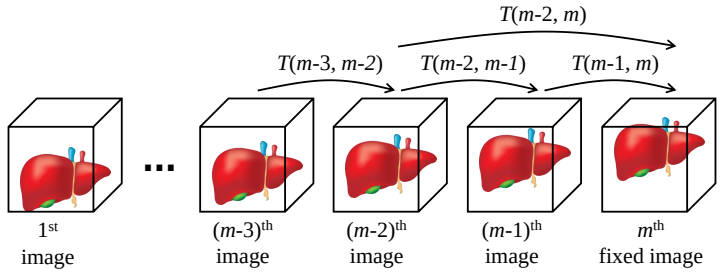

(b)

Figure 3.3: Concept of registration framework I: (a) registration order; (b) the two registration steps for each moving image.

3.2.4. FRAMEWORK II: THE GLOBAL 4D REGISTRATION FRAMEWORK

The second registration framework also relies on the liver mask's mean relative displacement albeit in a different manner. Furthermore, it also aims to initialize the registration of dynamic volumes to the last volume close to the global optimum.

Therefore, we assert that the displacement of a point in the liver is in its first approximation linearly related to the mean relative liver displacement in each spatial dimension. The displacement of liver points was already tentatively estimated by registering the last volume to each previous dynamic (Fig. 3.2, top part). Furthermore, the liver's mean relative displacement was obtained through the center of mass of the transformed liver mask (Fig. 3.2, bottom part).

The concept of the registration framework is illustrated in Fig. 3.4. Orange dots represent the estimated displacement of a point in the liver (vertically) as a function of the mean relative displacement of the liver mask (horizontally) in the superior-inferior direc-

tion. The dot located in the origin corresponds to the last image in the 4D DCE series; dots close to the origin represent images in which the liver mask is found to have small mean relative displacement and vice versa.

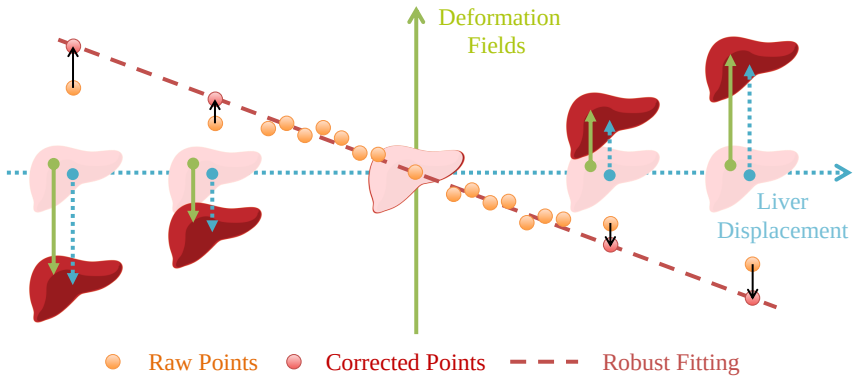

Figure 3.4: Concept of registration framework II: orange dots represent the mean relative displacement of the liver in z-direction (horizontally) against the displacement of a single point in z direction (vertically), estimated as illustrated in Fig. 3.2; the dashed red line is obtained by robust fitting to the orange dots; the offset of the orange dots to the fitted line is added to the point's initial displacement to improve the initial registration. The same concept is applied to x and y directions. The pink liver shape stands for the liver mask from the last dynamic; the burgundy shape represents the liver segmentation in a particular dynamic. The green and blue dots are exemplary points of which the initial deformations vectors are corrected.

In reality, the relation between the displacement of the points and the mean relative liver displacement is not perfectly proportional. Particularly for dynamic volumes associated with large liver displacement the displacement of points shows large variation. This is due to trappings in local minima and nonlinear deformation. Therefore, the dots in Fig. 3.4 close to the origin are considered more reliable than the ones away from the origin. Accordingly, we adopted a robust approach to fit a line to the data from each point in the liver mask (indicated by the dashed line) [27]. While doing so a higher weight was attributed to points closer to the origin.

After robust fitting, the offset of a point from the fitted line is taken to adjust the initially estimated displacement of the point. Applying this to each point for each spatial dimension is done to initialize the registration of the dynamic volume close to the global optimum. This scheme is repeated several times, after which the final registration is performed (notice that the iterations merely target to update the initial registration and are not based on adjusted registrations).

Finally, the obtained deformation fields need to be inverted in order to have the entire 4D series registered to the last image (as all prior registrations concerned matching the last DCE volume to the individual dynamics). To do so we adopted a simple fixed-point approach of which more details can be found in [28].

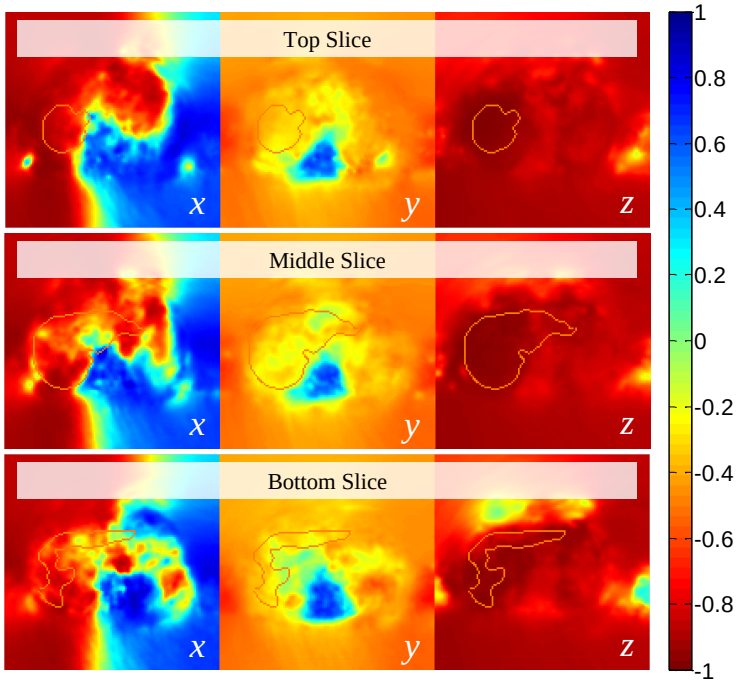

Figure 3.5: The correlation between the mean liver displacement and the displacements of points in $x-$, $y-$ and $z-$directions.

Fig. 3.5 shows the correlation (in color) between the mean liver displacement in the three orthogonal directions for all points in the image that was also used in Fig. 3.1 Three slices were arbitrarily chosen from the top, middle and bottom part of the liver. The contour of the liver mask is superimposed for reference. Notice that red tints represent negative correlation and blue tints reflect positive correlation. One may observe that the highest correlations are in superior-inferior (z) direction, a little bit lower correlations in anterior-posterior (x) direction, and the weakest correlation is observed in medial-lateral (y) direction. This is because the motion component due to breathing is smallest in medial-lateral direction. Fig. 3.6 serves to confirm this. In Fig. 3.6, the robust fitting between the mean liver mask displacement and a point's displacement in x-, y- and z-directions for three iterations is shown: $(u_0, v_0, w_0)_{i=1,2,3}$ are the initial point displacements and $(u_i, v_i, w_i)_{i=1,2,3}$ represent the point displacements after the i^{th} iteration. The figure shows that the correlation magnitude in all three directions becomes higher with increasing iteration number.

3.2.5. LIVER SIGNAL MODEL

In order to evaluate the benefit of our approach we will fit a pharmacokinetic model to the time-intensity signal in the segmented region. The residual of the fit will be considered as a measure for registration accuracy. Therefore, we adopt the liver model proposed by

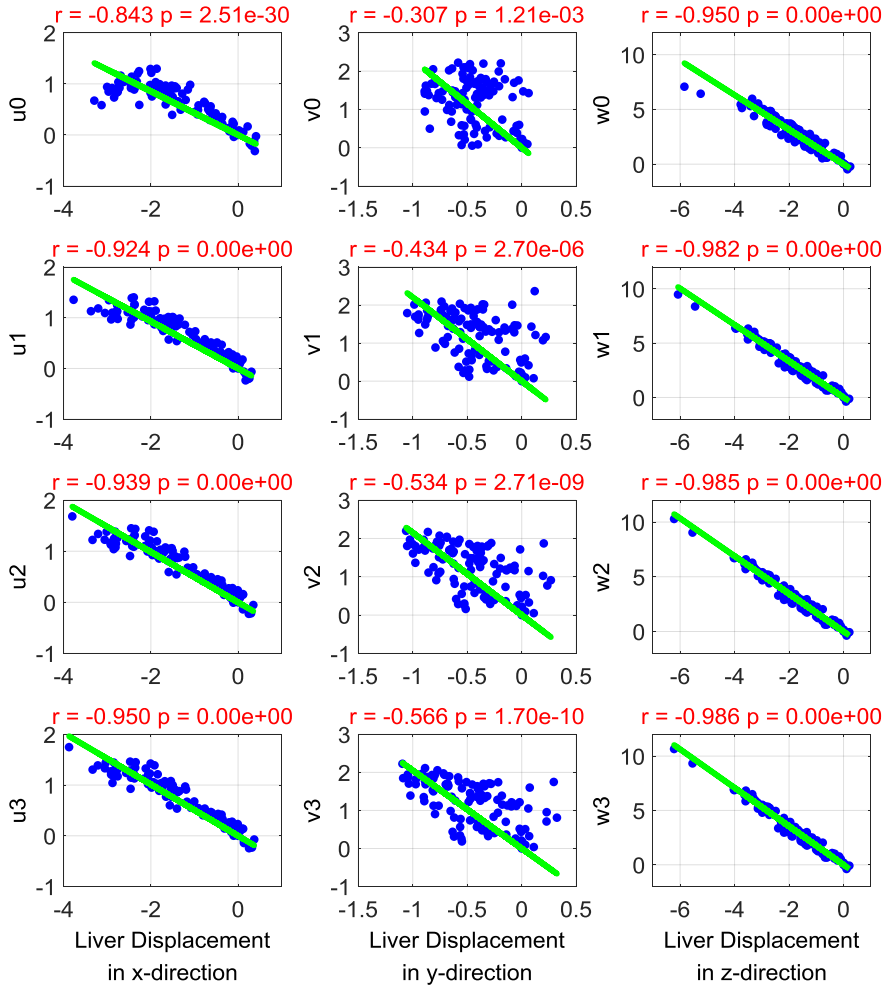

Figure 3.6: Robust fitting of a line to data from an arbitrarily selected point in the liver. The displacement of this point is shown across the entire DCR series as a function of the mean relative liver displacement in x, y and z-direction, for three iterations (from top to bottom). Above each subfigure Pearson's correlation coefficient is given, as well as the significance of the correlation.

S. Sourbron *et al.* [2], henceforth referred to as "the Sourbron model". This dual-inlets two-compartment uptake model was especially designed for the intracellular hepatobiliary contrast agent Primovist. The diagram in Fig. 3.7 [2] illustrates the model. The arterial input function (AIF) and venous input function (VIF) are the dual inlets representing the contrast agent concentration in the blood plasma supplied to the liver by the hepatic artery and the portal vein, respectively. These were obtained by averaging the top three of most enhancing time intensity curves of all voxels in regions manually delineated in the aorta (cranially from the hepatic artery) and the portal vein. T_A and T_V represent time delays and F_A and F_V are arterial and venous plasma flows, respectively. Furthermore, in the gray rectangle denoting liver tissue, the left circle represents the extracellular compartment and the right circle stands for the intracellular compartment, i.e. corresponding to the hepatocytes. As such, V_E is the extracellular volume and K_I represents the uptake rate of the hepatocytes represented by a volume V_I..

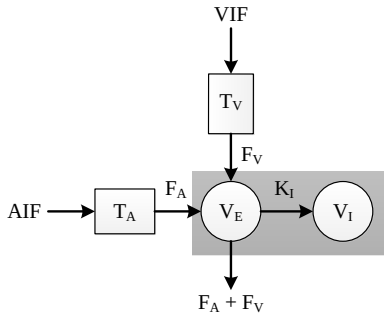

Figure 3.7: Sourbron model: a dual-inlets two-compartment uptake model for Gadoxetate disodium in the liver. The AIF and VIF are dual inlets into the liver, representing the concentration of the contrast agent over time entering from the hepatic artery and the portal vein. T_A and T_V are time delays. F_A and F_V are the arterial and venous plasma flows, respectively (in mL per minute per 100 mL). The gray rectangle represents the liver, the left circle the extracellular compartment V_E (in mL per 100 mL) and the right circle stands for the hepatocytes, i.e. the intracellular compartment. K_I (per minute) is the liver uptake rate.

Let C_E and C_I be the contrast agent concentrations in the extravascular, extracellular compartment and hepatocytes, respectively. Defining C_A and C_V as the concentrations of the AIF and VIF, the mass transport between the two compartments can be expressed as

$$\begin{cases} V_E \dfrac{dC_E}{dt}(t) = F_A C_A(t - T_A) + F_V C_V(t - T_V) - (F_A + F_V + K_I) C_E(t) \\ V_I \dfrac{dC_I}{dt}(t) = K_I C_E(t) \end{cases} \tag{3.7}$$

and the solution for the total liver tissue concentration ($C_T = V_E C_E + V_I C_I$) is

$$C_T(t) = \left[T_E \delta(t) + \frac{K_I}{F_A + F_V + K_I} \right] * \frac{e^{-\frac{t}{T_E}}}{T_E} * [F_A C_A(t - T_A) + F_V C_V(t - T_V)] \tag{3.8}$$

where * is the convolution operator, and $T_E(V_E/[F_A + F_V + K_I])$ represents the extracellular mean transit time..

3.3. RESULT AND DISCUSSION

THIS study included 11 patients diagnosed with colorectal liver metastasis (5), hepatocellular carcinoma (2) and benign (4). All scans were operated between December 2014 and Sep 2015. The final cohort (age range, 43 – 76 years; mean age, 62.0 years) included 6 men (age range, 50 – 70 years; mean age, 61.2 years) and 5 women (age range, 43 – 76 years; mean age, 63.0 years). The study was approved by the ethical review board of the Amsterdam University Medical Centers and registered under ID NL45755.018.13. Informed consent was obtained from all individual participants included in the study.

Abdominal DCE-MRI data were acquired on a 3T Philips Ingenia whole-body scanner via a 3D SPGR sequence. The acquisition parameter settings were T_E/T_R = 2.3/3.75 ms, FA = 15°, matrix size = 128×128×44, voxel size = 3×3×5 mm^3, acquisition time = 2.141 s for each volume; the sampling interval (between images) was 2.141 s for volumes 1-81, 30 s for volumes 82-98 and 60 s for volumes 99-108. The total imaging time was approximately 20 minutes. Patients held their breath during the acquisition of volumes 13-22, 33-42, 61-70 and 79-108.

Table 3.1: Description of state-of-the-art methods to which the proposed frameworks are compared.

Type	Description	Acronym	Parameter settings
State-of-the-art methods	PCA-based group-wise registration method	PCAG	FinalGridSpacingInPhysicalUnits = 4 NumberOfSpatialSamples = 1024
	Dense displacement sampling	DEEDS	-l 8 -s 1 -α 0.1 -r 50 -G 8x7x6x5x4x3x2x1 -L 8x7x6x5x4x3x2x1 -Q 1x1x1x1x1x1x1x1
Proposed registration frameworks	Sort volumes according to displacement (framework I)	SVAD	-α 0.1
	Optimized starting points by robust fitting (framework II)	OSPARF	-α 0.1

The two proposed registration frameworks will be compared against two state-of-the-art techniques, which are representative methods from different categories: group-wise registration [22] and discrete matching [15]. Essentially, both methods also target to avoid local minima, albeit in different ways. To achieve the best performance with a method, its parameters were optimized by performing a parameter sweep. Accordingly, all data that will be presented were obtained with the parameter setting that gave the lowest value for the objective function of a method. Further details of the methods are presented in Table 3.1.

Figure 3.8: Moving image (a) registered images obtained by the different registration methods (b-f) and the fixed image (g). Three (non-consecutive) slices were chosen (from top to bottom). In each image the outline from the fixed image is superimposed. The yellow arrows indicate mismatches.

3.3.1. EVALUATING THE REGISTRATION ACCURACY BY VISUAL INSPECTION

From the previously used data (Fig. 3.1) we selected the dynamic volume with the largest mean liver displacement. We chose to do so since the liver in this volume likely contains the largest deformation. Fig. 3.8 shows the outcome as this volume (raw moving image) is registered to the last image from the series (fixed image), using the methods from Table 3.1. Three slices from top to bottom through the volume are shown, on which the outline of the liver mask from the fixed image is superimposed to facilitate a visual comparison. Clearly, the mask's outline largely corresponds to the liver edge in the dynamic volume after application of PCAG, SSC or DEEDS registration. However, some mismatch can still be observed near the bottom of the liver as highlighted by the yellow arrows. In contrast, the results obtained with SVAD and OSPARF show a visually better alignment between the liver mask and the liver data signifying a better registration accuracy.

Fig. 3.9 visualizes the registration performance of the entire DCE series. As shown in Fig. 3.9(a), we selected one voxel in the liver and drew three orthogonal lines through it in $x-$, $y-$ and $z-$directions, indicated in blue, red and green. The intensity along these lines as a function of time is shown in Fig. 3.9(b), for the original volumes and after applying each registration method. Prior to registration, large fluctuations are visible in the signal over time due to breathing of the patient. The liver's upper boundary appears especially well registered by DEEDS, SVAD and OSPARF. Particularly near the lower edge of the liver SVAD and OSPARF outperform the other methods, see the arrows pointing this out.

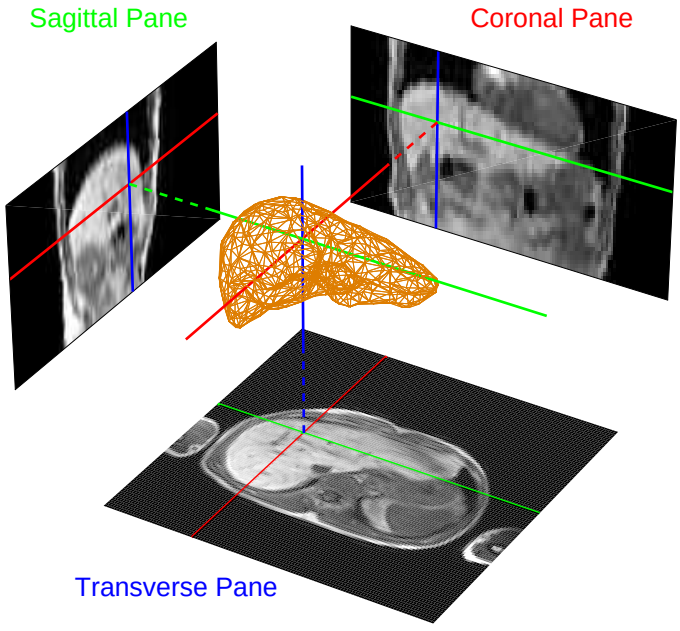

(a)

(b)

Figure 3.9: (a) Cross-sections of the liver on transverse, sagittal and coronal planes (projected to the sides for visualization purposes. (b) Intensity along the blue, red and green lines in (a) as a function of time as indicated by the image's border color. Images in the first column of (b) are prior to registration, images in the other columns are after registration by PCAG, SSC, DEEDS, SVAD and OSPARE, respectively.

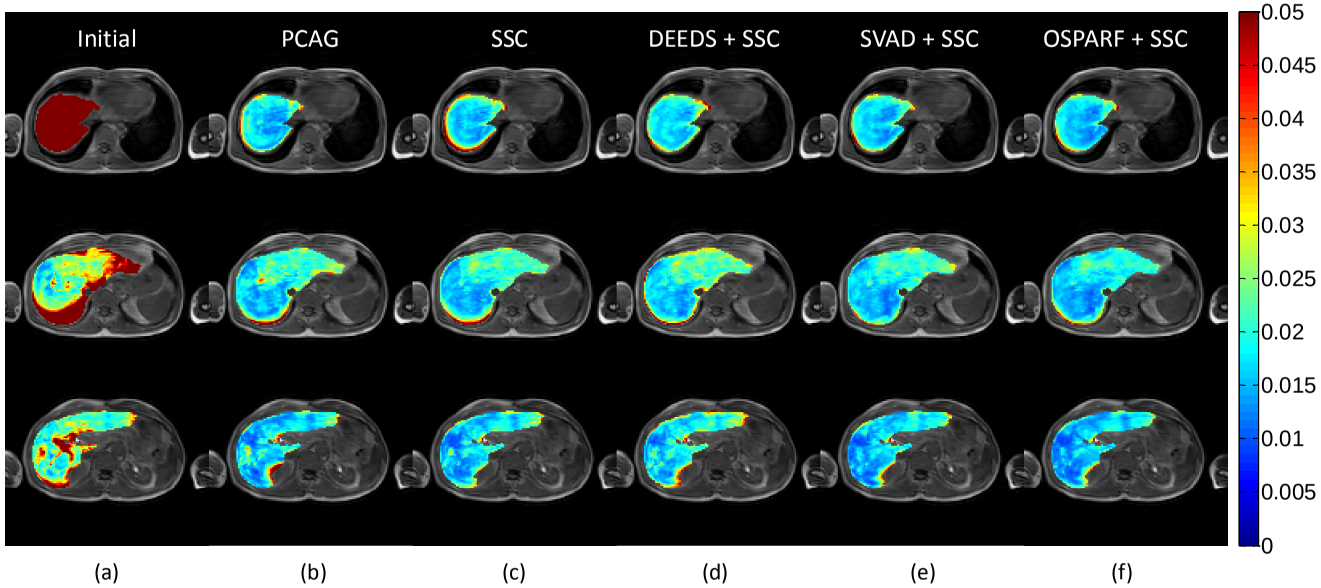

Figure 3.10: The RMSE of fitting Sourbron's model to the concentration time curves before registration (a) and after registration by means of PCAG, SSC, DEEDS, SVAD and OSPARF (e-f) in three slices (from top to bottom). Red colors represent large RMSE, blue colors small RMSE.

3.3.2. EVALUATION OF REGISTRATION ACCURACY BY MODEL FIT ERROR

In order to evaluate the registration performance quantitatively, we fitted Sourbron's liver model [2] to the concentration-time curves (CTCs) converted from the time-intensity curves (TICs) of each voxel in the liver. The residual of the fit (root mean square error, RMSE) was considered as a measure for registration accuracy. More details about the implementation of the model and fitting can be found in [2].

Fig. 3.10 shows the distribution of the RMSE after fitting Sourbron's model to all voxels inside the liver mask before and after registration using the methods from Table 3.1. Again three slices from the top to the bottom through the liver were selected for illustration purposes. It can be seen that PCAG and SSC yield regions with large RMSE at the edge of the liver, especially in the middle images (see the sharp red edges). Such regions are smaller with the DEEDS approach. The darker blue regions in the results from SVAD and OSPARF indicate even better registration, while OSPARF appears to perform a little bit better than SVAD.

Table 3.2: Average root mean square error (RMSE) and standard deviation (in brackets) after fitting Sourbron's model to all CTCs inside the liver mask for all patients in our dataset. Numbers with single underline are the minima, i.e. best results, per patient; numbers with double underlines represent second best outcomes.

Case	Initial	PCAG	SSC	DEEDS+SSC	SVAD+SSC	OSPARF+SSC
1	0.0721 ± 0.0741	0.0226 ± 0.0195	0.0253 ± 0.0289	0.0268 ± 0.0351	0.0224 ± 0.0243	0.0213 ± 0.0245
2	0.0506 ± 0.0448	0.0245 ± 0.0255	0.0198 ± 0.0150	0.0187 ± 0.0113	0.0180 ± 0.0098	0.0170 ± 0.0105
3	0.0584 ± 0.0478	0.0343 ± 0.0263	0.0340 ± 0.0258	0.0351 ± 0.0267	0.0350 ± 0.0290	0.0315 ± 0.0245
4	0.0693 ± 0.0481	0.0492 ± 0.0304	0.0435 ± 0.0258	0.0423 ± 0.0250	0.0405 ± 0.0229	0.0404 ± 0.0233
5	0.0649 ± 0.0788	0.0270 ± 0.0171	0.0275 ± 0.0184	0.0284 ± 0.0191	0.0249 ± 0.0145	0.0242 ± 0.0144
6	0.0654 ± 0.0515	0.0340 ± 0.0267	0.0335 ± 0.0197	0.0337 ± 0.0199	0.0316 ± 0.0179	0.0300 ± 0.0166
7	0.0633 ± 0.0495	0.0329 ± 0.0280	0.0249 ± 0.0180	0.0254 ± 0.0156	0.0225 ± 0.0132	0.0222 ± 0.0132
8	0.0700 ± 0.0593	0.0389 ± 0.0400	0.0317 ± 0.0392	0.0301 ± 0.0318	0.0262 ± 0.0284	0.0264 ± 0.0349
9	0.0365 ± 0.0623	0.0192 ± 0.0134	0.0191 ± 0.0141	0.0195 ± 0.0132	0.0178 ± 0.0122	0.0177 ± 0.0120
10	0.0408 ± 0.0323	0.0266 ± 0.0167	0.0258 ± 0.0214	0.0263 ± 0.0244	0.0248 ± 0.0268	0.0241 ± 0.0205
11	0.0557 ± 0.0532	0.0455 ± 0.0558	0.0394 ± 0.0473	0.0373 ± 0.0439	0.0320 ± 0.0268	0.0331 ± 0.0361
Avg	0.0584 ± 0.0563	0.0329 ± 0.0298	0.0302 ± 0.0270	0.0302 ± 0.0263	0.0278 ± 0.0232	0.0271 ± 0.0233

Table 3.2 shows the average RMSE and standard deviation of all voxels in the liver mask for each patient. OSPARF provides the smallest average RMSE in 9/11 patients and SVAD is second best in 9/11 patients. The last row in the table shows the average result of all patients. OSPARF ranks first and SVAD is the second best.

3.3.3. EVALUATION OF ACCURACY BY MEAN TARGET REGISTRATION ERROR

Synthetic MR images were generated by artificially deforming the fixed images of each patient (last image of the DCE series). The artificial deformations were generated by averaging the deformations fields of the five registration methods for each dynamic volume and patient. As such, the ground truth is known, enabling to calculate the mean target registration error for each point in the liver. We did so since it appeared not feasible to reliably identify landmarks in these data. This was due to the low resolution of the data and absence of highly characteristic points in or around the liver in our data. Eventually, the artificially deformed fixed images were registered to the (undeformed) fixed images.

Table 3.3 collates the MTRE outcomes for each patient and registration method. It

Table 3.3: Mean target registration error (MTRE) and corresponding standard deviation in the liver on synthetic MRI data. Synthetic images were generated by artificially deforming the fixed images, i.e. last image in the DCE series. Numbers with single underline are the best results per patient; Numbers with double underlines are second best outcomes. The unit is mm.

Case	Initial	PCAG	SSC	DEEDS+SSC	SVAD+SSC	OSPARF+SSC
1	11.3973 ± 6.9890	2.3498 ± 1.3307	1.3558 ± 0.7180	1.2960 ± 0.7435	1.0603 ± 0.5761	1.1821 ± 0.6177
2	7.5174 ± 5.4657	3.4517 ± 2.0918	1.3509 ± 0.7049	1.3324 ± 0.7395	1.0893 ± 0.5988	1.2171 ± 0.5998
3	7.4822 ± 6.4074	3.2546 ± 2.4945	1.4064 ± 0.7120	1.3400 ± 0.6919	1.1106 ± 0.5683	1.3064 ± 0.6534
4	8.0321 ± 7.2211	3.3593 ± 2.5285	1.4247 ± 0.7131	1.3400 ± 0.7342	1.1543 ± 0.5812	1.3743 ± 0.6600
5	8.4332 ± 7.6378	1.9549 ± 1.4420	1.1797 ± 0.6579	1.1876 ± 0.6412	0.9744 ± 0.5095	1.1070 ± 0.5941
6	8.7288 ± 6.4925	2.2287 ± 1.3690	1.2975 ± 0.6806	1.2851 ± 0.7344	1.0637 ± 0.5808	1.1730 ± 0.6002
7	11.0906 ± 11.3667	2.3525 ± 1.8548	1.2163 ± 0.7121	1.3159 ± 0.7939	1.1283 ± 0.6689	1.1327 ± 0.6311
8	11.6533 ± 10.0273	4.0130 ± 3.3391	1.4070 ± 0.8157	1.2531 ± 0.6788	1.0589 ± 0.5535	1.2481 ± 0.6160
9	5.5437 ± 2.9003	2.7758 ± 1.4367	1.3022 ± 0.6239	1.2667 ± 0.6927	1.0691 ± 0.5209	1.3098 ± 0.6152
10	6.6298 ± 5.9773	2.7708 ± 2.0664	1.3100 ± 0.6525	1.2569 ± 0.6528	1.0859 ± 0.5444	1.2693 ± 0.6176
11	11.0175 ± 9.4377	5.2308 ± 4.7569	1.3939 ± 0.8006	1.3642 ± 0.8069	1.1263 ± 0.5664	1.3001 ± 0.6289
Avg	8.0234 ± 7.4431	2.9045 ± 2.4578	1.3269 ± 0.6905	1.2862 ± 0.6978	1.0622 ± 0.5583	1.2474 ± 0.6175

shows that SVAD and OSPARF perform best and second best on average. Furthermore, we also performed this experiment while calculating the MTRE over the whole volume, instead of over the liver only. The result can be seen in Table 3.3. OSPARF performs best on 10/11 patients while SVAD is in the second place on 8/11 patients. The average performance shows that OSPARF has the highest accuracy.

Table 3.4: Mean target registration error (MTRE) and corresponding standard deviation over the whole volume on synthetic MRI data. Synthetic images were generated by artificially deforming the fixed images, i.e. last image in the DCE series. Numbers with single underline are the best results per patient; Numbers with double underlines are second best outcomes. The unit is mm.

Case	Initial	PCAG	SSC	DEEDS+SSC	SVAD+SSC	OSPARF+SSC
1	6.3576 ± 5.7787	2.9796 ± 2.2085	1.4499 ± 0.7980	1.3287 ± 0.7845	1.3368 ± 0.9809	1.1564 ± 0.6353
2	4.7964 ± 4.8542	2.6388 ± 2.4868	1.2468 ± 0.7184	1.2942 ± 0.7960	1.1578 ± 0.7281	1.0550 ± 0.6045
3	4.0032 ± 4.1393	2.0698 ± 1.8384	1.2041 ± 0.6935	1.2850 ± 0.7501	1.1718 ± 0.7309	1.0949 ± 0.6322
4	4.7965 ± 5.5607	2.7673 ± 3.1623	1.2448 ± 0.7688	1.2685 ± 0.8077	1.1996 ± 0.7782	1.1781 ± 0.6869
5	4.4344 ± 5.1465	2.0915 ± 1.9862	1.2431 ± 0.7253	1.2188 ± 0.7300	1.1837 ± 0.9309	1.0572 ± 0.6299
6	4.4992 ± 4.6482	2.0726 ± 1.7639	1.2397 ± 0.7000	1.2606 ± 0.7688	1.1465 ± 0.7388	1.0541 ± 0.6211
7	5.8003 ± 7.1173	2.6538 ± 2.9433	1.2988 ± 0.8340	1.3175 ± 0.7950	1.4200 ± 1.0202	1.1647 ± 0.7120
8	6.0004 ± 6.7081	3.1274 ± 3.2867	1.3214 ± 0.8464	1.2840 ± 0.8157	1.1694 ± 0.7646	1.1501 ± 0.6691
9	3.6446 ± 3.0243	1.9670 ± 1.6482	1.1227 ± 0.6145	1.2471 ± 0.7299	1.0949 ± 0.6326	1.1034 ± 0.6177
10	3.3359 ± 4.1887	1.8115 ± 1.9354	1.0678 ± 0.6613	1.1979 ± 0.7310	1.0572 ± 0.6507	0.9898 ± 0.6169
11	5.5793 ± 6.0905	3.1303 ± 3.5519	1.2956 ± 0.8034	1.3266 ± 0.8220	1.1404 ± 0.6531	1.1141 ± 0.6269
Avg	5.0263 ± 5.5703	2.5904 ± 2.6703	1.2755 ± 0.7605	1.3013 ± 0.7929	1.2099 ± 0.8072	1.1306 ± 0.6594

3.3.4. EVALUATION OF REGISTRATION ACCURACY BY DICE COEFFICIENT AND MEAN SURFACE DISTANCE

The liver was outlined manually in the fixed volume (last image from the DCE series) and in the dynamic volume with the largest liver placement. In this way we selected the moving volume in which the largest deformation was expected. A research fellow supervised by an abdominal radiologist performed this task for each patient. Subsequently, the Dice

Coefficient (DC) was calculated to express the overlap before and after registration. Furthermore, the mean surface distance (MSD) between the outlines was also calculated. The MSD was determined as the average shortest distance from outline points in the fixed image to points in the moving image and vice versa.

Table 3.5 and Table 3.6 summarize the assessments by DC and MSD respectively for each registration method. OSPARF has the highest DC and lowest MSD on 6/10, cases and SVAD in 4/10 cases. Both methods perform better than the existing registration methods in both aspects on almost all patients. It is just the DEEDS approach that comes second regarding DC on two patients.

Table 3.5: Dice Coefficient of manually annotated liver outlines between the dynamic volume with largest liver mask displacement and the fixed image before and after registration. Numbers with single underline are the best results per patient; Numbers with double underlines are second best outcomes.

Case	Initial	PCAG	SSC	DEEDS+SSC	SVAD+SSC	OSPARF+SSC
1	0.5245	0.8546	0.8262	0.8567	0.8696	0.8677
2	0.6072	0.8117	0.8672	0.8924	0.9039	0.8964
3	0.7454	0.8930	0.9047	0.9101	0.9113	0.9106
4	0.6077	0.8006	0.8714	0.8701	0.9028	0.9155
5	0.5076	0.8741	0.9069	0.9175	0.9280	0.9383
6	0.6918	0.8993	0.8933	0.9000	0.9028	0.9010
7	0.5641	0.8459	0.8762	0.8863	0.8945	0.8874
8	0.5541	0.8121	0.8680	0.8852	0.8864	0.8863
9	0.7846	0.8850	0.8931	0.8838	0.9018	0.9032
10	0.7192	0.8326	0.8649	0.8548	0.8672	0.8670
11	0.6686	0.7708	0.8501	0.8604	0.8623	0.8728
Avg	0.6341	0.8436	0.8747	0.8834	0.8937	0.8951

Table 3.6: Mean surface distance (mm) of manually annotated liver outlines between the dynamic volume with largest liver mask displacement and the fixed image before and after registration. Numbers with single underline are the best results per patient; Numbers with double underlines are second best outcomes.

Case	Initial	PCAG	SSC	DEEDS+SSC	SVAD+SSC	OSPARF+SSC
1	13.3993	4.6619	5.9355	4.6638	4.5296	4.6285
2	9.9083	6.1134	4.4018	3.7185	3.3343	3.6000
3	10.0374	4.8161	4.3861	4.1545	4.0737	4.1979
4	15.3564	8.4413	5.7826	5.9666	4.6430	4.1643
5	16.0148	4.7404	3.8315	3.2375	2.7697	2.5777
6	9.9854	3.7624	3.9875	3.5706	3.5092	3.6256
7	15.7158	5.6104	4.9210	4.5990	4.3421	4.4323
8	13.7681	6.2928	4.7429	4.2810	4.2259	4.3963
9	7.4760	4.3054	4.1581	4.5692	3.9757	3.9427
10	10.0095	6.3983	5.4182	5.8998	5.2488	5.2834
11	10.6872	7.5771	5.4479	5.0519	5.0366	4.7735
Avg	12.0326	5.7018	4.8194	4.5193	4.1535	4.1475

3.4. SUMMARY AND CONCLUSION

In this paper, two novel frameworks for 4D registration of DCE MRI data were proposed to reduce the sensitivity of image registration methods to local minima in the objective

function.

The first framework (SVAD) imposed an ordering to the images by increasing distance in the superior-inferior direction with respect to a reference image. Subsequently, the images were sequentially registered to the reference image starting with the images with the shortest distance. Hypothetically, the registration of an image was initialized close to the global optimum by combining its registration to the preceding image with the registration of the latter to the reference.

The second framework (OSPARF) assumed a linear relation between the mean relative displacement of the liver and the displacement of individual points in the liver. It also aimed to initialize the registration close to the global optimum by iteratively adjusting the initial registration based on this asserted relation.

The proposed methods were compared to two state-of-art methods that also target to avoid local minima. The performance of the registration methods was quantitatively assessed using the fit error of a pharmacokinetic model (Table 3.2) and the target registration error on synthetically deformed images (Table 3.3).

The proposed methods outperformed the existing methods in all but a minority of cases. Furthermore, the OSPARF method appeared to have a slight edge over SVAD, although the difference is not large.

There are several limitations of our work. First, the proposed methods relied on a segmentation of the liver. A delineation of the organ of interest would also needed for any other application and this might not always be a trivial task. In our work, the segmentation was simplified to a large extent as a liver specific contrast agent was used. We do consider developing a joint registration and segmentation method, i.e. do the registration and segmentation simultaneously, in order to become less dependent on the quality of the first and last image in the DCE series.

The second limitation is that the number of patients we have is rather small. Clearly, evaluating the performance of registration on a large number of subjects would be even more convincing, even though the number of dynamic volumes per patient is quite large. Unfortunately, we are restricted to a small number of patients as our work is part of a pilot study into the uptake rate of the contrast medium into the liver cells.

We hypothesize that our methods may also aid in the initialization of other registration methods, if a measure of proximity can be defined for the data.

REFERENCES

[1] A. Jackson, D. L. Buckley, and G. J. M. Parker, *Dynamic contrast-enhanced magnetic resonance imaging in oncology* (Springer, 2005).

[2] S. Sourbron, W. H. Sommer, M. F. Reiser, and C. J. Zech, *Combined Quantification of Liver Perfusion and Function with Dynamic Gadoxetic Acid-enhanced MR Imaging,* Radiology **263**, 874 (2012).

[3] A. Sotiras, C. Davatzikos, and N. Paragios, *Deformable medical image registration: A survey,* IEEE Transactions on Medical Imaging **32**, 1153 (2013), arXiv:NIHMS150003 .

[4] F. G. Zöllner, R. Sance, P. Rogelj, M. J. Ledesma-Carbayo, J. Rørvik, A. Santos, and A. Lundervold, *Assessment of 3D DCE-MRI of the kidneys using non-rigid image registration and segmentation of voxel time courses,* Computerized Medical Imaging and Graphics **33**, 171 (2009).

[5] D. Zikic, S. Sourbron, X. Feng, H. J. Michaely, A. Khamene, and N. Navab, *Automatic alignment of renal DCE-MRI image series for improvement of quantitative tracer kinetic studies,* Proceedings of SPIE **6914**, 691432 (2008).

[6] M. P. Heinrich, M. Jenkinson, M. Bhushan, T. Matin, F. V. Gleeson, S. M. Brady, and J. A. Schnabel, *MIND: Modality independent neighbourhood descriptor for multi-modal deformable registration,* Medical Image Analysis **16**, 1423 (2012).

[7] M. P. Heinrich, M. Jenkinson, B. W. Papiez, S. M. Brady, and J. A. Schnabel, *Towards realtime multimodal fusion for image-guided interventions using self-similarities,* in *Lecture Notes in Computer Science (including subseries Lecture Notes in Artificial Intelligence and Lecture Notes in Bioinformatics)*, Vol. 8149 LNCS (2013) pp. 187–194.

[8] J. Nocedal and S. J. Wright, *Analysis*, Vol. 43 (1999) pp. 164–75, arXiv:NIHMS150003 .

[9] R. Fletcher and C. M. Reeves, *Function minimization by conjugate gradients,* The Computer Journal **7**, 149 (1964), arXiv:1011.1669v3 .

[10] W. Press, S. Teukolsky, W. Vetterling, B. Flannery, E. Ziegel, W. Press, B. Flannery, S. Teukolsky, and W. Vetterling, *Technometrics*, Vol. 29 (1987) p. 501, arXiv:arXiv:1011.1669v3 .

[11] D. Zikic, A. Kamen, and N. Navab, *Revisiting Horn and Schunck: Interpretation as Gauss-Newton Optimisation,* Procedings of the British Machine Vision Conference 2010 , 113.1 (2010).

[12] Y. Boykov and V. Kolmogorov, *An experimental comparison of min-cut/max- flow algorithms for energy minimization in vision,* IEEE Transactions on Pattern Analysis and Machine Intelligence **26**, 1124 (2004), arXiv:0703101v1 [cs] .

[13] J. Pearl and a. Hasman, *International Journal of Bio-Medical Computing*, Vol. 28 (1991) p. 554, arXiv:1558604790 .

[14] B. Glocker, N. Komodakis, G. Tziritas, N. Navab, and N. Paragios, *Dense image registration through MRFs and efficient linear programming,* Medical Image Analysis **12**, 731 (2008).

[15] M. P. Heinrich, M. Jenkinson, M. Brady, and J. A. Schnabel, *MRF-Based deformable registration and ventilation estimation of lung CT,* IEEE Transactions on Medical Imaging **32**, 1239 (2013).

[16] C. T. Metz, S. Klein, M. Schaap, T. van Walsum, and W. J. Niessen, *Nonrigid registration of dynamic medical imaging data using nD+t B-splines and a groupwise optimization approach,* Medical Image Analysis **15**, 238 (2011).

[17] H. Xu and X. Li, *A symmetric 4D registration algorithm for respiratory motion modeling,* Lecture Notes in Computer Science (including subseries Lecture Notes in Artificial Intelligence and Lecture Notes in Bioinformatics) **8150 LNCS**, 149 (2013).

[18] Z. Li, J. A. Tielbeek, M. W. Caan, C. A. Puylaert, M. L. Ziech, C. Y. Nio, J. Stoker, L. J. Van Vliet, and F. M. Vos, *Expiration-Phase Template-Based Motion Correction of Free-Breathing Abdominal Dynamic Contrast Enhanced MRI,* IEEE Transactions on Biomedical Engineering **62**, 1215 (2015).

[19] J. Hamm, D. H. Ye, R. Verma, and C. Davatzikos, *GRAM: A framework for geodesic registration on anatomical manifolds,* Medical Image Analysis **14**, 633 (2010), arXiv:NIHMS150003 .

[20] Q. Feng, Y. Zhou, X. Li, Y. Mei, Z. Lu, Y. Zhang, Y. Feng, Y. Liu, W. Yang, and W. Chen, *Liver DCE-MRI Registration in Manifold Space Based on Robust Principal Component Analysis,* Scientific Reports **6**, 34461 (2016).

[21] V. Hamy, N. Dikaios, S. Punwani, A. Melbourne, A. Latifoltojar, J. Makanyanga, M. Chouhan, E. Helbren, A. Menys, S. Taylor, and D. Atkinson, *Respiratory motion correction in dynamic MRI using robust data decomposition registration - Application to DCE-MRI,* Medical Image Analysis **18**, 301 (2014).

[22] W. Huizinga, D. H. J. Poot, J. M. Guyader, R. Klaassen, B. F. Coolen, M. Van Kranenburg, R. J. M. Van Geuns, A. Uitterdijk, M. Polfliet, J. Vandemeulebroucke, A. Leemans, W. J. Niessen, and S. Klein, *PCA-based groupwise image registration for quantitative MRI,* Medical Image Analysis **29**, 65 (2016).

[23] T. Zhang, Z. Li, J. H. Runge, C. Lavini, J. Stoker, T. van Gulik, L. J. van Vliet, and F. M. Vos, *Improved registration of DCE-MR images of the liver using a prior segmentation of the region of interest,* Proc. SPIE **9784**, 978443 (2016).

[24] Y. Zhang, B. J. Matuszewski, L.-K. Shark, and C. J. Moore, *Medical Image Segmentation Using New Hybrid Level-Set Method,* in *2008 Fifth International Conference BioMedical Visualization: Information Visualization in Medical and Biomedical Informatics* (2008) pp. 71–76.

[25] V. Caselles, R. Kimmel, and G. Sapiro, *Geodesic Active Contours,* International Journal of Computer Vision **22**, 61 (1997).

[26] T. F. Chan and L. a. Vese, *Active contours without edges.* IEEE transactions on image processing : a publication of the IEEE Signal Processing Society **10**, 266 (2001).

[27] P. W. Holland and R. E. Welsch, *Robust regression using iteratively reweighted least-squares,* Communications in Statistics - Theory and Methods **6**, 813 (1977).

[28] M. Chen, W. Lu, Q. Chen, K. J. Ruchala, and G. H. Olivera, *A simple fixed-point approach to invert a deformation field.* Medical physics **35**, 81 (2008).

4

A Pharmacokinetic Model with Separate Arrival Time for Two Inputs and Compensating for Varying Flip-angle in DCE-MRI with Gd-EOB-DTPA

Pharmacokinetic models facilitate assessment properties of the micro-vascularization based on DCE-MRI data. However, accurate pharmacokinetic modeling in the liver is challenging since it has two vascular inputs and is subject to large deformation and displacement due to respiration.

We propose an improved pharmacokinetic model for the liver that (1) analytically models the arrival-time of the contrast agent for both inputs separately; (2) implicitly compensates for signal fluctuations that can be modeled by varying applied flip-angle e.g. due to B_1-inhomogeneity.

Orton's AIF model is used to analytically represent the vascular input functions. The inputs are independently embedded into the Sourbron model. B_1-inhomogeneity-driven variation of flip-angles are accounted for to justify the voxel's displacement with respect to a pre-contrast image.

The new model was shown to yield lower root mean square error (RMSE) residues after fitting the model to all but a minority of voxels compared to Sourbron's approach. Furthermore, it outperformed this existing model in the majority of voxels according to three model-selection criteria.

Other types of pharmacokinetic models may also benefit from our approaches, since the techniques are generally applicable.

4.1. INTRODUCTION

DYNAMIC Contrast-Enhanced MRI (DCE-MRI) is a technique that can be applied to assess properties of the micro-vascularization in organs such as the liver, breast, and kidney [1][2]. Pharmacokinetic (PK) modeling in the liver is more challenging then the rest of the body since the liver has two vascular inputs: the hepatic artery and the portal vein Furthermore, contrary to standard Gd-based contrast media, the hepatobiliary contrast agent Gadoxetate disodium (Primovist^{TM}, Bayer pharmaceutical) is also taken up by the hepatocytes. As such an additional compartment should be taken into account in a pharmacokinetic model. Finally, the uptake rate of the hepatocytes is low and for this reason DCE-MRI may take up to 20 minutes or more. During image acquisition the liver can experience large deformations and displacements, which may significantly influence the signal intensity (e.g. due to B_1-inhomogeneity). These issues result in the fact that accurate pharmacokinetic modeling in the liver is a far from trivial.

4.1.1. RELATED WORK

Quantitative analysis of liver function with MRI using Gd-EOB-DTPA in rabbits was first proposed by Ryeom *et al.* [3] in 2004. Using a deconvolution technique, the estimated hepatic extraction fraction (HEF) showed correlation with liver function measured through the plasma's retention rate after indocyane green injection. Subsequently, Nilsson *et al.* [4] applied the same liver model to humans with a more efficient deconvolution technique called truncated singular value decomposition (TSVD). However, this deconvolution approach regarded the hepatic artery as the sole input, and ignored the portal vein. A dual-input one-compartmental model was already proposed in 2002, but this model focused on extracellular contrast agents such as Gd-DTPA (Magnevist, Bayer Schering Pharma, Berlin, Germany) [5]. By adding an intracellular compartment, Sourbron *et al.* [2] created a dual-input, two-compartmental model that accounted for Gd-EOB-DTPA metabolization by the hepatic cells in 2012. One limitation of Sourbron's model is that it ignores the extraction rate of hepatocytes, i.e. the efflux to the bile canaliculi. To solve this, Ulloa *et al.* [6] modeled the transport of the contrast agent from the hepatocytes to the bile via nonlinear Michaelis-Menten kinetics in humans. Georgiou *et al.* [8] tried to simplify the efflux transport by a simple linear approximation. Recently, Ning *et al.* [9] correlated pharmacokinetic parameters estimated from different models with a blood chemistry test. It was found that the relative liver uptake rate estimated from the model without bile efflux transport significantly correlated with direct bilirubin (r=-0.52, p=0.015), prealbumin (r=0.58, p=0.015) and prothrombin time (r=-0.51, p=0.026). Furthermore, only insignificant correlations were found using the model with efflux transport. Accordingly, our work regards Sourbron's model [2] as the starting point, i.e. opting for a model without bile efflux transport.

In Sourbron's approach, the delay of the arterial input is empirically determined by the best model fit over a discrete set of values. This might limit the accuracy of the PKM parameter estimation and could restrict its applicability. Furthermore, the method does not take the effects of liver motion on the signal intensity into account. Such motion not only causes misalignment, which should be compensated for using image registration,

but it may also induce other signal fluctuation, due to motion-induced time-varying B_1-inhomogeneity caused by the movement of the bowel in the field of view.

Previously, several papers investigated the influence of B1-inhomogeneity on pharmacokinetic modeling. For example, Park *et al.* [10] and Sengupta et al [11] conducted a simulation and an experimental study respectively showing that a small degree of B_1-inhomogeneity can cause a significant error in the estimated PKM parameters. Alternatively, Van Schie *et al.* [12] combined variable flip angle (VFA) and Look-Locker (LL) sequences to obtain a B1-inhomogeneity map for DCE imaging. Such a B_1-map may also be obtained by means of the DREAM sequence [13]. Essentially, all these methods attempt to correct the B_1-inhomogeneity based on auxiliary sequences. However, this not only makes the imaging even more time-consuming, it conventionally yields static B_1-maps whereas fluctuations due to motion remain hard to account for.

4.1.2. OBJECTIVE

In this paper we aim to improve the accuracy of pharmacokinetic modeling of liver DCE MRI data. Therefore, two novelties are introduced in the PK modeling. First, the arterial input function proposed by Orton is integrated into Sourbron's PK model. This enables that the arrival times of contrast from the portal vein and the hepatic artery are separately included in the model and estimated simultaneously with the PK model parameters. Secondly, the deformation and displacement of the liver is estimated and used to correct for changes in signal intensity such as the ones caused by B_1-inhomogeneities.The effectiveness of the new model will be assessed by several experiments.

4.2. MATERIALS AND METHODS

4.2.1. DATA ACQUISITION

THIS study included 11 patients diagnosed with colorectal liver metastasis (5), hepatocellular carcinoma (2) and benign (4). All scans were operated between December 2014 and Sep 2015. The final cohort (age range, 43 – 76 years; mean age, 62.0 years) included 6 men (age range, 50 – 70 years; mean age, 61.2 years) and 5 women (age range, 43 – 76 years; mean age, 63.0 years). The study was approved by the ethical review board of the Amsterdam University Medical Centers and registered under ID NL45755.018.13. Informed consent was obtained from all individual participants included in the study.

DCE-MRI data were acquired on a 3T Philips Ingenia whole-body scanner at the AMC by means of a T_1-weighted 3D Spoiled Gradient Echo sequence. The x-axis of the data corresponds to the anterior-posterior direction, the y-axis to the left-right direction and the z-axis to the superior-inferior direction, as show in Fig. 4.1(a). The acquisition parameter settings were T_E/T_R = 2.30/3.75 ms, FA = 15°, matrix size = 128×128×44, voxel size = 3×3×5 mm^3, acquisition time = 2.141 s for each volume; sampling interval (between images) was 2.141 s for volumes 1-81, 30 s for volumes 82-98, and 60 s for volumes 99-108. The total imaging time was approximately 20 minutes. Volumes 1-19 were acquired in the pre-contrast stage. Subjects held their breath during the acquisition of volumes 13-22, 33-42, 61-70 and 79-108. 11 subjects were included for this research.

In addition, dual refocusing echo acquisition mode (DREAM) images [13] were acquired to quantify the extent of the B_1-inhomogeneity before the DCE sequence was ac-

quired. The acquisition parameter settings were matrix size = 64×64×30, voxel size = 8.28×8.28×8.80 mm^3, nominal STEAM flip-angle $\alpha = 60°$, nominal imaging flip-angle $\beta = 10°$, $TE_{STE} = 1.06$ ms, $TE_{FID} = 2.30$ ms, $T_R = 3.84$ ms. Essentially, the DREAM sequence produces a map, in which the value of every voxel represents the ratio between the real flip-angle and the programmed flip-angle. We will refer to it as the 'zeta' map.

4.2.2. IMAGE REGISTRATION AND LIVER SEGMENTATION

Image registration is required to achieve spatial correspondence between voxels of the DCE-MRI data prior to PK modeling. In this work, each 4D DCE-MR dynamic is registered to the last dynamic volume. In order to do so, we apply the registration framework Optimized Starting Points by Robust Fitting (OSPARF). It is described in Chapter 3, in which the registration kernel is the self-similarity context (SSC) method [14], which is a state-of-the-art technique for multi-modal image registration. Essentially, it is a patch-based descriptor of the structure in a certain neighborhood layout N, defined as:

$$SSC\left(I,\mathbf{x},\mathbf{y}\right) = \exp\left[-\frac{D\left(I,\mathbf{x},\mathbf{y}\right)}{V\left(I,\mathbf{x}\right)}\right] \mathbf{x},\mathbf{y} \in N \tag{4.1}$$

in which I is an image, $\mathbf{x}$ and $\mathbf{y}$ are the center locations of two patches within N, and D is the distance between the two image patches measured by the sum of squared differences (SSD):

$$D\left(I,\mathbf{x_1},\mathbf{x_2}\right) = \sum_{\mathbf{y}\in N}\left[I\left(\mathbf{x}_1+\mathbf{y}\right) - I\left(\mathbf{x}_2+\mathbf{y}\right)\right]^2 \tag{4.2}$$

and $V(I, N)$ is the mean of the patch distances in neighborhood N:

$$V\left(I,N\right) = \frac{1}{num\left(N\right)}\sum_{\mathbf{x},\mathbf{y}\in N} D\left(I,\mathbf{x},\mathbf{y}\right) \tag{4.3}$$

The SSC operator is based on all distances in a six neighborhood (with a Euclidean distance of $\sqrt{2}$ between them), while the central pixel is excluded from N.

SSC registration can be described as

$$\mathbf{u}^* = \arg\min_{\mathbf{u}}\left\{\sum_{\mathbf{x}}\left[\frac{1}{|R|}\sum_{\mathbf{r}\in R}\left|SSC\left(I,\mathbf{x},\mathbf{r}\right) - SSC\left(J,\mathbf{x},\mathbf{r}\right)\right|\right] + \alpha\left|\nabla\mathbf{u}\left(\mathbf{x}\right)\right|^2\right\} \tag{4.4}$$

where $\mathbf{u} = (u, v, w)$ is the deformation field and α the regularization parameter, i.e. a coefficient that weighs the regularization term.

In this paper we follow the default setup as introduced in [14]: $R = 3$, $N = N_6$, i.e. a six-connected neighborhood, patch size $D = 3$, and the regularization coefficient $\alpha = 0.1$.

Furthermore, we segment the liver, defining our region of interest, using a segmentation method that we proposed previously [15]. As we apply a liver-specific contrast agent, the surrounding organs show less signal enhancement than the liver. Maximal contrast is achieved by subtracting the registered first image of the series from the last image. Subsequently, the liver is segmented based on the resulting "contrast" volume by means of a level set approach, which takes boundary as well as region information into consideration [16]. More implementation details can be found in [15].

The obtained mask coarsely segments the liver across the registered DCE series. Simultaneously, inverting the registration transformations and applying them to the liver mask yield liver segmentations in each original dynamic. Finally, we subtract from each deformation field the deformation field resulting from the registration of the first image to the last one. We do this merely for practical reasons, so that all deformation fields are relative to the first image in the series.

The liver's mean relative displacement in a dynamic volume with respect to the first image is estimated by the displacement of the liver mask's center of mass, see Fig. 4.1. The large displacements in some parts of the graph represent strong inhalation emanating from the breath holds (during dynamics 13-22, 33-42, 61-70 and 79-108). Notice that, at the same time, these large displacements coincide with abrupt offsets in the time intensity curves: see the arrows in Fig. 4.1(c).

In Section *Varying Applied Flip-angle Compensation* we will show how the liver displacements can be used to compensate for these intensity offsets.

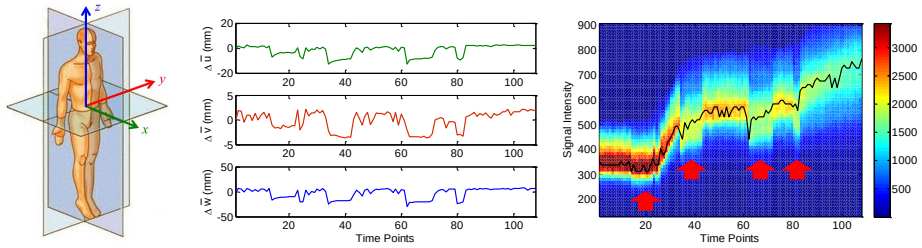

(a) (b) (c)

Figure 4.1: (a) Image coordinates; (b) Liver displacement curves in x, y and z directions; (c) The distribution of time intensity curves (TICs) for all liver voxels. The black line is the mode.

4.2.3. INPUT FUNCTION MODELS

An arterial input function (AIF) represents the time-dependent arterial contrast agent (CA) concentration, that is used in PK modeling of dynamic imaging data. The AIF is often computed directly from the signal measured in an artery close to the tissue of interest. The liver, however, has two inputs: the hepatic artery's AIF and the portal vein's venous input function (VIF).

We assume that the profile of both input functions follows a slightly modified input function model described by Orton *et al.* [17]. This model parametrizes an input function as a sum of two functions, one describing the first passage of the bolus peak, and the other describing the wash-out of CA in the tail of the input function [18].

The bolus peak $C_B(t)$ is described by:

$$C_B(t) = a_B \mu_B^2 e^{-\mu_B t} u(t), \tag{4.5}$$

with $u(t)$ the unit step function. This function has been modified slightly with respect to the one described by Orton *et al.*, such that the area under the curve of $C_B(t)$ is given by the parameter a_B, while μ_B only affects the decay rate.

The tail of the AIF and VIF is expressed as a convolution between the bolus peak and a body transfer function G(t), which is modeled as

$$G(t) = a_G e^{-\mu_G t} u(t), \tag{4.6}$$

in which a_G determines the starting level of this decay function and μ_G governs the decay rate, which may reflect kidney functioning.

Thus, the complete input function is given by:

$$\begin{aligned} C_I(t) &= C_B(t) + C_B(t) * G(t) \\ &= \left[A_B t e^{-\mu_B t} + A_G \left(e^{-\mu_G t} - e^{-\mu_B t} \right) \right] u(t), \end{aligned} \tag{4.7}$$

with

$$A_B = a_B \mu_B^2 \left(1 - \frac{a_G}{\mu_B - \mu_G} \right),$$

$$A_G = \frac{a_B a_G \mu_B^2}{(\mu_B - \mu_G)^2}.$$

which can be used to represent either the AIF or VIF.

The liver's AIF and VIF were estimated by semi-automatically segmenting a homogeneous region in the aorta and the portal vein, respectively [15]. Subsequently, the top three of most enhancing time intensity curves of the voxels in both regions were separately averaged and converted into time concentration curves (CTC) assuming a nonlinear relationship between signal intensity and concentration of contrast agent [19]. Finally, the input function parameters were estimated by fitting Orton's model to these data. These fits yield different parameters for AIF and VIF.

An advantage of our approach is that noise on the input function is suppressed, because a smooth, parameterized representation is fit to the data. However, not all features contained in the original data may be represented, especially a second pass of the bolus peak, which is not contained in Orton's model. We considered this limitation acceptable as, we could not visually identify a second peak corresponding to a second bolus pass in the hepatic artery let alone in the portal vein for any data set.

Furthermore, the parameterized input functions can be analytically integrated in our PKM (see below). As such, it allows for a continuous estimate of the time delay with which the AIF and VIF arrive in a voxel under investigation.

4.2.4. SOURBRON'S MODEL

Sourbron *et al.* [2] developed a dual-inlets, two-compartment uptake model that was especially designed for the intracellular hepatobiliary contrast agent Primovist. The diagram in Fig. 4.2 [2] illustrates the model. The arterial input function C_A and venous input function C_V are the dual inlets representing the contrast agent concentration in the blood plasma supplied to the liver by the hepatic artery and the portal vein, respectively. T_A and T_V represent time delays and F_A and F_V are arterial and venous plasma flows, respectively. Furthermore, in the gray rectangle denoting liver tissue, the left circle represents the extracellular compartment and the right circle stands for the intracellular compartment, i.e. corresponding to the hepatocytes. As such, V_E is the extracellular volume and K_I represents the uptake rate of the hepatocytes represented by a volume V_I.

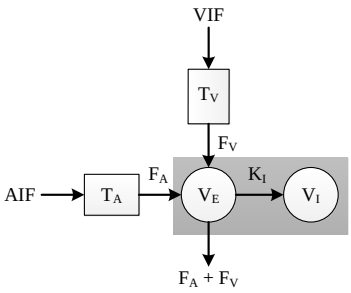

Figure 4.2: Sourbron model: a dual-inlets two-compartment uptake model for Gadoxetate disodium in the liver. The AIF and VIF are dual inlets into the liver, representing the concentration of the contrast agent over time entering from the hepatic artery and the portal vein. T_A and T_V are time delays. F_A and F_V are the arterial and venous plasma flows, respectively (in mL per minute per 100 mL). The gray rectangle represents the liver, the left circle denotes the extracellular compartment V_E (in mL per 100 mL) and the right circle stands for the hepatocytes, i.e. the intracellular compartment. K_I (per minute) is the liver uptake rate.

The analytical solution of Sourbron's model yielding the total contrast agent concentration C_T in a voxel is

$$\begin{aligned} C_T(t) = &\frac{K_I}{F_A+F_V+K_I}\int_0^t \left[F_A C_A(\tau-T_A)+F_V C_V(\tau-T_V)\right]d\tau \\ &+\frac{F_A+F_V}{F_A+F_V+K_I}e^{-\frac{t}{T_E}}\int_0^t e^{\frac{\tau}{T_E}}\left[F_A C_A(\tau-T_A)+F_V C_V(\tau-T_V)\right]d\tau, \end{aligned} \tag{4.8}$$

where

$$T_E = \frac{V_E}{F_A+F_V+K_I}.$$

A derivation of this expression can be found in Appendix I.

4.2.5. THE COMBINED ORTON-SOURBRON (COS) MODEL

Since vascular input functions are the front-ends of Sourbron's liver model, a comprehensive model can be derived by inserting Eq. 4.7 into Eq. 4.8. This leads for the contrast agent concentration in a voxel $C_{T,I}$ due to either AIF or VIF (i.e $I \in \{A, V\}$ to:

$$\begin{aligned} C_{T,I}(t) = F_I * u(t-T_I)\{ &\\ &+A_B\frac{\mu_B V_E - K_I}{\mu_B\left(F_A+F_V+K_I-\mu_B V_E\right)}(t-T_I)\,e^{-\mu_B(t-T_I)} \\ &-\left(\begin{array}{l} +A_B\dfrac{\left(\mu_B V_E-K_I\right)^2+(F_A+F_V)K_I}{\mu_B^2\left(F_A+F_V+K_I-\mu_B V_E\right)^2} \\ +A_G\dfrac{\mu_B V_E-K_I}{\mu_B\left(F_A+F_V+K_I-\mu_B V_E\right)} \end{array}\right)e^{-\mu_B(t-T_I)} \\ &+A_G\frac{\mu_G V_E-K_I}{\mu_G\left(F_A+F_V+K_I-\mu_G V_E\right)}e^{-\mu_G(t-T_I)} \end{aligned}$$

$$
\begin{aligned}
&+\frac{(F_A+F_V)\,V_E^2}{F_A+F_V+K_I}\left(\begin{array}{l}+\dfrac{A_B}{\left(F_A+F_V+K_I-\mu_B V_E\right)^2}\\ +\dfrac{A_G\left(\mu_B-\mu_G\right)}{\left(F_A+F_V+K_I-\mu_B V_E\right)\left(F_A+F_V+K_I-\mu_G V_E\right)}\end{array}\right)e^{-\frac{F_A+F_V+K_I}{V_E}(t-T_I)}\\
&+\frac{K_I}{F_A+F_V+K_I}\left(\frac{A_B}{\mu_B^2}-\frac{A_G}{\mu_B}+\frac{A_G}{\mu_G}\right)\\
&\},
\end{aligned}
\tag{4.9}
$$

in which Orton's model parameters (μ_B, μ_G) are particular for either AIF or VIF; T_I refers to the time delay associated with the particular input function. A derivation of this expression can be found in Appendix II.

The final model is expressed as the sum of contributions from AIF and VIF:

$$C_T(t) = C_{T,A}(t) + C_{T,V}(t), \tag{4.10}$$

in which C_T, as before, models the total contrast agent concentration in a voxel.

Practically, we set the time delay for the portal vein (T_V) to be zero (as in [2]) since it is smaller than the temporal resolution of our data (2.2 s). We do estimate the time delay of the arterial input function (T_A), which is larger as it is measured in the aorta, i.e. further away from the liver.

4.2.6. VARYING APPLIED FLIP-ANGLE COMPENSATION

Fig. 4.1 shows the distribution of TICs for a particular patient. Several abrupt drops in signal intensity may be observed that appear correlated with the liver's displacement.

We hypothesize that this signal variation can be modeled as a deviation in the locally applied flip-angle. In general, the signal intensity in a voxel emanating from a gradient echo sequence, neglecting T_2^* decay, and assuming the spins are in the steady state, is given by:

$$S(\alpha, T_1) = N(H)\sin(\alpha)\frac{1-e^{-\frac{TR}{T_1}}}{1-\cos(\alpha)\,e^{-\frac{TR}{T_1}}}, \tag{4.11}$$

where $N(H)$ is the local proton density, multiplied by an arbitrary factor (the scaling factor used by the scanner), T_1 the spin-lattice relaxation time, α the flip-angle and T_R the repetition time.

Furthermore, the Relative Signal Intensity (RSI) in a voxel while the contrast agent is flowing in can be expressed as:

$$RSI(\alpha, T_1) = \frac{S(\alpha, T_1)}{S(\alpha_0, T_{10})} = \frac{sin(\alpha)\,\frac{1-e^{-\frac{TR}{T_1}}}{1-\cos(\alpha)e^{-\frac{TR}{T_1}}}}{sin(\alpha_0)\,\frac{1-e^{-\frac{TR}{T_{10}}}}{1-\cos(\alpha_0)e^{-\frac{TR}{T_{10}}}}}, \tag{4.12}$$

in which α_0 is the presumed flip-angle in the voxel prior to contrast administration (we assume 15°, i.e. the scan protocol); T_{10} the spin-lattice relaxation time before contrast

arrives, T_1 the actual spin-lattice relaxation time and α the actually perceived flip-angle during the dynamic scan, which is assumed to be varying due to liver movement in the FOV.

The contrast agent concentration C_T can be expressed as a function of α, T_1 and the RSI as (see Appendix III):

$$C_T(\alpha, T_1) = \frac{1}{R}\left\{ -\frac{1}{TR}\ln\left(\frac{\frac{1-\cos(\alpha_0)e^{-\frac{TR}{T_{10}}}}{1-e^{-\frac{TR}{T_{10}}}} - RSI(\alpha, T_1)}{\frac{1-\cos(\alpha_0)e^{-\frac{TR}{T_{10}}}}{1-e^{-\frac{TR}{T_{10}}}} - RSI(\alpha, T_1)\cos(\alpha_0)} \right) - \frac{1}{T_{10}} \right\}, \tag{4.13}$$

with R the relaxivity of the applied contrast agent (for Gd-EOB-DTPA at 3T, R = 7 $s^{-1}mM^{-1}l$ [20]).

Consequently, the error in the calculated contrast agent concentration due to deviating flip-angle (e.g. caused by B_1-inhomogeneity) is:

$$\Delta C_T(\alpha, T_1) = C_T(\alpha, T_1) - C_T(\alpha_0, T_1). \tag{4.14}$$

The intrinsic T_1 value of the liver prior to contrast injection is around 800 ms [21], while we estimate that the effective T_1 can be as small as 300 ms after contrast injection. Fig. 4.3(a) shows ΔC_T for this range of T_1 values as well as for flip angle deviations varying from -3° to +3°. Essentially, the graph demonstrates that the error in C_T is non-linearly dependent on T_1 for any given deviation in flip-angle. However, normalizing through division by RSI(α, T_1) yields profiles that are independent of T_1 for every flip-angle deviation, see Fig. 4.3(b). Furthermore, the distance between the profiles reflects that there is an approximately linear relation between ΔC_T and the applied flip-angle.

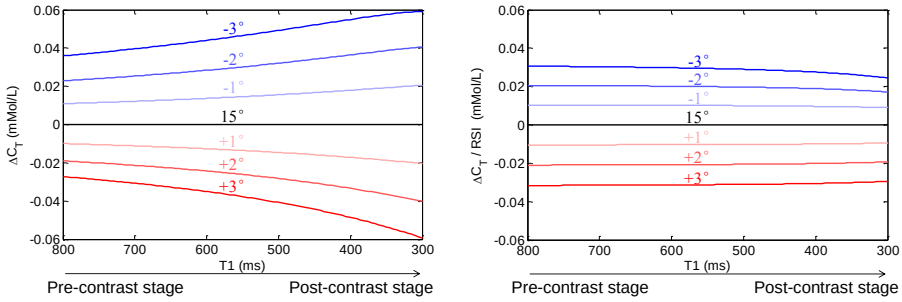

Figure 4.3: (a) Error in the contrast agent concentration due to a deviation in flip-angle (e.g. due to B_1 inhomogeneity) as a function of T_1 value; (b) Error in contrast agent concentration after normalization by the relative signal intensity.

Assuming that there is a linear relation between the displacement of the liver and the change of flip-angle, we model the contrast agent concentration in a voxel as:

$$C_T'(t) = C_T(t) + \begin{bmatrix} \alpha RSI(t) & \beta RSI(t) & \gamma RSI(t) \end{bmatrix} \begin{bmatrix} \Delta u(t) & \Delta v(t) & \Delta w(t) \end{bmatrix}^T, \tag{4.15}$$

in which $C'_T(t)$ is the measured, uncorrected contrast agent concentration in a voxel; $C_T(t)$ is the combined Orton-Sourbron (COS) model, see Eq. 4.10; α, β and γ are proportionality constants that need to be estimated and RSI(t) is the relative signal intensity with respect to the one in the pre-contrast stage, i.e. $S(\alpha, T_{1-post})/S(\alpha, T_{1-pre})$.

Thus, by fitting Eq. 4.15 to the concentration curves we have not only parameterized the arrival time in Sourbron's model (through the COS approach), but also included an implicit varying flip-angle correction (FLAC). Henceforth, we will refer to this as our COS-FLAC approach.

4.2.7. EXPERIMENTAL SETUP

COMPARISON BETWEEN SOURBRON'S MODEL AND THE COS MODEL

We first ran a numerical experiment to compare the accuracy and time efficiency of Sourbron's original approach and the proposed COS technique.

Therefore, the liver's AIF and VIF were obtained in each of our 11 patient both numerically and estimated as described above by fitting Orton's model. After that, Sourbron's model as well as our COS model were applied to extract the PK model parameters in each liver voxel.

Subsequently, both the numerical and analytical AIFs and VIFs were adopted as ground truth. Furthermore, the PKM parameters from the Sourbron and COS models were averaged to yield true model parameters for each voxel, from which noise-free tissue concentration curves were generated via Eq. 4.8. Thereafter, synthetic AIFs and VIFs were generated by adding noise to ground-truth AIFs and VIFs of each patient. The standard deviation of this added noise was equal to the root mean square of the residuals of Orton's model fit (performed separately for AIF and VIF). In the same way, noisy tissue concentration curves were generated by adding noise to the ground truth tissue curves. Finally, we fitted both PK models to the noisy synthetic data and compared the estimated PK model parameters with the ground truth. The nonlinear least-squares fitting routine *lsqcurvefit* in MATLAB (version R2015b; Mathworks, Natick, USA) was used to perform the model fits; 19 cores were adopted for parallel computing on a HPC equipped with two Intel(R) Xeon(R) CPU E5-2698 v4 clocked at 2.20GHz and 256GB RAM memory.

RELATION BETWEEN DISPLACEMENT AND PROGRAMMED FLIP-ANGLE DEVIATIONS

Eq. 4.15 assumed that a difference from the true contrast agent is linearly related to the displacement of a liver voxel. Furthermore, the difference (ΔC_T) was modeled to linearly relate to the deviation from the programmed flip-angle (Fig. 4.3).

To assess the validity of this, the zeta-map from the DREAM sequence, representing the deviation from the programmed flip angle, was geometrically aligned to the first dynamic. Observe that the displacement of a liver voxel in any DCE image is given by the registration transformation that is relative to the first dynamic. Subsequently, the difference in zeta value over the displacement vector (Δzeta) was correlated to the displacement across all dynamics. The strength of the correlation was assessed by Pearson's correlation coefficient and the significance of the correlation was determined.

THE COS-FLAC MODEL WITH AND WITHOUT RSI WEIGHTING

Models of increasing complexity, from the COS-model up to the COS-FLAC model with RSI weighting, were fit to the data of the 11 subjects described 4.2. The root mean square

error (RMSE) of the residue that remains after fitting the COS and the COS-FLAC models to the signal were determined in order to quantitatively assess the performance. However, increasing degrees of freedom by adding parameters to a model generally leads to decreased smaller RMSE of the fit residue. To evaluate whether the added parameters truly contributed to a better fit, three model-selection criteria were applied: Akaike's information criterion (AIC) [22], the Bayesian information criterion (BIC) [23], and Information Complexity (ICOMP) [24].

4.3. RESULTS

4.3.1. COMPARISON BETWEEN SOURBRON'S MODEL AND THE COS MODEL

TABLE 4.1 shows absolute values of the fitted model parameters for Sourbron's model, the COS model and the ground truth. Furthermore, Table 4.2 show the mean difference between the ground truth and estimated PK model parameters (as well as corresponding standard deviations) for Sourbron's model and the COS model. It shows that the COS model achieved smaller mean difference and standard deviation on four PK model parameters out of five. Additionally, the COS model was fitted more than 7 times faster than Sourbron's model due to the analytical representation of AIF and VIF.

Table 4.1: Comparison between Sourbron's model (discrete AIF) and COS model (analytical AIF) in terms of estimating PK model parameters on synthetic data. The numbers report the mean values of fitted model parameters and corresponding standard deviation (between brackets).

	Original Sourbron's model	COS model	Ground truth
F_A (ml / min / 100ml)	15.658 (12.363)	13.124 (12.743)	13.287 (12.285)
F_V (ml / min / 100ml)	38.660 (27.696)	72.402 (58.868)	56.855 (45.519)
K_I (/ 100 / min)	8.161 (5.003)	8.078 (4.318)	7.656 (4.026)
V_E (ml / 100 ml)	0.452 (0.236)	0.407 (0.190)	0.429 (0.214)
T_A (sec)	5.941 (2.902)	5.417 (3.449)	5.634 (3.166)

Table 4.2: Comparison between Sourbron's model (discrete AIF) and COS model (analytical AIF) in terms of estimating PK model parameters and time efficiency on synthetic data. The numbers report the mean difference from the ground truth and corresponding standard deviation (between brackets). The numbers printed in boldface are the best outcomes per row.

	Original Sourbron's model	COS model
ΔF_A (ml / min / 100ml)	2.058 (3.983)	**-0.096** (**2.297**)
ΔF_V (ml / min / 100ml)	-17.318 (29.495)	**6.965** (**23.260**)
ΔK_I (/ 100 / min)	0.407 (1.407)	**0.339** (**0.704**)
ΔV_E (ml / 100 ml)	**0.005** (0.047)	-0.011 (**0.038**)
ΔT_A (sec)	0.172 (1.409)	**0.073** (**1.330**)
Computation time (min)	145.855	19.455

4.3.2. RELATION BETWEEN DISPLACEMENT AND PROGRAMMED FLIP-ANGLE DEVIATIONS

Table 4.3 collates the mean correlation coefficients averaged over all liver voxels for each patient. Additionally, the mean p-values (and associated standard deviations) of the correlations are given. The mean p-values demonstrate that the correlations are highly significant. Furthermore, the correlation coefficients indicated a moderate to strong linear relationship [26]. This supports the validity of the assumed linear relation between displacement and deviation in flip angle.

Table 4.3: Mean Pearson correlation coefficients (and associated standard deviation) of the correlations between the displacement and the deviation from the applied flip-angle over all liver voxels as well as the mean p-values (and standard deviation) of these correlations stratified by patient number.

Case	Correlation coefficients	P-values
1	0.742 (0.220)	7.71E-10 (5.06E-09)
2	0.554 (0.260)	1.61E-05 (7.21E-05)
3	0.675 (0.271)	1.29E-07 (7.24E-07)
4	0.536 (0.277)	1.81E-04 (7.13E-04)
5	0.621 (0.272)	1.86E-06 (9.15E-06)
6	0.677 (0.190)	9.47E-11 (5.02E-10)
7	0.851 (0.169)	3.48E-08 (1.99E-07)
8	0.798 (0.197)	1.41E-09 (8.50E-09)
9	0.542 (0.263)	4.52E-05 (1.86E-04)
10	0.732 (0.226)	7.82E-10 (4.64E-09)
11	0.840 (0.142)	2.80E-12 (1.99E-11)
Overall	0.655 (0.275)	7.86E-07 (4.10E-06)

4.3.3. THE COS-FLAC MODEL WITH AND WITHOUT RSI WEIGHTING

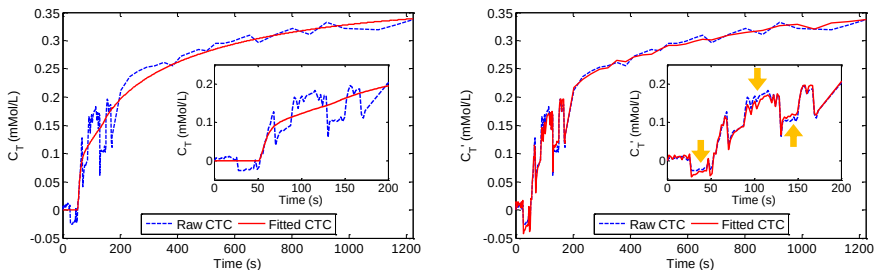

(a) (b)

The signal intensity in the liver of one patient was already shown in Fig. 4.1(c). Fig. 4.4 illustrates how models (red) of increasing complexity, from COS up to the COS-FLAC model with RSI weighting, fit to the concentration curve (blue) from an exemplary voxel. Insets show zoom-ins of the initial part of the graphs, containing most of the breath holds. In Fig. 4.4(a) merely the combined Orton-Sourbron (COS) model was fitted. The model does not fit to the strong fluctuations of the first part of the concentration curve. In Fig.

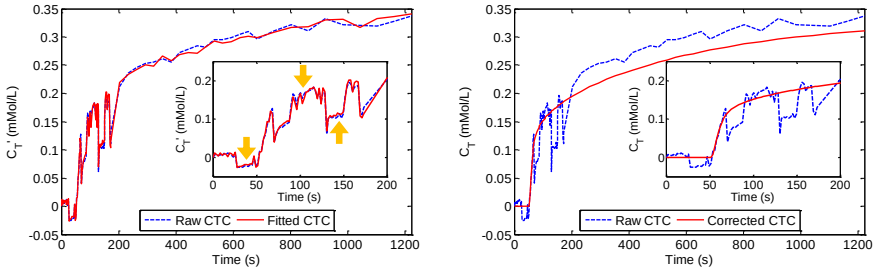

(c) (d)

Figure 4.4: Fitting results (red) of different models to the concentration-time curve ($C'_T(t)$, blue) extracted from a single voxel. (a) Combined Orton-Sourbron (COS) model; (b) COS model with varying flip-angle correction (FLAC) but without the RSI weighting term in Eq. 4.15; (c) COS-FLAC model including the RSI weighting term; (d) Pure concentration-time curve ($C_T(t)$) recovered from (c). All sub-plots show zoom-ins of the initial part of the curves, i.e. 0 – 200 s.

4

4.4(a), we fitted the COS model with varying flip-angle correction (FLAC) model but without the RSI weighting term. Clearly, an improved fitting result was achieved compared with Fig 4 (a). However, some parts of the concentration curve are slightly off, see the yellow arrows in Fig. 4.4(b). Fig. 4.4(c) shows that the full COS-FLAC model including the RSI weighting term achieved an even better fit. For reference, Fig. 4.4(c) shows the mere concentration part C_T from Eq. 4.15 taken from the fit in Fig. 4.4(c).

Table 4.4: Average root mean square error (RMSE) of the residue that remains after fitting the COS and COS-FLAC models with and without RSI weighting term. The numbers are the mean value and the standard deviation (std) averaged over all liver voxels. The best results are printed in boldface.

Case	COS	COS-FLAC without RSI weighting	COS-FLAC with RSI weighting
1	1.902E-02 (4.334E-03)	1.496E-02 (**3.652E-03**)	**1.461E-02** (3.678E-03)
2	1.600E-02 (5.355E-03)	1.160E-02 (3.100E-03)	**1.129E-02** (**3.089E-03**)
3	2.664E-02 (1.117E-02)	2.054E-02 (7.739E-03)	**2.012E-02** (**7.579E-03**)
4	4.260E-02 (1.740E-02)	3.523E-02 (1.441E-02)	**3.491E-02** (**1.441E-02**)
5	2.206E-02 (5.618E-03)	1.952E-02 (4.966E-03)	**1.929E-02** (**4.927E-03**)
6	2.975E-02 (1.176E-02)	2.059E-02 (6.565E-03)	**1.948E-02** (**5.886E-03**)
7	2.192E-02 (9.294E-03)	1.111E-02 (**3.280E-03**)	**1.067E-02** (3.325E-03)
8	2.500E-02 (9.045E-03)	1.890E-02 (6.708E-03)	**1.826E-02** (**6.708E-03**)
9	1.688E-02 (4.040E-03)	1.411E-02 (**3.953E-03**)	**1.406E-02** (3.984E-03)
10	2.338E-02 (5.071E-03)	2.033E-02 (4.746E-03)	**2.005E-02** (**4.728E-03**)
11	3.243E-02 (9.060E-03)	1.916E-02 (5.164E-03)	**1.802E-02** (**5.152E-03**)
Overall	2.515E-02 (1.047E-02)	1.868E-02 (7.446E-03)	**1.819E-02** (**7.319E-03**)

The mean RMSEs of fitting in all 11 patients is collated in Table 4.4. It shows that the COS-FLAC model with RSI weighting term achieved the lowest RMSE, which is significantly better than the COS model and the COS-FLAC model without RSI weighting term (p <0.001, assessed by paired t-tests). Henceforth the, COS-FLAC model refers to the model including the RSI weighting term.

Table 4.5 shows the scores that PK models get according to three model selection cri-

Table 4.5: The scores that each model gets as well as the percentage of the voxels in the liver of 11 subjects in which the COS-FLAC model outperformed the COS approach according to three model-selection criteria: Akaike's Information criterion (AIC), Bayesian Information Criterion (BIC) and Information Complexity (ICOMP). A lower score indicates the model fits the data better.

Case	AIC			BIC			ICOMP		
	COS	COS-FLAC	Outperform percentage (%)	COS	COS-FLAC	Outperform percentage (%)	COS	COS-FLAC	Outperform percentage (%)
1	-852.679 (**51.460**)	**-908.107** (57.626)	98.615	-839.268 (**51.460**)	**-886.650** (57.626)	93.292	-853.657 (**51.386**)	**-911.632** (57.138)	99.716
2	-893.338 (78.885)	**-963.347** (**62.107**)	97.817	-879.927 (78.885)	**-941.890** (**62.107**)	90.685	-894.220 (79.409)	**-968.002** (**62.020**)	99.388
3	-776.654 (103.998)	**-833.659** (**92.809**)	98.159	-763.243 (103.998)	**-812.201** (**92.809**)	91.089	-780.678 (104.698)	**-841.156** (**93.754**)	99.499
4	-673.668 (**94.404**)	**-712.605** (94.814)	95.422	-660.351 (**94.404**)	**-691.297** (94.814)	82.586	-674.465 (94.602)	**-717.599** (**93.913**)	98.769
5	-820.607 (58.029)	**-848.015** (**57.665**)	94.591	-807.197 (58.029)	**-826.558** (**57.665**)	79.425	-820.605 (58.159)	**-851.622** (**57.673**)	98.952
6	-767.001 (91.726)	**-848.749** (**68.966**)	98.667	-753.591 (91.726)	**-827.292** (**68.966**)	94.646	-767.590 (92.134)	**-853.252** (**68.769**)	99.558
7	-833.484 (98.759)	**-975.161** (**71.903**)	99.371	-820.073 (98.759)	**-953.704** (**71.903**)	97.271	-833.528 (98.651)	**-977.555** (**71.784**)	99.695
8	-795.408 (**83.835**)	**-860.269** (84.557)	97.925	-781.997 (**83.835**)	**-838.812** (84.557)	91.634	-794.805 (**83.843**)	**-861.989** (84.349)	99.047
9	-878.362 (**54.731**)	**-917.277** (64.419)	97.159	-864.951 (**54.731**)	**-895.820** (64.419)	88.554	-879.493 (**55.079**)	**-922.729** (64.564)	99.458
10	-808.133 (**48.258**)	**-840.045** (53.112)	96.209	-794.722 (**48.258**)	**-818.588** (53.112)	84.253	-809.190 (**48.543**)	**-844.428** (53.273)	98.985
11	-738.370 (67.289)	**-863.216** (**66.717**)	99.083	-724.959 (67.289)	**-841.759** (**66.717**)	96.129	-736.598 (67.654)	**-868.164** (**66.278**)	99.616
Overall	-794.126 (101.212)	**-860.240** (**100.905**)	97.397	-780.728 (101.198)	**-838.802** (**100.882**)	89.380	-794.990 (101.466)	**-864.651** (**100.638**)	99.300

teria as well as the percentage of voxels in which these criteria favored the COS-FLAC model over the mere COS approach. The proposed COS-FLAC technique was considered to yield a better fit in the majority of voxels across all subjects according to all three model-selection methods (p <0.001, assessed by paired t-tests).

4.4. DISCUSSION

IN this paper, we proposed an improved pharmacokinetic model for DCE-MRI of the liver. The novelties of our work comprise: (1) analytically modeling the arrival-time of the contrast agent in a voxel; (2) compensation for effects that allowing for a breath-dependent B_1-induced variation of the experienced flip-angle in each voxel.

Orton's model was adopted to represent the liver's input functions (hepatic artery and portal vein) and embed them into Sourbron's model. The combined Orton and Sourborn (COS) model was shown to enhance the fitting accuracy as well as the efficiency of the model fitting (see Table 4.2). The poorer performance of Sourbron's original approach is due to the discretized delay of the arterial input and determining the best model fit over a set of delay values.

A potentially deviating flip-angle was modeled to linearly relate to the displacement of a liver voxel with respect to the first image. We referred to the approach combining both novelties as the COS-FLAC model. The validity of our approach is supported by the moderate to strong linear correlation between displacement and deviation in flip angle.

The COS-FLAC model was quantitatively assessed by the root mean square error (RMSE) of the residue that remains after fitting the model to the signal in every voxel of the liver. We found that the COS-FLAC model achieved significantly lower RMSE than the COS approach. Furthermore, three model complexity criteria showed that the COS-FLAC model outperformed the COS model in the vast majority of voxels. These findings confirm that a small degree of B_1-inhomogeneity can have a marked effect on the estimation of PKM parameters, c.f. [10][11].

One might argue that the COS approach would suffice in voxels in which there is no deviation in flip-angle. This might explain why, according to the model selection criteria, there are still some voxels in which this simpler model appears sufficient. At the same time, the large number of voxels in which the COS-FLAC approach is favored, emphasizes to our opinion its importance.

There are several limitations of our work. A first limitation is that the number of subjects is rather small. Clearly, evaluating the performance of the method on a larger number of subjects would be more convincing. Unfortunately, we are restricted to a small number of subjects as our work is part of a pilot study into the uptake rate of the contrast medium into liver cells.

A second limitation is the lack of a reference standard. Obtaining the true pharmacokinetic tissue parameters under realistic measurement circumstances is a highly complex, still unsolved issue.

4.5. CONCLUSION

Our work primarily targeted to improve pharmacokinetic modeling for DCE-MRI of the liver. However, other types of pharmacokinetic models may also benefit from our ap-

proaches, since the techniques are generally applicable.

APPENDIX 1: DERIVATION OF SOURBRON'S MODEL

Sourbron's model:

$$\begin{cases} V_E \dfrac{dC_E(t)}{dt} = F_A C_A(t-T_A) + F_V C_V(t-T_V) - (F_A + F_V + K_I) C_E(t) \\ V_I \dfrac{dC_I(t)}{dt} = K_I C_E(t) \\ C_T(t) = V_E C_E(t) + V_I C_I(t) \end{cases}, \tag{4.16}$$

where
F_A: Arterial plasma flow (mL/min/100 mL)
F_V: Venous plasma flow (mL/min/100 mL)
T_A: Arterial delay (sec)
T_V: Venous delay (sec)
K_I: Uptake rate (per min)
V_E: Extracellular volume (mL/100 mL)
V_I: Hepatocyte volume (mL/100 mL)
T_E: Extracellular mean transit time (sec)

The first equation in Sourbron's model

$$V_E \frac{dC_E(t)}{dt} = F_A C_A(t-T_A) + F_V C_V(t-T_V) - (F_A + F_V + K_I) C_E(t). \tag{4.17}$$

According to

$$T_E = \frac{V_E}{F_A + F_V + K_I}, \tag{4.18}$$

Eq. 4.17 can be rearranged as

$$\frac{dV_E C_E(t)}{dt} = F_A C_A(t-T_A) + F_V C_V(t-T_V) - \frac{V_E C_E(t)}{T_E}. \tag{4.19}$$

The equation is of the type

$$\frac{dy(t)}{dt} + k(t)\, y(t) = Q(t), \tag{4.20}$$

whose general solution is

$$\begin{cases} y(t) = y(a)\, e^{-A(t)} + e^{-A(t)} \displaystyle\int_0^t Q(u)\, e^{-A(u)}\, du \\ A(t) = \displaystyle\int_0^t k(u)\, du \end{cases}, \tag{4.21}$$

where a is arbitrary. In our case, $a = 0$, $y(a) = y(0) = 0$.

Substitution of

$$\begin{cases} y(t) = V_E C_E(t) \\ k(t) = \dfrac{1}{T_E} \\ Q(t) = F_A C_A(t-T_A) + F_V C_V(t-T_V) \end{cases}, \tag{4.22}$$

into Eq. 4.21 leads to

$$C_E(t) = \frac{1}{V_E} e^{-\frac{t}{T_E}} \int_0^t Q(u)\, e^{\frac{u}{T_E}}\, du. \tag{4.23}$$

Now consider the third equation in Sourbron's model

$$C_T(t) = V_E C_E(t) + V_I C_I(t). \tag{4.24}$$

Obtaining the derivatives of both sides

$$\frac{dC_T(t)}{dt} = V_E \frac{dC_E(t)}{dt} + V_I \frac{dC_I(t)}{dt}. \tag{4.25}$$

Substituting the first and second equations of Sourbron's model

$$\begin{aligned} \frac{dC_T(t)}{dt} =& F_A C_A(t - T_A) + F_V C_V(t - T_V) - (F_A + F_V + K_I) C_E(t) + K_I C_E(t) \\ =& Q(t) - (F_A + F_V) C_E(t). \end{aligned} \tag{4.26}$$

The solution is

$$C_T(t) = \int_0^t [Q(t) - (F_A + F_V) C_E(t)]\, dt. \tag{4.27}$$

Substituting Eq. 4.18 and Eq. 4.23 into Eq. 4.27

$$\begin{aligned} C_T(t) &= \int_0^t \left[Q(t) - \frac{F_A + F_V}{V_E} e^{-\frac{t}{T_E}} \int_0^t Q(u)\, e^{\frac{u}{T_E}}\, du \right] dt \\ &= \int_0^t \left[Q(t) - \frac{F_A + F_V}{F_A + F_V + K_I} \frac{1}{T_E} e^{-\frac{t}{T_E}} \int_0^t Q(u)\, e^{\frac{u}{T_E}}\, du \right] dt \\ &= \int_0^t Q(t)\, dt - \frac{F_A + F_V}{F_A + F_V + K_I} \frac{1}{T_E} \int_0^t e^{-\frac{t}{T_E}} \left(\int_0^t Q(u)\, e^{\frac{u}{T_E}}\, du \right) dt \\ &= \int_0^t Q(t)\, dt + \frac{F_A + F_V}{F_A + F_V + K_I} \int_0^t \left(\int_0^t Q(u)\, e^{\frac{u}{T_E}}\, du \right) de^{-\frac{t}{T_E}} \\ &= \int_0^t Q(t)\, dt + \frac{F_A + F_V}{F_A + F_V + K_I} \left\{ \begin{array}{l} \left[\left(\int_0^t Q(u)\, e^{\frac{u}{T_E}}\, du \right) e^{-\frac{t}{T_E}} \right] \Big|_0^t \\ -\int_0^t e^{-\frac{t}{T_E}}\, d\left(\int_0^t Q(u)\, e^{\frac{u}{T_E}}\, du \right) \end{array} \right\} \\ &= \int_0^t Q(t)\, dt + \frac{F_A + F_V}{F_A + F_V + K_I} \left[\begin{array}{l} \left(\int_0^t Q(u)\, e^{\frac{u}{T_E}}\, du \right) e^{-\frac{t}{T_E}} \\ -\int_0^t e^{-\frac{t}{T_E}} Q(t)\, e^{\frac{t}{T_E}}\, dt \end{array} \right] \\ &= \int_0^t Q(t)\, dt + \frac{F_A + F_V}{F_A + F_V + K_I} \left(e^{-\frac{t}{T_E}} \int_0^t Q(u)\, e^{\frac{u}{T_E}}\, du - \int_0^t Q(t)\, dt \right) \\ &= \frac{K_I}{F_A + F_V + K_I} \int_0^t Q(t)\, dt + \frac{F_A + F_V}{F_A + F_V + K_I} e^{-\frac{t}{T_E}} \int_0^t Q(u)\, e^{\frac{u}{T_E}}\, du, \end{aligned} \tag{4.28}$$

where

$$Q(t) = F_A C_A(t - T_A) + F_V C_V(t - T_V).$$

APPENDIX 2: DERIVATION OF COMBINED ORTON-SOURBRON MODEL

The AIF is described as:

$$\begin{aligned} C_{Orton}(t) &= C_B(t) + C_B(t) * G(t) \\ &= \left[A_B t e^{-\mu_B t} + A_G\left(e^{-\mu_G t} - e^{-\mu_B t}\right)\right] u(t), \end{aligned} \tag{4.29}$$

where

$$\begin{cases} A_B = a_B \mu_B^2 \left(1 - \dfrac{a_G}{\mu_B - \mu_G}\right) \\ A_G = \dfrac{a_B a_G \mu_B^2}{(\mu_B - \mu_G)^2} \end{cases}.$$

The solution of Sourbron's model is

$$\begin{aligned} C_T = &\frac{K_I}{F_A + F_V + K_I} \int_0^t \left[F_A C_A(\tau - T_A) + F_V C_V(\tau - T_V)\right] d\tau \\ &+ \frac{F_A + F_V}{F_A + F_V + K_I} e^{-\frac{t}{T_E}} \int_0^t e^{\frac{\tau}{T_E}} \left[F_A C_A(\tau - T_A) + F_V C_V(\tau - T_V)\right] d\tau. \end{aligned} \tag{4.30}$$

Mainly there are two kinds of integrals inside

$$\begin{cases} A(t) = \displaystyle\int_0^t F_I C_I(\tau - T_I)\, d\tau \\ B(t) = \displaystyle\int_0^t e^{\frac{\tau}{T_E}} F_I C_I(\tau - T_I)\, d\tau \end{cases}, \tag{4.31}$$

where I denotes either AIF (C_A) and VIF (C_V). Now A and B:

$$\begin{aligned} A(t) &= \int_0^t F_I C_I(\tau - T_I)\, d\tau \\ &= \int_0^{t - T_0} F_I C_I(\tau)\, d\tau \\ &= F_I \int_0^{t - T_0} \left[A_B t e^{-\mu_B \tau} + A_G\left(e^{-\mu_G \tau} - e^{-\mu_B \tau}\right)\right] d\tau \\ &= F_I \begin{bmatrix} -\dfrac{A_B}{\mu_B}(t - T_0)\, e^{-\mu_B (t - T_I)} + \left(\dfrac{A_G}{\mu_B} - \dfrac{A_B}{\mu_B^2}\right) e^{-\mu_B (t - T_I)} \\ -\dfrac{A_G}{\mu_G} e^{-\mu_G (t - T_I)} + \dfrac{A_B}{\mu_B^2} - \dfrac{A_G}{\mu_B} + \dfrac{A_G}{\mu_G} \end{bmatrix}. \end{aligned} \tag{4.32}$$

$$\begin{aligned} B(t) &= \int_0^t e^{\frac{\tau}{T_E}} F_I C_I(\tau - T_I)\, d\tau \\ &= F_I \int_0^t \left\{e^{\frac{\tau}{T_E}} \left[A_B t e^{-\mu_B(\tau - T_I)} + A_G\left(e^{-\mu_G(\tau - T_I)} - e^{-\mu_B(\tau - T_I)}\right)\right]\right\} d\tau. \end{aligned}$$

$$
\begin{aligned}
&= F_I \left[\begin{array}{l}
\dfrac{A_B T_E}{1-\mu_B T_E}(t-T_0)\, e^{\frac{1}{T_E}-\mu_B (t-T_I)} - \dfrac{A_B T_E^2}{(1-\mu_B T_E)^2} e^{\frac{t}{T_E}-\mu_B (t-T_I)} \\
-\dfrac{A_G T_E}{1-\mu_B T_E} e^{\frac{t}{T_E}-\mu_B (t-T_I)} + \dfrac{A_G T_E}{1-\mu_G T_E} e^{\frac{1}{T_E}-\mu_G (t-T_I)} \\
+\dfrac{A_G T_E e^{\frac{T_I}{T_E}}}{1-\mu_B T_E} - \dfrac{A_G T_E e^{\frac{T_I}{T_E}}}{1-\mu_G T_E} + \dfrac{A_B T_E^2 e^{\frac{T_I}{T_E}}}{(1-\mu_B T_E)^2}
\end{array} \right] \\
&= F_I \left[\begin{array}{l}
+\dfrac{A_B T_E}{1-\mu_B T_E}(t-T_0)\, e^{\frac{t}{T_E}-\mu_B (t-T_I)} \\
-\dfrac{T_E}{1-\mu_B T_E}\left(\dfrac{A_B T_E}{1-\mu_B T_E} + A_G\right) e^{\frac{t}{T_E}-\mu_B (t-T_I)} + \dfrac{A_G T_E}{1-\mu_G T_E} e^{\frac{t}{T_E}-\mu_G (t-T_I)} \\
+T_E \left(\dfrac{A_G}{1-\mu_B T_E} - \dfrac{A_G}{1-\mu_G T_E} + \dfrac{A_B T_E}{(1-\mu_B T_E)^2}\right) e^{\frac{T_I}{T_E}}
\end{array} \right].
\end{aligned} \tag{4.33}
$$

Substituting Eq. 4.32 and Eq. 4.33 into Eq. 4.30 we can obtain

$$
\begin{aligned}
C_T &= \frac{K_I}{F_A+F_V+K_I}\int_0^t \left[F_A C_A(\tau-T_A)+F_V C_V(\tau-T_V)\right] d\tau \\
&\quad + \frac{F_A+F_V}{F_A+F_V+K_I} e^{-\frac{t}{T_E}} \int_0^t e^{\frac{\tau}{T_E}} \left[F_A C_A(\tau-T_A)+F_V C_V(\tau-T_V)\right] d\tau \\
&= \frac{K_I}{F_A+F_V+K_I} \sum_{I=A,V} F_I \left[\begin{array}{l}
-\dfrac{A_B}{\mu_B}(t-T_0)\, e^{-\mu_B (t-T_I)} + \left(\dfrac{A_G}{\mu_B} - \dfrac{A_B}{\mu_B^2}\right) e^{-\mu_B (t-T_I)} \\
-\dfrac{A_G}{\mu_G} e^{-\mu_G (t-T_I)} + \dfrac{A_B}{\mu_B^2} - \dfrac{A_G}{\mu_B} + \dfrac{A_G}{\mu_G}
\end{array} \right]_I \\
&\quad + \frac{F_A+F_V}{F_A+F_V+K_I} e^{-\frac{t}{T_E}} \sum_{I=A,V} F_I \left[\begin{array}{l}
+\dfrac{A_B T_E}{1-\mu_B T_E}(t-T_0)\, e^{\frac{t}{T_E}-\mu_B (t-T_I)} \\
-\dfrac{T_E}{1-\mu_B T_E}\left(\dfrac{A_B T_E}{1-\mu_B T_E} + A_G\right) e^{\frac{t}{T_E}-\mu_B (t-T_I)} \\
+\dfrac{A_G T_E}{1-\mu_G T_E} e^{\frac{t}{T_E}-\mu_G (t-T_I)} \\
+T_E \left(\dfrac{A_G}{1-\mu_B T_E} - \dfrac{A_G}{1-\mu_G T_E} + \dfrac{A_B T_E}{(1-\mu_B T_E)^2}\right) e^{\frac{T_I}{T_E}}
\end{array} \right]_I \\
&= \frac{K_I}{F_A+F_V+K_I} \sum_{I=A,V} F_I \left[\begin{array}{l}
-\dfrac{A_B}{\mu_B}(t-T_0)\, e^{-\mu_B (t-T_I)} + \left(\dfrac{A_G}{\mu_B} - \dfrac{A_B}{\mu_B^2}\right) e^{-\mu_B (t-T_I)} \\
-\dfrac{A_G}{\mu_G} e^{-\mu_G (t-T_I)} + \dfrac{A_B}{\mu_B^2} - \dfrac{A_G}{\mu_B} + \dfrac{A_G}{\mu_G}
\end{array} \right]_I
\end{aligned}
$$

$$+\frac{F_A+F_V}{F_A+F_V+K_I}\sum_{I=A,V}F_I\left[\begin{array}{l}+\dfrac{A_BT_E}{1-\mu_BT_E}(t-T_I)\,e^{-\mu_B(t-T_I)}\\-\dfrac{T_E}{1-\mu_BT_E}\left(\dfrac{A_BT_E}{1-\mu_BT_E}+A_G\right)e^{-\mu_B(t-T_I)}\\+\dfrac{A_GT_E}{1-\mu_GT_E}e^{-\mu_G(t-T_I)}\\+T_E\left(\dfrac{A_G}{1-\mu_BT_E}-\dfrac{A_G}{1-\mu_GT_E}+\dfrac{A_BT_E}{(1-\mu_BT_E)^2}\right)e^{-\frac{t-T_I}{T_E}}\end{array}\right]_I$$

$$=\sum_{I=A,V}F_I\left[\begin{array}{l}+\left[-\dfrac{K_I}{F_A+F_V+K_I}\dfrac{A_B}{\mu_B}+\dfrac{F_A+F_V}{F_A+F_V+K_I}\dfrac{A_BT_E}{1-\mu_BT_E}\right](t-T_I)\,e^{-\mu_B(t-T_I)}\\+\left[\begin{array}{l}\dfrac{K_I}{F_A+F_V+K_I}\left(\dfrac{A_G}{\mu_B}-\dfrac{A_B}{\mu_B^2}\right)\\-\dfrac{F_A+F_V}{F_A+F_V+K_I}\dfrac{T_E}{1-\mu_BT_E}\left(\dfrac{A_BT_E}{1-\mu_BT_E}+A_G\right)\end{array}\right]e^{-\mu_B(t-T_I)}\\+\left[-\dfrac{K_I}{F_A+F_V+K_I}\dfrac{A_G}{\mu_G}+\dfrac{F_A+F_V}{F_A+F_V+K_I}\dfrac{A_GT_E}{1-\mu_GT_E}\right]e^{-\mu_G(t-T_I)}\\+\dfrac{K_I}{F_A+F_V+K_I}\left(\dfrac{A_B}{\mu_B^2}-\dfrac{A_G}{\mu_B}+\dfrac{A_G}{\mu_G}\right)\\+\dfrac{F_A+F_V}{F_A+F_V+K_I}T_E\left(\dfrac{A_G}{1-\mu_BT_E}-\dfrac{A_G}{1-\mu_GT_E}+\dfrac{A_BT_E}{(1-\mu_BT_E)^2}\right)e^{-\frac{t-T_I}{T_E}}\end{array}\right]_I$$

$$=\sum_{I=A,V}F_I\left[\begin{array}{l}+\left[-\dfrac{K_I}{F_A+F_V+K_I}\dfrac{A_B}{\mu_B}+\dfrac{F_A+F_V}{F_A+F_V+K_I}\dfrac{A_B}{1/T_E-\mu_B}\right](t-T_I)\,e^{-\mu_B(t-T_I)}\\+\left[\begin{array}{l}+\dfrac{K_I}{F_A+F_V+K_I}\left(\dfrac{A_G}{\mu_B}-\dfrac{A_B}{\mu_B^2}\right)\\-\dfrac{F_A+F_V}{F_A+F_V+K_I}\dfrac{1}{1/T_E-\mu_B}\left(\dfrac{A_B}{1/T_E-\mu_B}+A_G\right)\end{array}\right]e^{-\mu_B(t-T_I)}\\+\left[-\dfrac{K_I}{F_A+F_V+K_I}\dfrac{A_G}{\mu_G}+\dfrac{F_A+F_V}{F_A+F_V+K_I}\dfrac{A_G}{1/T_E-\mu_G}\right]e^{-\mu_G(t-T_I)}\\+\dfrac{K_I}{F_A+F_V+K_I}\left(\dfrac{A_B}{\mu_B^2}-\dfrac{A_G}{\mu_B}+\dfrac{A_G}{\mu_G}\right)\\+\dfrac{F_A+F_V}{F_A+F_V+K_I}\left(\dfrac{A_G}{1/T_E-\mu_B}-\dfrac{A_G}{1/T_E-\mu_G}+\dfrac{A_B}{(1/T_E-\mu_B)^2}\right)e^{-\frac{F_A+F_V+K_I}{V_E}(t-T_I)}\end{array}\right]_I$$

4

$$
\begin{aligned}
&= \sum_{I=A,V} F_I \left[\begin{array}{l}
+ \left[\begin{array}{l} -\dfrac{K_I}{F_A+F_V+K_I}\dfrac{A_B}{\mu_B} \\ +\dfrac{F_A+F_V}{F_A+F_V+K_I}\dfrac{A_B V_E}{F_A+F_V+K_I-\mu_B V_E} \end{array} \right] (t-T_I)\, e^{-\mu_B (t-T_I)} \\
+ \left[\begin{array}{l} +\dfrac{K_I}{F_A+F_V+K_I}\left(\dfrac{A_G}{\mu_B}-\dfrac{A_B}{\mu_B^2}\right) \\ -\dfrac{F_A+F_V}{F_A+F_V+K_I}\dfrac{V_E}{F_A+F_V+K_I-\mu_B V_E} \\ *\left(+\dfrac{A_B V_E}{F_A+F_V+K_I-\mu_B V_E}+A_G\right) \end{array} \right] e^{-\mu_B (t-T_I)} \\
+ \left[\begin{array}{l} -\dfrac{K_I}{F_A+F_V+K_I}\dfrac{A_G}{\mu_G} \\ +\dfrac{F_A+F_V}{F_A+F_V+K_I}\dfrac{A_G V_E}{F_A+F_V+K_I-\mu_G V_E} \end{array} \right] e^{-\mu_G (t-T_I)} \\
+\dfrac{K_I}{F_A+F_V+K_I}\left(\dfrac{A_B}{\mu_B^2}-\dfrac{A_G}{\mu_B}+\dfrac{A_G}{\mu_G}\right) \\
+\dfrac{F_A+F_V}{F_A+F_V+K_I} V_E \left(\begin{array}{l} +\dfrac{A_G}{F_A+F_V+K_I-\mu_B V_E} \\ -\dfrac{A_G}{F_A+F_V+K_I-\mu_G V_E} \\ +\dfrac{A_B V_E}{\left(F_A+F_V+K_I-\mu_B V_E\right)^2} \end{array} \right) e^{-\frac{F_A+F_V+K_I}{V_E}(t-T_I)}
\end{array} \right]_I \\
&= \sum_{I=A,V} F_I \left[\begin{array}{l}
+A_B \dfrac{\mu_B V_E - K_I}{\mu_B\left(F_A+F_V+K_I-\mu_B V_E\right)} (t-T_I)\, e^{-\mu_B (t-T_I)} \\
-\left[\begin{array}{l} +A_B \dfrac{\left(\mu_B V_E-K_I\right)^2+\left(F_A+F_V\right)K_I}{\mu_B^2\left(F_A+F_V+K_I-\mu_B V_E\right)^2} \\ +A_G \dfrac{\mu_B V_E-K_I}{\mu_B\left(F_A+F_V+K_I-\mu_B V_E\right)} \end{array} \right] e^{-\mu_B (t-T_I)} \\
+A_G \dfrac{\mu_G V_E-K_I}{\mu_G\left(F_A+F_V+K_I-\mu_G V_E\right)} e^{-\mu_G (t-T_I)} \\
+\dfrac{F_A+F_V}{F_A+F_V+K_I} V_E^2 \\
*\left(\begin{array}{l} +A_B \dfrac{1}{\left(F_A+F_V+K_I-\mu_B V_E\right)^2} \\ +A_G \dfrac{\left(\mu_B-\mu_G\right)}{\left(F_A+F_V+K_I-\mu_B V_E\right)\left(F_A+F_V+K_I-\mu_G V_E\right)} \end{array} \right) e^{-\frac{F_A+F_V+K_I}{V_E}(t-T_I)} \\
+\dfrac{K_I}{F_A+F_V+K_I}\left(\dfrac{A_B}{\mu_B^2}-\dfrac{A_G}{\mu_B}+\dfrac{A_G}{\mu_G}\right)
\end{array} \right]_I .
\end{aligned}
\tag{4.34}
$$

Note: a unit step function $u(t - T_I)$ should be added to Eq. 4.34.

APPENDIX 3: DERIVATION FROM SIGNAL INTENSITY TO TISSUE CONCENTRATION

In DCE-MRI, the signal in steady state is given by (neglecting T_2^* effect):

$$S(T_1) = N(H)\sin(\alpha)\frac{1-e^{-\frac{TR}{T_1}}}{1-\cos(\alpha)\,e^{-\frac{TR}{T_1}}}, \tag{4.35}$$

where $N(H)$ is the local proton density multiplied by an arbitrary factor, T_1 the spin-lattice relaxation time, α the flip-angle and T_R the repetition time.

The Relative Signal Intensity (RSI) in a voxel can be calculated as

$$\begin{aligned} RSI(T_1) &= \frac{S(T_1)}{S(T_{10})} \\ &= \frac{1-e^{-\frac{TR}{T_1}}}{1-\cos(\alpha)\,e^{-\frac{TR}{T_1}}}\frac{1-\cos(\alpha)\,e^{-\frac{TR}{T_{10}}}}{1-e^{-\frac{TR}{T_{10}}}} \\ &= \frac{1-E}{1-\cos(\alpha)\,E}F, \end{aligned} \tag{4.36}$$

in which

$$\begin{cases} E = e^{-\frac{TR}{T_1}} \\ F = \dfrac{1-\cos(\alpha)\,e^{-\frac{TR}{T_{10}}}}{1-e^{-\frac{TR}{T_{10}}}} \end{cases}.$$

Solving for E yields:

$$E = \frac{F - RSI(T_1)}{F - \cos(\alpha)\,RSI(T_1)}. \tag{4.37}$$

Expanding E and solving for $1/T_1(t)$:

$$\frac{1}{T_1} = -\frac{1}{TR}\ln\left(\frac{F - RSI(T_1)}{F - \cos(\alpha)\,RSI(T_1)}\right). \tag{4.38}$$

Next, the concentration of contrast agent can be computed from T_1:

$$\frac{1}{T_1(t)} = \frac{1}{T_0} + RC_t(t), \tag{4.39}$$

with R the relaxivity of the applied contrast agent.

Solving $C_T'(t)$:

$$\begin{aligned} C_T(t) &= \frac{1}{R}\left(\frac{1}{T_1(t)} - \frac{1}{T_{10}}\right) \\ &= \frac{1}{R}\left(-\frac{1}{TR}\ln\left(\frac{F - RSI(T_1)}{F - \cos(\alpha)\,RSI(T_1)}\right) - \frac{1}{T_{10}}\right) \\ &= \frac{1}{R}\left(-\frac{1}{TR}\ln\left(\frac{\frac{1-\cos(\alpha)e^{-\frac{TR}{T_{10}}}}{1-e^{-\frac{TR}{T_{10}}}} - RSI(T_1)}{\frac{1-\cos(\alpha)e^{-\frac{TR}{T_{10}}}}{1-e^{-\frac{TR}{T_{10}}}} - \cos(\alpha)\,RSI(T_1)}\right) - \frac{1}{T_{10}}\right). \end{aligned} \tag{4.40}$$

which is as same as Eq. 4.13 in the manuscript.

REFERENCES

[1] A. Jackson, D. L. Buckley, and G. J. M. Parker, *Dynamic contrast-enhanced magnetic resonance imaging in oncology* (Springer, 2005).

[2] S. Sourbron, W. H. Sommer, M. F. Reiser, and C. J. Zech, *Combined Quantification of Liver Perfusion and Function with Dynamic Gadoxetic Acid-enhanced MR Imaging,* Radiology **263**, 874 (2012).

[3] H.-K. Ryeom, S.-H. Kim, J.-Y. Kim, H.-J. Kim, J.-M. Lee, Y.-M. Chang, Y.-S. Kim, and D.-S. Kang, *Quantitative evaluation of liver function with MRI Using Gd-EOB-DTPA.* Korean journal of radiology : official journal of the Korean Radiological Society **5**, 231 (2004).

[4] H. Nilsson, A. Nordell, R. Vargas, L. Douglas, E. Jonas, and L. Blomqvist, *Assessment of hepatic extraction fraction and input relative blood flow using dynamic hepatocyte-specific contrast-enhanced MRI,* Journal of Magnetic Resonance Imaging **29**, 1323 (2009).

[5] R. Materne, a. M. Smith, F. Peeters, J. P. Dehoux, a. Keyeux, Y. Horsmans, and B. E. Van Beers, *Assessment of hepatic perfusion parameters with dynamic MRI.* Magnetic resonance in medicine : official journal of the Society of Magnetic Resonance in Medicine / Society of Magnetic Resonance in Medicine **47**, 135 (2002).

[6] J. L. Ulloa, S. Stahl, J. Yates, N. Woodhouse, J. G. Kenna, H. B. Jones, J. C. Waterton, and P. D. Hockings, *Assessment of gadoxetate DCE-MRI as a biomarker of hepatobiliary transporter inhibition.* NMR in biomedicine **26**, 1258 (2013).

[7] M. F. Forsgren, O. Dahlqvist Leinhard, N. Dahlström, G. Cedersund, and P. Lundberg, *Physiologically realistic and validated mathematical liver model revels hepatobiliary transfer rates for Gd-EOB-DTPA using human DCE-MRI data.* PloS one **9**, e95700 (2014).

[8] L. Georgiou, J. Penny, G. Nicholls, N. Woodhouse, F.-X. Blé, P. L. H. Cristinacce, and J. H. Naish, *Quantitative assessment of liver function using gadoxetate-enhanced magnetic resonance imaging,* Investigative Radiology **52**, 111 (2017).

[9] J. Ning, Z. Yang, S. Xie, Y. Sun, C. Yuan, and H. Chen, *Hepatic function imaging using dynamic Gd-EOB-DTPA enhanced MRI and pharmacokinetic modeling,* Magnetic Resonance in Medicine **1495**, 1488 (2016).

[10] B. Park, B. S. Choi, Y. S. Sung, D.-C. Woo, W. H. Shim, K. W. Kim, Y. S. Choi, S. J. Pae, J.-Y. Suh, H. Cho, and Others, *Influence of B1-Inhomogeneity on Pharmacokinetic Modeling of Dynamic Contrast-Enhanced MRI: A Simulation Study,* Korean Journal of Radiology **18**, 585 (2017).

[11] A. Sengupta, R. K. Gupta, and A. Singh, *Evaluation of B1 inhomogeneity effect on DCE-MRI data analysis of brain tumor patients at 3T,* Journal of translational medicine **15**, 242 (2017).

[12] J. J. N. van Schie, C. Lavini, L. J. van Vliet, and F. M. Vos, *Feasibility of a fast method for B1-inhomogeneity correction for FSPGR sequences,* Magnetic Resonance Imaging **33**, 312 (2015).

[13] K. Nehrke and P. Börnert, *DREAM-a novel approach for robust, ultrafast, multislice B1 mapping,* Magnetic Resonance in Medicine **68**, 1517 (2012).

[14] M. P. Heinrich, M. Jenkinson, B. W. Papiez, S. M. Brady, and J. A. Schnabel, *Towards realtime multimodal fusion for image-guided interventions using self-similarities,* in *Lecture Notes in Computer Science (including subseries Lecture Notes in Artificial Intelligence and Lecture Notes in Bioinformatics)*, Vol. 8149 LNCS (2013) pp. 187–194.

[15] T. Zhang, Z. Li, J. H. Runge, C. Lavini, J. Stoker, T. van Gulik, L. J. van Vliet, and F. M. Vos, *Improved registration of DCE-MR images of the liver using a prior segmentation of the region of interest,* (2016).

[16] Y. Zhang, B. J. Matuszewski, L.-K. Shark, and C. J. Moore, *Medical Image Segmentation Using New Hybrid Level-Set Method,* in *2008 Fifth International Conference BioMedical Visualization: Information Visualization in Medical and Biomedical Informatics* (2008) pp. 71–76.

[17] M. R. Orton, J. A. D'Arcy, S. Walker-Samuel, D. J. Hawkes, D. Atkinson, D. J. Collins, and M. O. Leach, *Computationally efficient vascular input function models for quantitative kinetic modelling using DCE-MRI,* Physics in Medicine and Biology **53**, 1225 (2008).

[18] J. J. van Schie, C. Lavini, L. J. van Vliet, and F. M. Vos, *Estimating the arterial input function from dynamic contrast-enhanced MRI data with compensation for flow enhancement (I): Theory, method, and phantom experiments,* Journal of Magnetic Resonance Imaging **47**, 1190 (2018).

[19] S. Aronhime, C. Calcagno, G. H. Jajamovich, H. A. Dyvorne, P. Robson, D. Dieterich, M. I. Fiel, V. Martel-Laferriere, M. Chatterji, H. Rusinek, and B. Taouli, *DCE-MRI of the liver: effect of linear and nonlinear conversions on hepatic perfusion quantification and reproducibility.* Journal of magnetic resonance imaging : JMRI **40**, 90 (2014).

[20] M. Rohrer, H. Bauer, J. Mintorovitch, M. Requardt, and H. J. Weinmann, *Comparison of magnetic properties of MRI contrast media solutions at different magnetic field strengths,* Investigative Radiology **40**, 715 (2005), arXiv:arXiv:1011.1669v3 .

[21] C. M. J. de Bazelaire, G. D. Duhamel, N. M. Rofsky, and D. C. Alsop, *MR Imaging Relaxation Times of Abdominal and Pelvic Tissues Measured in Vivo at 3.0 T: Preliminary Results,* Radiology **230**, 652 (2004).

[22] H. Akaike, *Information theory and an extensión of the maximum likelihood principle,* International symposium on information theory , 267 (1973).

[23] G. Schwarz, *Estimating the Dimension of a Model,* The Annals of Statistics **6**, 461 (1978), arXiv:arXiv:1011.1669v3 .

[24] H. Bozdogan, *ICOMP: A new model-selection criterion.* in *1. Conference of the International Federation of Classification Societies* (1987) pp. 599–608.

5

A Hybrid Segmentation Method for Partitioning the Liver Based on 4D DCE-MR Images

The Couinaud classification of hepatic anatomy partitions the liver into eight functionally independent segments. Detection and segmentation of the hepatic vein (HV), portal vein (PV) and inferior vena cava (IVC) plays an important role in the subsequent delineation of the liver segments.

To facilitate pharmacokinetic modeling of the liver based on the same data as delineating the liver segments, a 4D DCE-MR scan protocol was selected. This yields images with high temporal resolution but low spatial resolution. Since the liver's vasculature consists of many tiny branches, segmentation of these images is challenging. The proposed framework starts with registration of the 4D DCE-MRI series followed by region growing from manually annotated seeds in the main branches of key blood vessels in the liver. It calculates the Pearson correlation between the time intensity curves (TICs) of a seed and all voxels. A maximum correlation map for each vessel is obtained by combining the correlation maps for all branches of the same vessel through a maximum selection per voxel. The maximum correlation map is incorporated in a level set scheme to individually delineate the main vessels. Subsequently, the eight liver segments are segmented based on three vertical intersecting planes fit through the three skeleton branches of HV and IVC's center of mass as well as a horizontal plane fit through the skeleton of PV.

Our segmentation regarding delineation of the vessels is more accurate than the results of two state-of-the-art techniques on five subjects in terms of the average symmetric surface distance (ASSD) and modified Hausdorff distance (MHD). Furthermore, the proposed liver partitioning achieves large overlap with manual reference segmentations (expressed in Dice Coefficient) in all but a small minority of segments (mean values between 87% and 94% for segments 2-8). The lower mean overlap for segment 1 (72%) is due to the limited spatial resolution of our DCE-MR scan protocol.

5.1. INTRODUCTION

DURING liver surgery, resection of lesions inevitably goes at the expense of healthy liver tissue. To reduce this loss as much as possible and to limit the mortality rates after surgery, the Couinaud classification of liver anatomy was introduced [2]. This classification system partitions the liver into eight segments such that each of them has an independent circulatory system. It targets resecting only that segment in which the tumor is localized, without damaging the liver parenchyma of adjacent segments [3].

Conventionally, radiologists apply the Couinaud classification by manually annotating vessels in the liver, which is tedious, time-consuming and prone to errors. Accurate automatic methods for segmenting vessels are desired to improve the time efficiency. Several segmentation methods have been proposed, especially for computed tomography (CT) images which have relatively high spatial resolution [4][5]. However, the problem remains unsolved when it comes to magnetic resonance (MR) images, which is likely related to the lower spatial resolution of MR compared to CT imaging.

In this paper, we introduce a segmentation framework partitioning the liver according to Couinaud's classification of liver anatomy based on 4D dynamic contrast-enhanced magnetic resonance imaging (DCE-MRI) data. These data have high temporal resolution, but limited spatial resolution. We will show that our framework facilitates the segmentation of the liver vessels and in turn enables the segmentation of the eight liver segments.

5.2. METHODOLOGY

THIS study included 5 patients diagnosed with colorectal liver metastasis (3), hepatocellular carcinoma (1) and benign (1). All scans were operated between December 2014 and Sep 2015. The final cohort (age range, 65–76 years; mean age, 64.8 years) included 3 men (age range, 50–70 years; mean age, 61.7 years) and 2 women (age range, 63–76 years; mean age, 69.5 years). The study was approved by the ethical review board of the Amsterdam University Medical Centers and registered under ID NL45755.018.13. Informed consent was obtained from all individual participants included in the study.

DCE-MRI data were acquired on a 3T Philips Ingenia whole-body scanner via a 3D SPGR sequence. The x-axis of the data corresponds to the anterior-posterior direction, the y-axis to the left-right direction and the z-axis to the superior-inferior direction. The acquisition parameter settings were T_E/T_R = 2.3/3.75 ms, FA = 15°, matrix size = 128×128×44, voxel size = 3×3×5 mm^3, acquisition time = 2.141 s for each volume; sampling interval (between images) was 2.141 s for volumes 1-81, 30 s for volumes 82-98, and 60 s for volumes 99-108. The total imaging time was approximately 20 minutes.

5.2.1. REGISTRATION

To achieve spatial correspondence between corresponding voxels of the data, each 4D DCE-MR image series is registered to the last dynamic volume. In order to do so, we apply the registration framework Optimized Starting Points by Robust Fitting (OSPARF). It is described in Chapter 3, in which the registration kernel is the self-similarity context (SSC) method [6], which is a state-of-the-art technique for multi-modal image registration. Essentially, it is a patch-based descriptor of the structure in a certain neighborhood layout

Published in Proc. SPIE, **10574**, 1057434 (2018) [1].

N, defined as:

$$SSC\left(I,\mathbf{x},\mathbf{y}\right)=\exp\left[-\frac{D\left(I,\mathbf{x},\mathbf{y}\right)}{V\left(I,\mathbf{x}\right)}\right]\mathbf{x},\mathbf{y}\in N \tag{5.1}$$

in which I is an image, $\mathbf{x}$ and $\mathbf{y}$ are the center locations of two patches within N, and D is the distance between the two image patches measured by the sum of squared differences (SSD):

$$D\left(I,\mathbf{x_1},\mathbf{x_2}\right)=\sum_{\mathbf{y}\in N}\left[I\left(\mathbf{x}_1+\mathbf{y}\right)-I\left(\mathbf{x}_2+\mathbf{y}\right)\right]^2 \tag{5.2}$$

and $V(I, N)$ is the mean of the patch distances in neighborhood N:

$$V\left(I,N\right)=\frac{1}{num\left(N\right)}\sum_{\mathbf{x},\mathbf{y}\in N}D\left(I,\mathbf{x},\mathbf{y}\right) \tag{5.3}$$

The SSC operator is based on all distances in a six neighborhood (with a Euclidean distance of $\sqrt{2}$ between them), while the central pixel is excluded from N.

SSC registration can be described as

$$\mathbf{u}^*=\arg\min_{\mathbf{u}}\left\{\sum_{\mathbf{x}}\left[\frac{1}{|R|}\sum_{\mathbf{r}\in R}|SSC\left(I,\mathbf{x},\mathbf{r}\right)-SSC\left(J,\mathbf{x},\mathbf{r}\right)|\right]+\alpha|\nabla\mathbf{u}\left(\mathbf{x}\right)|^2\right\} \tag{5.4}$$

where $\mathbf{u} = (u, v, w)$ is the deformation field and α the regularization parameter, i.e. a coefficient that weighs the regularization term.

In this paper we follow the default setup as introduced in [6]: $R = 3$, $N = N_6$, i.e. a six-connected neighborhood, patch size $D = 3$, and the regularization coefficient $\alpha = 0.1$.

5.2.2. SEGMENTATION OF THE HEPATIC VASCULATURE

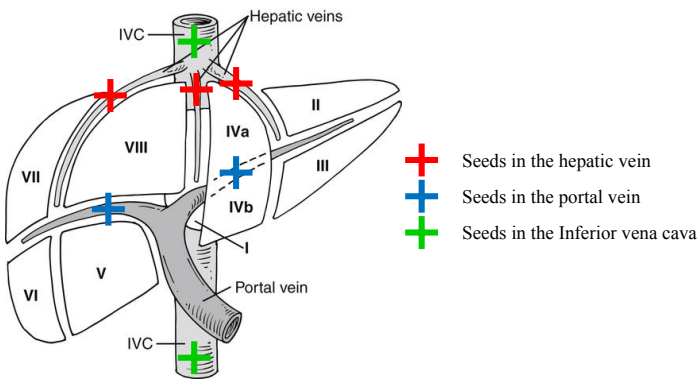

Figure 5.1: Locations of seed points in the hepatic vein (HV) including right, middle and left hepatic veins; portal vein (PV), including right and left portal veins; and inferior vena cava (IVC).

The Couinaud classification partitions the liver in functionally independent segments based on the vasculature. Our method resembles this standard method, but relies on

a semi-automatic segmentation of the key liver vessels. Specifically, a region growing method is applied to the 4D MR images to segment the main blood vessels as well as the liver. It adopts Pearson correlation between the time intensity curves (TICs) as distance metric [7]. Therefore, seeds are manually placed in the main branches of the liver's vasculature: hepatic vein (HV), portal vein (PV), and in the inferior vena cava (IVC), see Fig. 5.1 [8]. Since the blood in each main vessel has taken a different route through the human body, the TIC from each seed point is different. From each such seed the TIC is correlated with the entire 4D volume of TIC curves.

Subsequently, the maximum correlation is determined over the correlation maps for key vessel (HV, PV and IVC). As such, for each key vessel a separate maximum correlation map is obtained. Thereafter, the hybrid levelset segmentation method proposed by Y. Zhang *et al.* [9] is separately applied to the three maximum correlation maps. It takes boundary as well as region information into consideration while minimizing the next data term

$$E(\phi) = -\int_{\Omega} (I-\mu)\, H(\phi)\, d\Omega + \beta \int_{\Omega} g\, |\nabla H(\phi)|\, d\Omega \tag{5.5}$$

where I is the image, g represents the gradient of the image, β is a weighting coefficient, $H(\phi)$ is the Heaviside function, and μ is a parameter that represents the lower bound of the gray-level in the segmented object. The level set method is initiated by small spheres placed at the seed points. As such, a region growing method is applied to segment the branches of the hepatic vein (HV), portal vein (PV) and inferior vena cava (IVC). In addition, the first dynamic image is subtracted from the last dynamic image of the registered DCE-MRI series. Subsequently, the liver is segmented based on the resulting "contrast" volume by means of a level set approach [10].

All algorithms were implemented in MATLAB (version R2015b; Mathworks, Natick, USA). For the region growing method, three parameters, including the seed point, correlation threshold, maximum search distance were set for each case; For the level set method, three parameters, including the starting point, μ and β were set for each case. The detailed setting can be seen in the appendix 1 and 2.

5.2.3. DEFINITION OF HEPATIC SEGMENTS

In order to delineate the liver segments, skeletons representing the vessels are obtained by parallel medial axis thinning as described in Ref. [11]. Example skeletons of the hepatic vein (HV), portal vein (PV) and inferior vena cava (IVC) are shown in Fig. 5.2(a) and Fig. 5.3(a). The partitioning of the liver is carried out according to Couinaud's classification using intersegmental planes [12]. For the vertical partitioning, i.e. along the scan's z-axis, three planes spanned by the three main branches of HV were defined respectively. They can be generally expressed as

$$Ax + By = 1 \tag{5.6}$$

In Fig. 5.2(a), the HVs and the IVC are projected onto the xy-plane. For each HV branch, Eq. 5.6 is fit through the projected skeleton points and the IVC's center of mass. These are depicted by the red dashed points and green cross-shaped point in Fig. 5.2(a), respectively. As such, the liver is divided into four lobes as shown in Fig. 5.2(b).

The skeleton of the PV is shown in Fig. 5.3(a). A horizontal plane fit through the PV's skeleton divides the superior and inferior liver lobes, as show in Fig. 5.3(b).

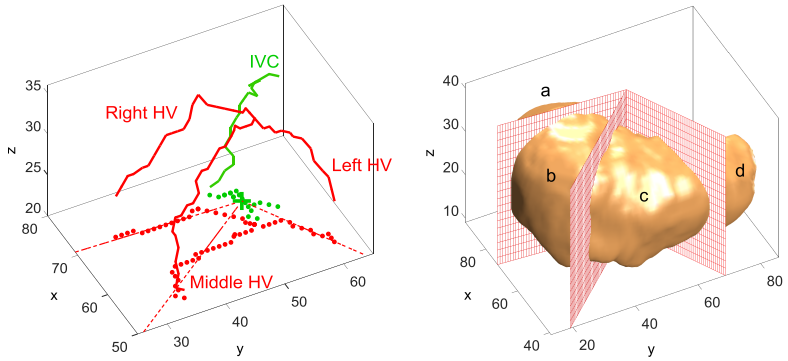

Figure 5.2: (a) The skeletons of left, middle, right HVs and IVC obtained by thinning the segmented structures. The red and green dashed points represent the coordinates of HVs and IVC projected onto the xy-plane. The green, cross-shaped symbol denotes the IVC's projected center of mass; (b) The three vertical planes dividing the liver into four parts; the lobes labeled a-d are defined as right posterior section, right anterior section, left medial section and left lateral section, respectively.

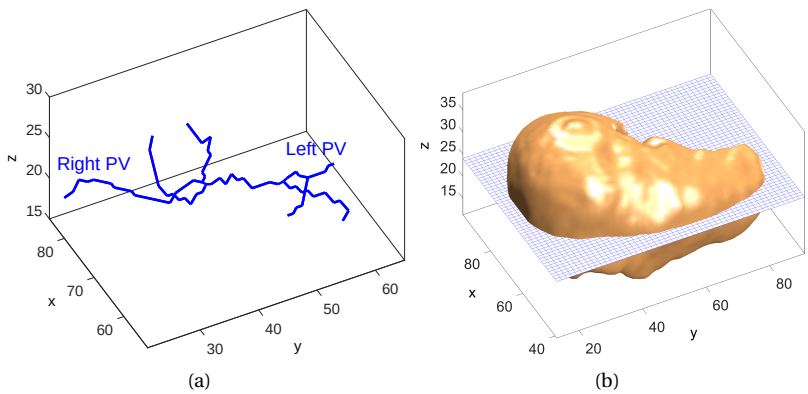

Figure 5.3: (a) The skeleton of the PV; (b) liver partitioning by fitting a horizontal plane.

In Couinaud's classification, the first segment is roundish and located around the region between the HV and IVC. However, the border between segment 1 and the other segments is not visible in our DCE-MR images due to the low spatial resolution. Therefore, the combination of half a sphere and cylinder is adopted to model the shape of segment 1. The modeling procedure is illustrated in Fig. 5.4. In the horizontal resection plane, an inscribing sphere is defined centered at the projected IVC's center of mass and with a radius equal to the distance between the IVC's center of mass and the nearest point on the PV skeleton. Subsequently, a cylinder with the same radius as the sphere extends from the sphere in the positive y-direction. The cylindrical segment thus delineated is truncated by

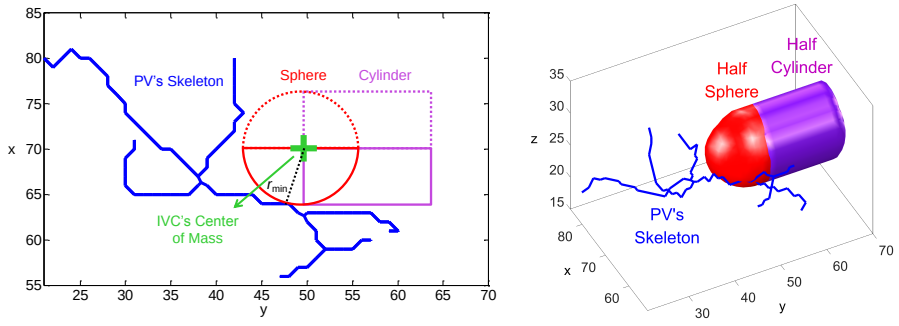

(a) (b)

Figure 5.4: Modeling of liver segment 1. (a) An inscribing sphere is defined centered at the IVC's projected center-of-mass (on the horizontal plane from Fig. 5.3), whose radius is determined by the nearest point of the PV skeleton. The sphere was extended by a cylindrical segment of the same radius in the positive y-direction. The red and purple solid lines indicate the half (of the sphere and cylinder) that is kept while the dashed lines correspond to the half that is removed; (b) the illustration of the kept half sphere and cylinder. Their combination is the final model to identify liver segment 1.

5

the border of the liver mask obtained as described below Eq. 5.5. The extended sphere is also truncated by the vertical plane as indicated in Fig. 5.4(a).

Table 5.1: Conditions delineating the liver segments. A and B: constant parameters for each plane definition. L: left, R: right, LHV: left hepatic vein, MHV: middle hepatic vein, RHV: right hepatic vein, PV: portal vein, IVC's CM: IVC's center of mass in the horizontal resection plane. r_{min}: the distance between IVC's center of mass and the nearest point on PV's skeleton.

Segment	Defining Conditions
1	$x^2+y^2+z^2 < r_{\text{min}}^2 \quad | \quad y^2+z^2 < r_{\text{min}}^2 \quad \& \quad x < x_{IVC'sCM}$
2	$A_{LHV}x + B_{LHV}y > 1 \quad \& \quad z > z_{PV}$
3	$A_{LHV}x + B_{LHV}y > 1 \quad \& \quad z < z_{PV}$
4	$A_{LHV}x + B_{LHV}y < 1 \quad \& \quad A_{MHV}x + B_{MHV}y < 1$
5	$A_{RHV}x + B_{RHV}y < 1 \quad \& \quad A_{MHV}x + B_{MHV}y > 1 \quad \& \quad z < z_{PV}$
6	$A_{RHV}x + B_{RHV}y > 1 \quad \& \quad z < z_{PV}$
7	$A_{RHV}x + B_{RHV}y > 1 \quad \& \quad z > z_{PV}$
8	$A_{RHV}x + B_{RHV}y < 1 \quad \& \quad A_{MHV}x + B_{MHV}y > 1 \quad \& \quad z > z_{PV}$

Table 5.1 summarizes the conditions to define the eight liver segments. Each segment consists of voxel points (x, y, z), which satisfy the corresponding conditions. The first segment was calculated and excluded before the other segments were determined.

5.3. RESULTS

FIG. 5.5 shows the correlation map for each branch of the hepatic vein. Note that each branch obtains the highest correlation in its individual map. As a result, the maximum selection map gets the highest contrast of the hepatic vein from a global point of view. The

portal vein and inferior vena cava are processed in the same way.

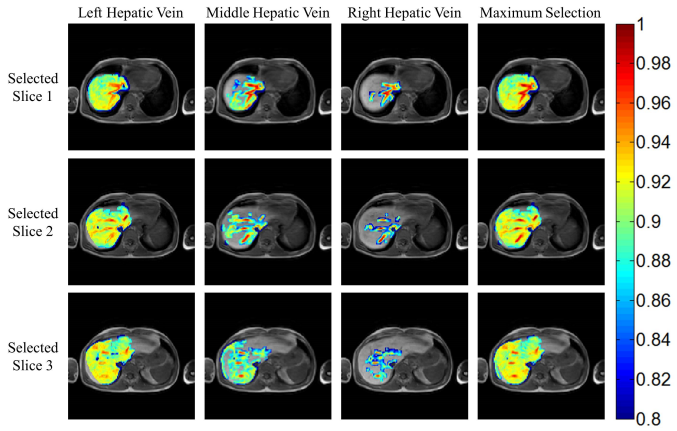

Figure 5.5: The first three columns: Correlation maps in three slices of the left, middle and right hepatic veins, respectively; Last column: The HV maximum correlation map composed by voxel-based maximum selection of correlation maps in the first three columns.

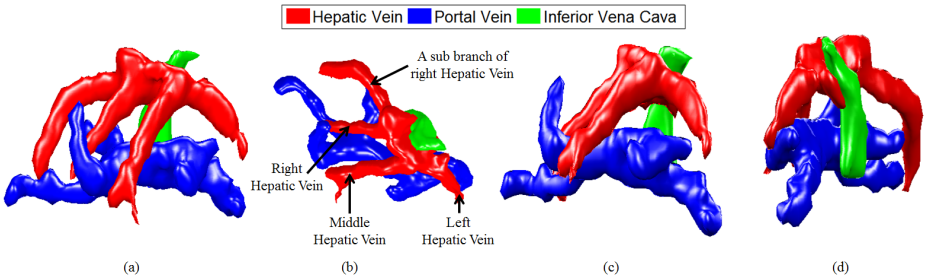

Figure 5.6: The segmentation of hepatic vein, portal vein and inferior vena cava in one subject. (a) 3D view; (b) top view; (c) front view; (d) side view.

Fig. 5.6 shows the segmentation of the three key vessels from the liver as obtained by the aforementioned level set method. The vessels were also segmented by means of two state-of-the-art techniques, based on respectively a vesselness enhancement filter (VEF) [13] and a diffusion enhancing filter (DEF) [5]. An experienced radiologist manually delineated the vessels, which served as the reference standard. The accuracy of the semi-automatic methods was evaluated by means of the average symmetric surface distance (ASSD) and modified Hausdorff distance (MHD) on data of five subjects as shown in Table 5.2. The ASSD and MHD were calculated according to the following equations:

$$ASSD = \frac{\sum_{a \in A} \min_{b \in M} \|a-b\| + \sum_{b \in M} \min_{a \in A} \|a-b\|}{2\,(N_A + N_M)} \tag{5.7}$$

$$MHD(A,B) = \max\left\{\frac{1}{N_A}\sum_{a\in A}\min_{b\in B}\|a-b\|, \frac{1}{N_B}\sum_{b\in B}\min_{a\in A}\|a-b\|\right\} \tag{5.8}$$

Table 5.2: Average symmetric surface distance (ASSD) and modified Hausdorff distance (MHD) of vessels segmented from five clinical cases with the proposed hybrid method and two standard techniques compared to manually annotated reference segmentations. VEF stands for a method based on a vesselsness enhancement filter; DEF represents a diffusion enhancement filter (DEF) based technique. The numbers printed in boldface are the best result per row. All measures are in mm.

Metric	ASSD			MHD		
Method	VEF	DEF	Ours	VEF	DEF	Ours
Case 1	6.004	5.246	**4.206**	8.496	6.145	**4.254**
Case 2	6.351	6.155	**5.580**	9.668	8.885	**6.894**
Case 3	6.619	7.769	**6.560**	9.883	9.409	**6.808**
Case 4	9.069	6.123	**5.271**	14.327	8.410	**7.828**
Case 5	7.534	9.201	**6.399**	12.142	13.392	**7.616**
Average	7.115	6.899	**5.603**	10.903	9.248	**6.680**

5

After segmentation of the key vessels, the functional liver segments are delineated by applying the method described in Sec. 5.2.3. In Fig. 5.7, the eight segments of five subjects are visualized. Additionally, the proposed segmentations are compared with manual ones, which are annotated under the supervision of one experienced radiologist in Table 5.3. It shows that the proposed segmentation method achieves good results in all but a small minority of cases, particularly concerning segment 1.

Table 5.3: The Dice Coefficient (DC) of volumetric overlap between the result of the proposed method and the manual segmentation.

DC (%)	Segment 1	Segment 2	Segment 3	Segment 4
Case 1	79.25	92.89	91.34	86.40
Case 2	77.34	87.85	64.44	92.44
Case 3	68.84	92.40	95.19	85.81
Case 4	59.49	89.36	90.28	91.24
Case 5	76.88	96.23	94.54	95.03
Average	72.36	91.75	87.16	90.18

DC (%)	Segment 5	Segment 6	Segment 7	Segment 8
Case 1	86.76	93.68	90.95	77.90
Case 2	91.72	85.84	92.83	94.26
Case 3	92.35	88.70	93.84	91.27
Case 4	92.34	90.40	96.42	95.06
Case 5	93.67	92.38	96.01	93.42
Average	91.37	90.20	94.01	90.38

Figure 5.7: Visualization of eight functional liver segments from five subjects. (a)-(e) represent subject 1-5, respectively. Images in the first row give the front view while in the second row give the back view.

5.4. SUMMARY AND CONCLUSION

THE hybrid segmentation method proposed by us for partitioning the liver from DCE-MRI images consists of two steps. In the first step, a region growing method is applied to segment the branches of the hepatic vein (HV), the portal vein (PV) and inferior vena cava (IVC) from the liver. In the second step, skeletons of these segmented vessels are regarded as landmarks to partition functional liver segments. Comparison with state-of-the art methods shows that our method produces more accurate segmentations of the vessels in the liver. Moreover, our segmentations of functional liver segment have large overlap (measured through the Dice Coefficient) with a manually annotated reference. The proposed segmentation method can easily be adapted to other DCE-MRI or DCE-CT applications with low spatial resolutions.

APPENDIX 1: SETTINGS OF THE REGION GROWING METHOD

Table 5.4: Settings of the region growing method for 5 patients.

Case	Vessel	Seed point (x, y, z)	Correlation threshold	Maximum search distance
1	Hepatic Vein	60, 58, 30	0.9	40
		62, 44, 31	0.9	40
		71, 41, 31	0.9	40
	Portal Vein	65, 34, 24	0.8	30
		71, 40, 24	0.92	20
	Inferior Vena Cava	69, 53, 32	0.8	30
		73, 51, 27	0.8	30
2	Hepatic Vein	60, 62, 27	0.8	40
		66, 52, 28	0.8	40
		75, 49, 28	0.8	40
	Portal Vein	69, 40, 22	0.9	40
		75, 42, 22	0.9	40
	Inferior Vena Cava	68, 59, 31	0.9	30
		70, 56, 24	0.9	30
3	Hepatic Vein	60, 49, 36	0.8	40
		62, 41, 36	0.8	40
		75, 37, 36	0.8	40
	Portal Vein	59, 42, 27	0.9	50
		77, 37, 28	0.9	40
	Inferior Vena Cava	72, 49, 37	0.9	30
		72, 47, 23	0.9	30
4	Hepatic Vein	53, 56, 28	0.9	40
		61, 46, 28	0.9	40
		72, 39, 27	0.9	40
	Portal Vein	51, 48, 22	0.8	40
		63, 34, 22	0.8	40
	Inferior Vena Cava	66, 52, 33	0.8	30
		70, 53, 26	0.8	30
5	Hepatic Vein	57, 53, 32	0.9	40
		58, 42, 32	0.9	40
		67, 38, 32	0.9	40
	Portal Vein	46, 47, 23	0.8	40
		62, 42, 22	0.8	40
	Inferior Vena Cava	65, 51, 33	0.8	30
		66, 51, 22	0.8	30

APPENDIX 2: SETTINGS OF THE LEVEL SET METHOD

Table 5.5: Settings of the level set method for 5 patients.

Case	Vessel	Starting point (x, y, z)	μ	β
1	Hepatic Vein	67, 55, 31	0.89	1
	Portal Vein	61, 47, 24	0.93	1/30
	Inferior Vena Cava	70, 53, 31	0.9	1/20
2	Hepatic Vein	64, 57, 27	0.92	1/20
	Portal Vein	69, 40, 22	0.9	1/20
	Inferior Vena Cava	69, 53, 22	0.85	1/20
3	Hepatic Vein	65, 50, 37	0.9	1/20
	Portal Vein	72, 33, 29	0.92	1/20
	Inferior Vena Cava	74, 49, 33	0.92	1
4	Hepatic Vein	62, 54, 30	0.94	1
	Portal Vein	61, 33, 26	0.84	1/10
	Inferior Vena Cava	65, 53, 36	0.7	1/50
5	Hepatic Vein	56, 53, 33	0.92	1/10
	Portal Vein	61, 42, 24	0.85	1/5
	Inferior Vena Cava	67, 53, 39	0.8	1/50

REFERENCES

[1] T. Zhang, W. Zhiyi, Z. Li, J. H. Runge, C. Lavini, T. van Gulik, J. Stoker, K. P. Cieslak, L. J. van Vliet, and F. M. Vos, *A hybrid segmentation method for partitioning the liver based on 4d dce-mr images,* Proc.SPIE **10574**, 10574 (2018).

[2] C. Couinaud, *Le foie: {é}tudes anatomiques et chirurgicales* (Masson & Cie, 1957).

[3] E. M. Pauli, K. F. Staveley-O'Carroll, M. V. Brock, D. T. Efron, and G. Efron, *A handy tool to teach segmental liver anatomy to surgical trainees,* Archives of Surgery **147**, 692 (2012).

[4] Y. Chen, X. Yue, C. Zhong, and G. Wang, *Functional Region Annotation of Liver CT Image Based on Vascular Tree,* BioMed Research International **2016** (2016), 10.1155/2016/5428737.

[5] H. M. Luu, C. Klink, A. Moelker, W. Niessen, and T. van Walsum, *Quantitative evaluation of noise reduction and vesselness filters for liver vessel segmentation on abdominal CTA images,* Physics in Medicine and Biology **60**, 3905 (2015).

[6] M. P. Heinrich, M. Jenkinson, B. W. Papiez, S. M. Brady, and J. A. Schnabel, *Towards realtime multimodal fusion for image-guided interventions using self-similarities,* in *Lecture Notes in Computer Science (including subseries Lecture Notes in Artificial Intelligence and Lecture Notes in Bioinformatics)*, Vol. 8149 LNCS (2013) pp. 187–194.

[7] Y. Lu, T. Jiang, and Y. Zang, *Region growing method for the analysis of functional MRI data,* NeuroImage **20**, 455 (2003).

[8] *Liver | Clinical Gate,* .

[9] Y. Zhang, B. J. Matuszewski, L.-K. Shark, and C. J. Moore, *Medical Image Segmentation Using New Hybrid Level-Set Method,* (2008).

[10] T. Zhang, Z. Li, J. H. Runge, C. Lavini, J. Stoker, T. van Gulik, L. J. van Vliet, and F. M. Vos, *Improved registration of DCE-MR images of the liver using a prior segmentation of the region of interest, Proc. SPIE,* **9784**, 978443 (2016).

[11] T.-C. Lee, R. L. Kashyap, and C.-N. Chu, *Building skeleton models via 3-D medial surface axis thinning algorithms,* CVGIP: Graphical Models and Image Processing **56**, 462 (1994).

[12] Fat-kin Yan, *Automatic Segmentation of Functional Hepatic Segments on Computed Tomography*, Ph.D. thesis, University of Hong Kong (2011).

[13] T. Jerman, F. Pernus, B. Likar, and Z. Spiclin, *Enhancement of Vascular Structures in 3D and 2D Angiographic Images,* IEEE Transactions on Medical Imaging **35**, 2107 (2016).

6

Comparison Between Dynamic Gadoxetate-enhanced MRI and ^{99m}Tc-mebrofenin Hepatobiliary Scintigraphy with SPECT for Quantitative Assessment of Liver Function

Objectives

To compare Gd-EOB-DTPA dynamic hepatocyte specific contrast-enhanced MRI (DHCE-MRI) with ^{99m}Tc-mebrofenin hepatobiliary scintigraphy (HBS) as quantitative liver function tests for the preoperative assessment of patients undergoing liver resection.

Materials and Methods

Patients undergoing liver surgery and preoperative assessment of future remnant liver (FRL) function using ^{99m}Tc-mebrofenin HBS were included. Patients underwent DHCE-MRI. Total liver uptake function was calculated for both modalities: mebrofenin uptake rate (MUR) and Ki respectively. The FRL was delineated with both SPECT-CT and MRI to calculate the functional share. Blood samples were taken to assess biochemical liver parameters.

Results

A total of 20 patients were included. The HBS-derived MUR and the DHCE-MRI derived mean Ki correlated strongly for both total and FRL function (Pearson $r = 0.70$, $P = 0.001$ and $r = 0.89$, $P < 0.001$ respectively). There was a strong agreement between the functional share determined with both modalities (ICC = 0.944, 95% -CI: 0.863-0.978, n = 20). There was

a significant negative correlation between liver aminotransferases and bilirubin for both MUR and Ki.

Conclusions

Assessment of liver function with DHCE-MRI is comparable with that of ^{99m}Tc-mebrofenin HBS and has the potential to be combined with diagnostic MRI imaging. This can therefore provide a one-stop-shop modality for the preoperative assessment of patients undergoing liver surgery.

Published in European Radiology, 0938-7994 (2019) [1].

6.1. INTRODUCTION

SURGICAL resection remains the only curative treatment in patients with primary and metastatic liver tumors and is presently performed with limited morbidity and mortality [2, 3]. However, extended liver resection still comes with the risk of posthepatectomy liver failure (PHLF) with incidence reported between 0.7 and 9.1% [4]. An insufficient future remnant liver (FRL) is one of the most important risk factors for the development of PHLF. The current management of PHLF is merely supportive and has a mortality rate of over 80% [5, 6]. Therefore, preoperative assessment liver function is crucial in order to minimize the risk of developing PHLF.

Computed tomography (CT) volumetry is considered in many centers as the reference standard to assess FRL sufficiency. Essentially, it exploits the liver volume as an indirect measure for the liver function [7–9]. Depending on the quality of liver parenchyma, separate cutoff values are used to determine resectability [10]. However, liver function does not always correlate with volume and functional capacity may not be homogeneously distributed throughout the liver, especially in patients with impaired liver parenchyma [11]. Furthermore, the quality of liver parenchyma is not always determined preoperatively through liver biopsy, making estimation of FRL function based on CT volumetry alone unreliable [11].

Several quantitative dynamic liver function tests are currently used to assess hepatic uptake and excretory function. This can be done with hepatobiliary scintigraphy (HBS) using technetium-99m (^{99m}Tc) labelled iminodiacetic acid (IDA) derivates of which mebrofenin is the most hepatocyte specific [12]. This lidocaine analogue is taken up by the hepatocytes and is excreted in the bile canaliculi without undergoing any biotransformation [13]. The hepatic uptake is facilitated by the same mechanisms as other endo- and exogenous substances (e.g. bilirubin and hormones), making it a favorable agent to assess liver uptake and excretory function [14]. Because HBS provides a direct quantitative measure of the uptake function, it can be used in both patients with healthy or impaired liver parenchyma (e.g. steatosis, hepatitis and fibrosis) using the same cutoff value for the uptake rate (2.7 %/min/m^2) [11]. Furthermore, HBS is combined with SPECT-CT which provides information on the regional distribution of liver function, enabling a more anatomical evaluation of FRL function [15].

HBS has proven to predict the risk of PHLF in a mixed series of patients undergoing major liver resection and is part of standard practice for the preoperative assessment of patients undergoing liver resection in our center [11, 16–18]. Even though HBS provides simultaneous morphologic (visual) and physiologic (functional) information of the liver, it is not suitable for diagnostic purposes due to the relatively low spatial resolution. Patients undergo additional imaging for diagnostic purposes.

Alternatively, MRI with ethoxybenzyl diethylenetriaminepentaacetic acid (Gd-EOB-DTPA; Primovist®) as a contrast agent for evaluation of liver function was first performed in 1993 [19]. Subsequently, multiple studies showed correlation with liver function in both animal models and humans [20–25]. Gd-EOB-DTPA shares pharmacokinetic properties with mebrofenin, as both are taken up by hepatocytes and are excreted in the bile canaliculi without undergoing biotransformation. Furthermore, dynamic contrast-enhanced MRI (DCE-MRI) with gadolinium-based contrast agents allows accurate depiction of benign or malignant liver lesions [26–28]. Pharmacokinetic models (PKM) have been de-

veloped that facilitate the estimation of the uptake rate of the contrast agent based on DHCE-MRI with Gd-EOB-DTPA on a per voxel basis [29–31]. Diagnostic MRI followed by DHCE-MRI therefore potentially provides a detailed, one-stop-shop modality for both diagnostic purposes as well as accurate determination of FRL function.

The aim of this study is to compare Gd-EOB-DTPA-enhanced DHCE-MRI with ^{99m}Tc-mebrofenin HBS as liver function tests for the preoperative assessment of patients undergoing liver resection. We hypothesize that the liver function determined by DHCE-MRI correlates with ^{99m}Tc-mebrofenin HBS.

6.2. MATERIALS AND METHODS

6.2.1. PATIENTS

PATIENTS diagnosed with one or more liver lesions and who were scheduled for ^{99m}Tc-mebrofenin HBS as part of the preoperative workup were included in this prospective observational pilot study. Patients with general contraindications for MRI, chronic renal insufficiency, known or family history of congenital prolonged QT-syndrome, current use of cardiac repolarization time prolonging drugs (such as class 3 anti-arrhythmic drugs), history of arrhythmia after the use of cardiac repolarization time prolonging drugs and history of allergic reaction to gadolinium-containing compounds were excluded from participation. As this was a pilot study, no formal sample size calculation was performed. The study was approved by the ethical review board of the Amsterdam University Medical Centers and registered under ID NL45755.018.13. Informed consent was obtained from all individual participants included in the study.

6.2.2. HEPATOBILIARY SCINTIGRAPHY

All patients underwent HBS to evaluate total and FRL function prior to resection as described previously [11, 15]. Briefly, patients were imaged in supine position using a large field of view dual-head SPECT-CT camera (Siemens Symbia T16, Munich, Germany). Dynamic acquisitions were obtained (38 frames; 10s/frame) immediately after intravenous injection of 200 MBq ^{99m}Tc-mebrofenin (Bridatec, GE Healthcare, Little Chalfont, United Kingdom) in order to calculate the hepatic uptake rate, see Fig. 6.1 A. Subsequently, SPECT was performed (60 projections of 8 s/projection, 128 matrix) which was used for the 3-dimensional assessment of liver function and calculation of functional liver volume. This was followed by low-dose CT imaging for attenuation correction and anatomical mapping. Finally, dynamic acquisitions were obtained (15 frames; 60 s/frame, 128 matrix) to evaluate biliary excretion.

Data were processed on a Hermes workstation (Hermes Medical Solutions, Sweden). Geometric mean datasets of the anterior and posterior acquisitions were used for the analysis [15]. Regions of interest (ROI) were drawn delineating the liver, the left ventricle and aorta (representing the blood pool) and the total field of view (FOV), from which time-activity curves were created, see Fig. 6.1 B.

Total liver function (TLF) was represented by the mebrofenin uptake rate (MUR; %/min). This was calculated as an increase of ^{99m}Tc-mebrofenin uptake over a time period of 200 s as described by Ekman *et al.* [32].

The FRL was defined on the planned resection and was delineated manually on the

SPECT-CT images to calculate its functional share from HBS (FS HBS), which was defined as the fraction of counts within the FRL, see Fig. 6.1 C. Subsequently, this functional share fraction was multiplied by the TLF to calculate the FRL function (fMUR; %/min).

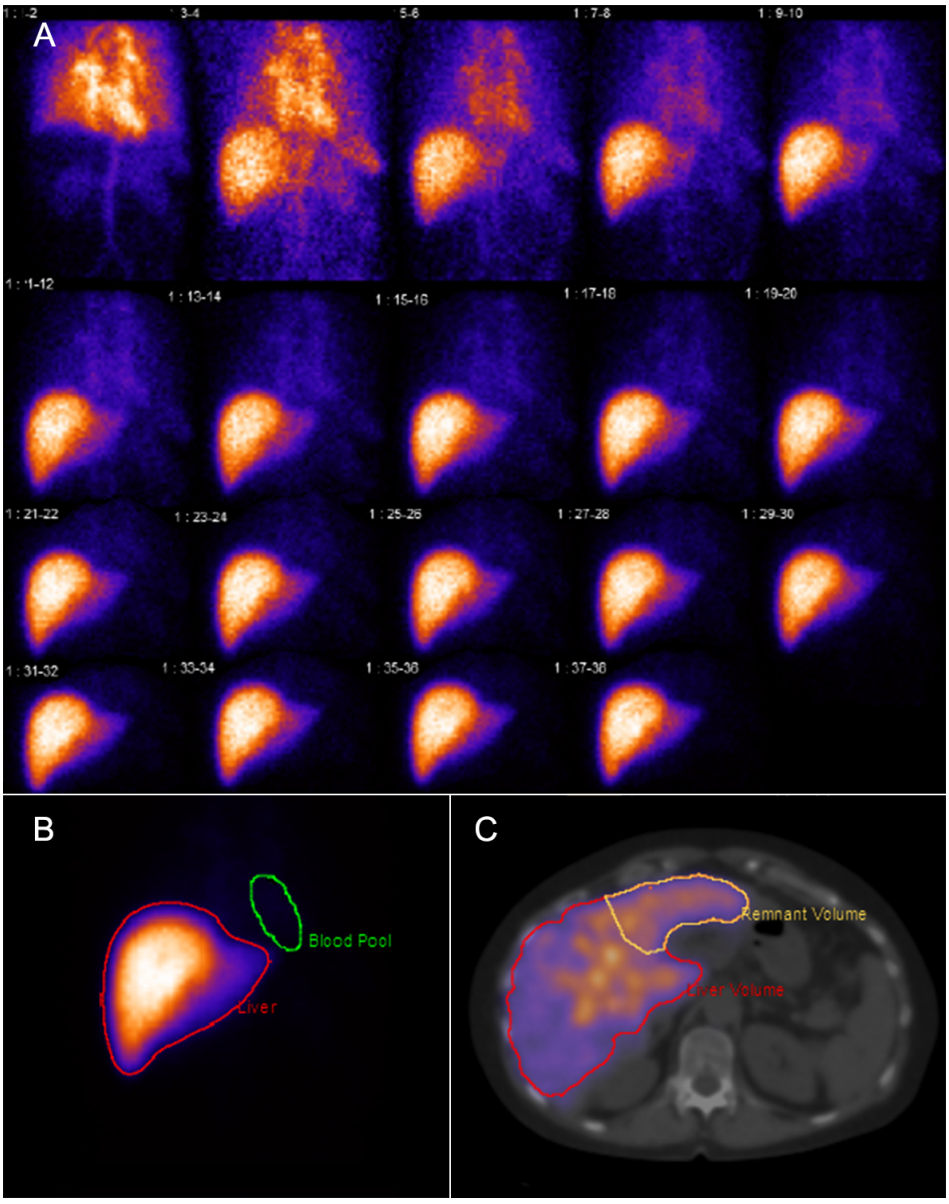

Figure 6.1: Hepatobiliary scintigraphy with series scintigram (A), ROI on summed images (B) and FRL delineation on SPECT/CT (C).

6.2.3. DHCE-MRI

DHCE-MRI data were acquired on a 3.0 Philips Ingenia whole-body MR-scanner (Philips Healthcare, Best, The Netherlands) by means of a Dynamic T_1-weighted 3D Spoiled Gradient Echo sequence. The acquisition parameter settings were TE/TR = 2.30/3.75 ms, FA = 15°, matrix size = 128×128×44, voxel size = 3×3×5 mm^3, acquisition time = 2.14 s for each volume; sampling interval (between images) was 2.14 s for volumes 1-81, 30 s for volumes 82-98, and 60 s for volumes 99-108. The total imaging for the dynamic series time was approximately 20 minutes. Subjects held their breath during the acquisition of volumes 13-22, 33-42, 61-70 and 79-108. Upon acquisition of dynamic 11 (i.e. 21 seconds after the start of the DHCE acquisition), a bolus of Gd-EOB-DTPA (Primovist®, Bayer B.V., Mijdrecht, The Netherlands) at a standard dose of 0.025 mmol/kg (i.e, 0.1 mL/kg) was administered at 2 mL/s and flushed with 20 mL of saline at the same rate through an antecubital intravenous cannula, see Fig. 6.2.

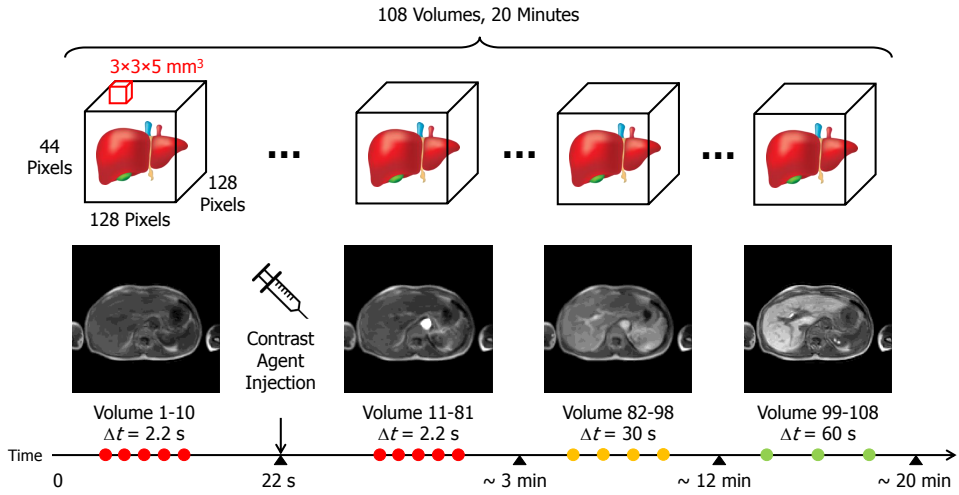

Figure 6.2: DHCE-MRI protocol

All post-processing was performed with in-house developed software implemented in MATLAB (R2015b; MathWorks, Natick, MA). The dynamic images were aligned to the first image in the series using the Self-Smilarity Context (SSC) method [33]. As such, spatial correspondence of the images was achieved across time. Subsequently, the liver was delineated using a semi-automatic segmentation method [34, 35]. The signal in each liver voxel was converted into time concentration curves assuming a nonlinear relationship between signal intensity and concentration of the contrast agent [36]. Furthermore, the liver's arterial input function (AIF) and its portal venous input function (VIF) describing the contrast agent concentration in the blood plasma supplied to the liver by the hepatic artery and the portal vein were estimated by averaging the top three of most enhancing time concentration curves of the voxels from homogeneous regions in the aorta and the portal vein respectively [34]. Additional details regarding the applied techniques are provided in Chapter 2.

In order to estimate the liver function, the pharmacokinetics of the liver were modeled from the MRI data based on COS-FLAC, the model proposed in Chapter 4. This model was developed from Sourbron's model [29]. It yielded the Gd-EOB-DTPA uptake rate (min^{-1}) in each voxel of the liver, which was averaged over the entire liver segmentation to represent the total liver's uptake rate Ki as measured with DHCE-MRI.

Additional semi-quantitative MRI study parameters were the relative enhancement (RE) and maximum slope of increase (MSI), see Fig. 6.3. RE was defined in each voxel as the difference of the signal at 20 minutes with the signal at baseline divided by the signal at baseline. MSI is defined as the maximum slope along the signal's time course. Both parameters were averaged over the entire liver.

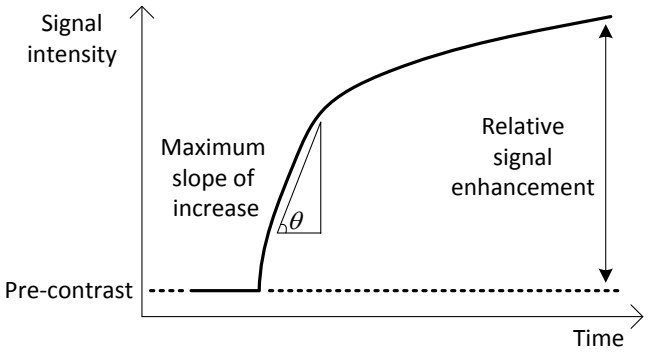

Figure 6.3: Signal intensity curve with semi-quantitative parameters.

For the calculation of the functional share from MRI, the FRL was manually delineated in the last dynamic (showing the largest contrast) using an ROI drawing tool. Subsequently, the functional share from MRI (FS MRI) was calculated as the summed Ki values in the FRL divided by the sum of Ki values over all voxels of the liver. Additionally, the FRL function from MRI was calculated as mean Ki in the delineated FRL region (fKi). Similarly, the mean maximum enhancement and maximum slope of increase were calculated over the FRL region.

6.2.4. BIOCHEMICAL PARAMETERS

Blood samples were collected immediately before the MRI scan for routine laboratory evaluation of aspartate aminotransferase (AST), aspartate aminotransferase (ALT), bilirubin, albumin, prothrombin time (PT), INR and creatinine.

6.2.5. STATISTICAL ANALYSIS

Continuous data were summarized by median and interquartile range (IQR) if not-normally distributed and as mean and standard deviation (SD) when normally distributed. Discrete variables were expressed as absolute numbers and relative frequencies. Pearson rank correlation was performed to analyze the relation between normally distributed variables. Reproducibility was assessed using intra-class correlation coefficient (absolute agreement, single measures, two-way mixed) and by a Bland-Altman plot. Statistical analysis was per-

formed with IBM SPSS Statistics (version 24.0; IBM Corp., New York, USA).

6.3. RESULTS

6.3.1. PATIENTS

Between December 2014 and July 2018, 20 patients underwent DHCE-MRI within 2 weeks of the ^{99m}Tc-mebrofenin HBS. Patient characteristics are presented in Table 6.1. The median (IQR) time between HBS and MRI was 5 (2-10) days.

Table 6.1: Patient characteristics.

Variable	n = 20
Age, median (IQR)	64 (57 – 70)
Male sex, n (%)	12 (67%)
BMI, kg/m^2, median (IQR)	22.5 (21.3 – 28.2)
BSA, m^2, median (IQR)	1.9 (1.7 – 2.1)
Diagnosis, n (%)	
Colorectal liver metastasis	9 (45 %)
Biliary tumor	4 (20 %)
Hepatocellular carcinoma	3 (15 %)
Benign	4 (20 %)
Neo-adjuvant chemotherapy, n (%)	6 (30%)
Preoperative biliary drainage, n (%)	3 (15 %)

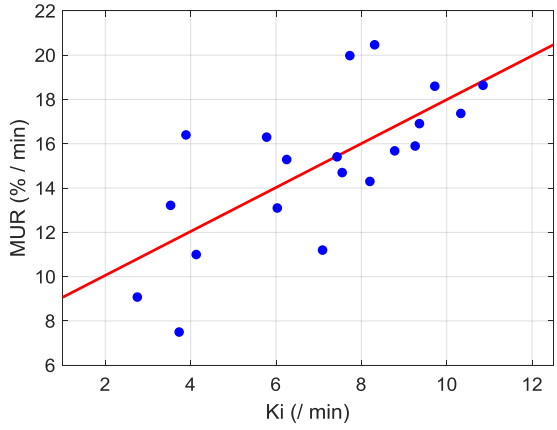

Figure 6.4: Pearson correlation between total liver function represented by the mebrofenin uptake rate (MUR; %/min) and the Gd-EOB-DTPA uptake rate (Ki; min^{-1}).

6.3.2. LIVER FUNCTION

The mean MUR for the total liver averaged over all patients was 15.1 (± 3.4) %/min. The mean Gd-EOB-DTPA uptake rate of the whole liver (Ki) averaged over all patients was 7.0 (± 2.4) per minute. There was a strong correlation between the MUR and Ki (Pearson r = 0.70, P = 0.001, n = 20), see Fig. 6.4.

6.3.3. FUNCTIONAL SHARE AND FUTURE REMNANT LIVER FUNCTION

There was a strong agreement between the functional shares from HBS (FS HBS) and MRI (FS MRI) (ICC = 0.944, 95%-CI: 0.863-0.978, n = 20). A Bland-Altman plot is presented in Fig. 6.5. The mean difference in the functional share between FS HBS and FS MRI was 2.6% and the 95% limit of agreement was ± 14.3%.

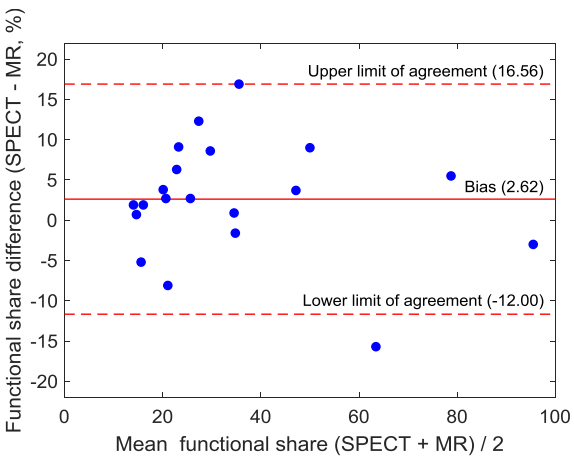

Figure 6.5: Bland-Altman plot for the agreement between functional share (%) of the FRL measured with SPECT and MRI.

Additionally, there was a strong correlation between the FRL function measured from HBS (fMUR) and MRI (fKi) (Pearson r = 0.89, P < 0.001, n = 20), see Fig. 6.6.

6.3.4. BIOCHEMICAL PARAMETERS

Blood samples were taken from all patients. In one patient albumin and PT could not be determined and in three patients INR could not be obtained, due to failing processing of the blood samples. Total serum bilirubin was marginally elevated in three patients (32, 34 and 42 µmol/L respectively). There was a negative correlation between ASAT, ALAT and bilirubin for both MUR and Ki, as shown in Table 6.2.

6.3.5. SEMI-QUANTITATIVE PARAMETERS

There was a moderate correlation between RE and the MUR (Pearson r = 0.473, P = 0.039, n = 20). Furthermore, there was no significant correlation between the mean MSI and the MUR (Pearson r = -0.380, P = 0.098, n = 20).

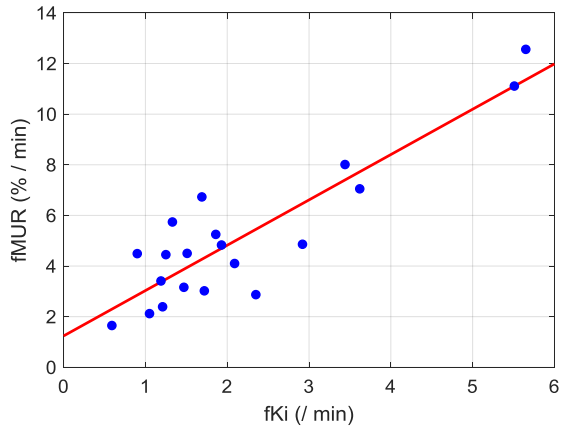

Figure 6.6: Pearson correlation between future remnant liver function represented by the mebrofenin uptake rate (fMUR; %/min) and the Gd-EOB-DTPA uptake rate (fKi; min^{-1}).

Table 6.2: Pearson correlation between blood parameters and MUR and Ki.

		AST	ALT	Bilirubin	Albumin	PT	INR	Creatinine
MUR	*r*	**-0.656**	**-0.530**	**-0.776**	0.224	-0.144	-0.217	-0.325
	P	**0.002**	**0.002**	**<0.001**	0.356	0.557	0.403	0.161
	n	20	20	20	19	19	17	20
Ki	*r*	**-0.603**	**-0.525**	**-0.633**	-0.01	-0.059	-0.063	-0.215
	P	**0.005**	**0.017**	**0.003**	0.968	0.810	0.811	0.362
	n	20	20	20	19	19	17	20

6.4. DISCUSSION

IN this study we demonstrated that there was a strong correlation between liver function measured with the mebrofenin uptake rate (MUR) derived from ^{99m}Tc-mebrofenin HBS and the mean Ki from DHCE-MRI in patients with planned liver resection. Furthermore, there was a strong agreement between the functional share of the FRL, measured with the SPECT-CT and MRI, yielding comparable calculations of the FRL function for both modalities.

Geisel *et al.* compared in an earlier study the liver function measured with HBS and MRI of the left and right liver lobes in patients undergoing portal vein embolization [37]. They showed a moderate to strong correlation between both the relative enhancement and the hepatic uptake index on MRI and mebrofenin uptake in HBS.

In this study we assessed the total liver function using HBS and calculated the functional fraction of the FRL using SPECT, similar to clinical practice. This method is suitable for the preoperative assessment of surgical candidates. Sourbron's model provided a quantification of the uptake rate of Gd-EOB-DTPA which is comparable to the uptake rate of mebrofenin. To our knowledge, this is the first study to compare the functional

distribution of liver function between HBS and MRI.

For the evaluation of liver function, we rely on the hepatic uptake of liver specific agents. This uptake depends on liver perfusion, vascular permeability, extracellular diffusion and hepatocyte transport, which parameters are taken into account in Sourbron's model. Clearly, all these parameters can be altered during liver disease. We hypothesize that by explicitly taking them into account into Sourbron's model, Ki yielded improved (strong) correlation with MUR over the semi-quantitative parameters. Specifically, we found only moderate, correlation between RE and MUR while the correlation between MSI and MUR was not significant.

The MUR is calculated as the percentage of total administered ^{99m}Tc-mebrofenin activity accredited by the liver per minute as described by Ekman *et al.* This calculation is conducted over a period of 150 to 350 seconds after injection (between homogenous distribution in the blood pool and before hepatic excretion in bile ducts). Mebrofenin is administered in tracer amounts such that the hepatic uptake receptors never reach saturation. Practically, this makes Ekman's method less susceptible to alterations in blood flow.

There are several similarities in pharmacokinetic properties between mebrofenin and Gd-EOB-DTPA, in particular, the uptake and excretion by the same transporters [38, 39]. Accordingly, multiple studies have shown that the liver enhancement effects of Gd-EOB-DPTA, which were (semi)-quantitatively assessed, depend on liver function [23, 40, 41]. The main difference between both substances is that mebrofenin is exclusively excreted by the liver, whereas approximately 50% of the injected Gd-EOB-DTPA dose is taken up by the hepatocytes and about 50% is excreted through the renal system (assuming normal organ function) [42]. In the absence of adequate biliary excretion, the urinary excretion pathway can compensate for any deficient hepatic transport mechanism [43, 44]. Renal excretion was found to be increased in patients with severe hepatic impairment. Even in that case however, a high hepatic signal has been observed, which was adequate to quantitatively assess liver function using Gd-EOB-DPTA [44].

Several pharmacokinetic models have been proposed to estimate liver function from DHCE-MRI. Nilsson *et al.* applied a technique called truncated singular value decomposition (TSVD) in order to estimate pharmacokinetic properties [45]. However, this approach regarded the hepatic artery as the sole input, and ignored the portal vein. Sourbron *et al.* created a dual-input, two-compartmental model that accounted for Gd-EOB-DTPA metabolization by the hepatic cells in 2012 [29]. One limitation of this model is that it ignores the extraction rate of hepatocytes, i.e. the efflux to the bile canaliculi. To solve this, Ulloa *et al.* modeled the transport of the contrast agent from the hepatocytes to the bile via so-called Michaelis-Menten kinetics in humans [46]. Alternatively, Georgiou *et al.* modified the efflux transport component of this model by a simpler approximation [47]. Recently, Ning *et al.* correlated pharmacokinetic parameters estimated from different models with a blood chemistry test [48]. They report that the relative liver uptake rate estimated from the model without bile efflux transport correlated with direct bilirubin (r = -0.52, P = 0.015), prealbumin (r = 0.58, P = 0.015) and prothrombin time (r = -0.51, P = 0.026). Furthermore, only insignificant correlations were found using the model with efflux transport. For this reason, in our work we applied COS-FLAC, the model described in Chapter 4, which is based on Sourbron's model, i,e, without bile efflux transport.

A variety of biochemical blood tests reflect the numerous functions of the liver. We focused on ALT and AST levels which reflect liver damage or hepatotoxicity, coagulation parameters like PT and INR and the protein albumin that reflect synthesis function. Serum bilirubin is generally considered the most potent prognostic marker for liver disease and has been used in numerous prognostic models [49, 50]. We found moderate to strong correlations between the hepatic uptake of both mebrofenin and Gd-EOB-DTPA and AST, ALT and serum bilirubin. This confirms earlier findings [51, 52].

During hyperbilirubinema, which is often the case in patients with obstructive biliary tumors, there is competitive uptake of mebrofenin/Gd-EOB-DTPA and bilirubin by the hepatocytes due to the binding to the same receptor. This could explain the strong negative correlations between plasma bilirubin and the uptake of both Gd-EOB-DTPA and mebrofenin in this cohort. Furthermore, during cholestasis, efflux of bile through the MRP2 receptors is impaired which can further contribute to the decreased Gd-EOB-DTPA uptake. This was observed in three of our patients.

The absence of correlation between albumin and coagulation parameters might be explained by insufficient power (due to the small patient population) and the absence of patients with severely impaired liver function.

In several centers, HBS is currently the reference test for the preoperative evaluation of FRL function in patients undergoing liver resection. A disadvantage of this technique is (despite the relatively low radiation burden) the relatively low spatial resolution, making it not feasible as a diagnostic modality for the differentiation of liver lesions. Contrary, the best available imaging tool for lesion characterization is standard contrast-enhanced MRI with multiple contrast phases (pre-contrast, arterial, portal-venous, late venous, delayed and optionally the hepatobiliary phase). With conventional MR imaging techniques, DHCE-MRI cannot be combined with the standard contrast-enhanced scans, one performs either of the two scan types. New developments in the field of MRI sequence engineering now offer the possibility to acquire data continuously in free breathing using a radial acquisition scheme [53, 54]. When performed before and during contrast administration, the raw data can be reconstructed into different data sets: (1) the standard contrast phases optimally timed for each subject as the inflow of contrast-enhanced blood into the liver can be observed and (2) a dynamic contrast-enhanced data set for time-intensity curve and/or pharmacokinetic analysis. While this has not yet been evaluated, the application of such a radial acquisition in this patient group could provide a one-stop-shop modality where patients undergo one scan for both characterization of underlying liver disease and evaluation of (future remnant) liver function.

In addition to lesion characterization, MRI facilitates evaluation of fibrosis, steatosis and micro-perfusion levels of the hepatic tissue as well as assessment of bile duct disease [55–57]. These parameters were not measured in our cohort because most patients had relatively normal (global) liver function without great variation in fibrosis or steatosis grade. Future studies could focus on the relation between Gd-EOB-DTPA uptake and fibrosis or steatosis grade assessed with histopathological quantification of liver biopsies.

One limitation of the applied MRI protocol was that the patients were instructed to hold their breath at several time-points. We did so to avoid movement artifacts during image acquisition, especially at the time points corresponding to the arterial, portal-venous and late venous phases. A free breathing DHCE-sequence, for example with a radial acqui-

sition scheme, should be studied in the future in order to reduce the burden on patients.

Another limitation of this study is the rather small variation in liver function in our cohort. A larger variation would potentially yield an increase of the correlation between HBS and MRI. The small sample size might also result in insufficient power to detect a significant correlation with other blood samples like coagulation parameters. Future studies in a different study population, including patients with chronic and diffuse liver disease that have a wider range of liver function should be conducted to make these findings more robust.

We did not perform an exact sample size calculation (a power analysis), since there was no previous data available on the correlation between Sourbron's model parameters and MUR. We anticipate that our data can form the basis for sample size calculation for a larger prospective, observational cohort study.

In conclusion, assessment of liver function with DHCE-MRI is comparable with that of ^{99m}Tc-mebrofenin HBS. If future studies confirm these findings and new free-breathing scan techniques can be applied successfully, DHCE-MRI could provide a one-stop-shop modality for the preoperative assessment of patients undergoing liver surgery.

REFERENCES

[1] F. Rassam, T. Zhang, K. P. Cieslak, C. Lavini, J. Stoker, R. J. Bennink, T. M. van Gulik, L. J. van Vliet, J. H. Runge, and F. M. Vos, *Comparison between dynamic gadoxetate-enhanced mri and 99mtc-mebrofenin hepatobiliary scintigraphy with spect for quantitative assessment of liver function,* European Radiology (2019), 10.1007/s00330-019-06029-7.

[2] S. Agrawal and J. Belghiti, *Oncologic resection for malignant tumors of the liver,* Annals of Surgery **253**, 656 (2011).

[3] W. R. Jarnagin, M. Gonen, Y. Fong, R. P. DeMatteo, L. Ben-Porat, S. Little, C. Corvera, S. Weber, and L. H. Blumgart, *Improvement in perioperative outcome after hepatic resection,* Annals of Surgery **236**, 397 (2002).

[4] M. A. J. V. D. Broek, S. W. M. O. Damink, C. H. C. Dejong, H. Lang, M. Malagó, R. Jalan, and F. H. Saner, *Liver failure after partial hepatic resection: definition, pathophysiology, risk factors and treatment,* Liver International **28**, 767 (2008).

[5] J. Belghiti, K. Hiramatsu, S. Benoist, P. P. Massault, A. Sauvanet, and O. Farges, *Seven hundred forty-seven hepatectomies in the 1990s: an update to evaluate the actual risk of liver resection11no competing interests declared.* Journal of the American College of Surgeons **191**, 38 (2000).

[6] C. Laurent, A. S. Cunha, P. Couderc, E. Rullier, and J. Saric, *Influence of postoperative morbidity on long-term survival following liver resection for colorectal metastases,* British Journal of Surgery **90**, 1131 (2003).

[7] C. Yigitler, *The small remnant liver after major liver resection: How common and how relevant?* Liver Transplantation **9**, S18 (2003).

[8] M. Shoup, *Volumetric analysis predicts hepatic dysfunction in patients undergoing major liver resection,* Journal of Gastrointestinal Surgery **7**, 325 (2003).

[9] P. Clavien, *Protection of the liver during hepatic surgery,* Journal of Gastrointestinal Surgery **8**, 313 (2004).

[10] A. Guglielmi, A. Ruzzenente, S. Conci, A. Valdegamberi, and C. Iacono, *How much remnant is enough in liver resection?* Digestive Surgery **29**, 6 (2012).

[11] W. de Graaf, K. P. van Lienden, S. Dinant, J. J. T. H. Roelofs, O. R. C. Busch, D. J. Gouma, R. J. Bennink, and T. M. van Gulik, *Assessment of future remnant liver function using hepatobiliary scintigraphy in patients undergoing major liver resection,* Journal of Gastrointestinal Surgery **14**, 369 (2009).

[12] G. Ghibellini, E. M. Leslie, G. M. Pollack, and K. L. R. Brouwer, *Use of tc-99m mebrofenin as a clinical probe to assess altered hepatobiliary transport: Integration of in vitro, pharmacokinetic modeling, and simulation studies,* Pharmaceutical Research **25**, 1851 (2008).

[13] R. J. Bennink, M. Tulchinsky, W. de Graaf, Z. Kadry, and T. M. van Gulik, *Liver function testing with nuclear medicine techniques is coming of age,* Seminars in Nuclear Medicine **42**, 124 (2012).

[14] W. de Graaf, S. Häusler, M. Heger, T. M. van Ginhoven, G. van Cappellen, R. J. Bennink, G. A. Kullak-Ublick, R. Hesselmann, T. M. van Gulik, and B. Stieger, *Transporters involved in the hepatic uptake of 99mtc-mebrofenin and indocyanine green,* Journal of Hepatology **54**, 738 (2011).

[15] W. de Graaf, K. P. van Lienden, T. M. van Gulik, and R. J. Bennink, *99mtc-mebrofenin hepatobiliary scintigraphy with SPECT for the assessment of hepatic function and liver functional volume before partial hepatectomy,* Journal of Nuclear Medicine **51**, 229 (2010).

[16] K. Cieslak, R. Bennink, W. de Graaf, M. Besselink, O. Busch, D. Gouma, and T. van Gulik, *Assessment of liver function in patients undergoing major liver resection using hepatobiliary scintigraphy,* HPB **18**, e713 (2016).

[17] D. Erdogan, B. H. Heijnen, R. J. Bennink, M. Kok, S. Dinant, I. H. Straatsburg, D. J. Gouma, and T. M. van Gulik, *Preoperative assessment of liver function: a comparison of 99mtc-mebrofenin scintigraphy with indocyanine green clearance test,* Liver International **24**, 117 (2004).

[18] S. Dinant, W. de Graaf, B. J. Verwer, R. J. Bennink, K. P. van Lienden, D. J. Gouma, A. K. van Vliet, and T. M. van Gulik, *Risk assessment of posthepatectomy liver failure using hepatobiliary scintigraphy and CT volumetry,* Journal of Nuclear Medicine **48**, 685 (2007).

[19] G. SCHUHMANN-GIAMPIERI, *Liver contrast media for magnetic resonance imaging interrelations between pharmacokinetics and imaging,* Investigative Radiology **28**, 753 (1993).

[20] S. A. SCHMITZ, A. MÜHLER, S. WAGNER, and K.-J. WOLF, *Functional hepatobiliary imaging with gadolinium-EOB-DTPA,* Investigative Radiology **31**, 154 (1996).

[21] T. Kim, T. Murakami, Y. Hasuike, M. Gotoh, N. Kato, M. Takahashi, T. Miyazawa, Y. Narumi, M. Monden, and H. Nakamura, *Experimental hepatic dysfunction: Evaluation by MRI with gd-EOB-DTPA,* Journal of Magnetic Resonance Imaging **7**, 683 (1997).

[22] J. Shimizu, K. Dono, M. Gotoh, Y. Hasuike, T. Kim, T. Murakami, M. Sakon, K. Umeshita, H. Nagano, S. Nakamori, N. Kato, T. Miyazawa, H. Nakamura, and M. Monden, *Evaluation ofreginal liver function by gadolinium-EOB-DTPA enhanced MR imaging,* Gastroenterology **114**, A1342 (1998).

[23] H.-K. Ryeom, S.-H. Kim, J.-Y. Kim, H.-J. Kim, J.-M. Lee, Y.-M. Chang, Y.-S. Kim, and D.-S. Kang, *Quantitative evaluation of liver function with MRI using gd-EOB-DTPA,* Korean Journal of Radiology **5**, 231 (2004).

[24] N. Tsuda, M. Okada, and T. Murakami, *Potential of gadolinium-ethoxybenzyl-diethylenetriamine pentaacetic acid (gd-EOB-DTPA) for differential diagnosis of non-alcoholic steatohepatitis and fatty liver in rats using magnetic resonance imaging,* Investigative Radiology **42**, 242 (2007).

[25] N. Tsuda, M. Okada, and T. Murakami, *New proposal for the staging of nonalcoholic steatohepatitis: Evaluation of liver fibrosis on gd-EOB-DTPA-enhanced MRI,* European Journal of Radiology **73**, 137 (2010).

[26] M. C. Niekel, S. Bipat, and J. Stoker, *Diagnostic imaging of colorectal liver metastases with CT, MR imaging, FDG PET, and/or FDG PET/CT: A meta-analysis of prospective studies including patients who have not previously undergone treatment,* Radiology **257**, 674 (2010).

[27] X. Liu, H. Jiang, J. Chen, Y. Zhou, Z. Huang, and B. Song, *Gadoxetic acid disodium-enhanced magnetic resonance imaging outperformed multidetector computed tomography in diagnosing small hepatocellular carcinoma: A meta-analysis,* Liver Transplantation **23**, 1505 (2017).

[28] Y. E. Chung, M.-J. Kim, Y.-E. Kim, M.-S. Park, J. Y. Choi, and K. W. Kim, *Characterization of incidental liver lesions: Comparison of multidetector CT versus gd-EOB-DTPA-enhanced MR imaging,* PLoS ONE **8**, e66141 (2013).

[29] S. Sourbron, W. H. Sommer, M. F. Reiser, and C. J. Zech, *Combined quantification of liver perfusion and function with dynamic gadoxetic acid–enhanced MR imaging,* Radiology **263**, 874 (2012).

[30] M. F. Forsgren, O. D. Leinhard, N. Dahlström, G. Cedersund, and P. Lundberg, *Physiologically realistic and validated mathematical liver model revels hepatobiliary transfer rates for gd-EOB-DTPA using human DCE-MRI data,* PLoS ONE **9**, e95700 (2014).

[31] H. Nilsson, L. Blomqvist, L. Douglas, A. Nordell, I. Janczewska, E. Näslund, and E. Jonas, *Gd-EOB-DTPA-enhanced MRI for the assessment of liver function and volume in liver cirrhosis,* The British Journal of Radiology **86**, 20120653 (2013).

[32] M. EKMAN, M. FJÄLLING, S. FRIMAN, S. CARLSON, and R. VOLKMANN, *Liver uptake function measured by IODIDA clearance rate in liver transplant patients and healthy volunteers,* Nuclear Medicine Communications **17**, 235 (1996).

[33] M. P. Heinrich, M. Jenkinson, B. W. Papiez, S. M. Brady, and J. A. Schnabel, *Towards realtime multimodal fusion for image-guided interventions using self-similarities,* in *Lecture Notes in Computer Science (including subseries Lecture Notes in Artificial Intelligence and Lecture Notes in Bioinformatics)*, Vol. 8149 LNCS (2013) pp. 187–194.

[34] T. Zhang, Z. Li, J. H. Runge, C. Lavini, J. Stoker, T. van Gulik, L. J. van Vliet, and F. M. Vos, *Improved registration of DCE-MR images of the liver using a prior segmentation of the region of interest,* in *Medical Imaging 2016: Image Processing*, edited by M. A. Styner and E. D. Angelini (SPIE, 2016).

[35] Y. Zhang, B. J. Matuszewski, L.-K. Shark, and C. J. Moore, *Medical image segmentation using new hybrid level-set method,* in *2008 Fifth International Conference BioMedical Visualization: Information Visualization in Medical and Biomedical Informatics* (IEEE, 2008).

[36] S. Aronhime, C. Calcagno, G. H. Jajamovich, H. A. Dyvorne, P. Robson, D. Dieterich, M. I. Fiel, V. Martel-Laferriere, M. Chatterji, H. Rusinek, and B. Taouli, *DCE-MRI of the liver: Effect of linear and nonlinear conversions on hepatic perfusion quantification and reproducibility,* Journal of Magnetic Resonance Imaging **40**, 90 (2013).

[37] D. Geisel, L. Lüdemann, V. Fröling, M. Malinowski, M. Stockmann, A. Baron, B. Gebauer, D. Seehofer, V. Prasad, and T. Denecke, *Imaging-based evaluation of liver function: comparison of 99mtc-mebrofenin hepatobiliary scintigraphy and gd-EOB-DTPA-enhanced MRI,* European Radiology **25**, 1384 (2014).

[38] M. Leonhardt, M. Keiser, S. Oswald, J. Kuhn, J. Jia, M. Grube, H. K. Kroemer, W. Siegmund, and W. Weitschies, *Hepatic uptake of the magnetic resonance imaging contrast agent gd-EOB-DTPA: Role of human organic anion transporters,* Drug Metabolism and Disposition **38**, 1024 (2010).

[39] B. E. V. Beers, C. M. Pastor, and H. K. Hussain, *Primovist, eovist: What to expect?* Journal of Hepatology **57**, 421 (2012).

[40] T. Tajima, H. Takao, H. Akai, S. Kiryu, H. Imamura, Y. Watanabe, J. Shibahara, N. Kokudo, M. Akahane, and K. Ohtomo, *Relationship between liver function and liver signal intensity in hepatobiliary phase of gadolinium ethoxybenzyl diethylenetriamine pentaacetic acid-enhanced magnetic resonance imaging,* Journal of Computer Assisted Tomography **34**, 362 (2010).

[41] N. Verloh, M. Haimerl, J. Rennert, R. Müller-Wille, C. Nießen, G. Kirchner, M. Scherer, A. Schreyer, C. Stroszczynski, C. Fellner, and P. Wiggermann, *Impact of liver cirrhosis on liver enhancement at gd-EOB-DTPA enhanced MRI at 3tesla,* European Journal of Radiology **82**, 1710 (2013).

[42] B. Hamm, T. Staks, A. Mühler, M. Bollow, M. Taupitz, T. Frenzel, K. J. Wolf, H. J. Weinmann, and L. Lange, *Phase i clinical evaluation of gd-EOB-DTPA as a hepatobiliary MR contrast agent: safety, pharmacokinetics, and MR imaging.* Radiology **195**, 785 (1995).

[43] A. Muhler, R. P. J. O. Elferink, and H.-J. Weinmann, *Complete elimination of the hepatobiliary mr contrast agent gd-EOB-DTPA in hepatic dysfunction: An experimental study using transport-deficient, mutant rats,* MAGMA Magnetic Resonance Materials in Physics, Biology, and Medicine **1**, 134 (1993).

[44] S. Gschwend, W. Ebert, M. Schultze-Mosgau, and J. Breuer, *Pharmacokinetics and imaging properties of gd-EOB-DTPA in patients with hepatic and renal impairment,* Investigative Radiology **46**, 556 (2011).

[45] H. Nilsson, A. Nordell, R. Vargas, L. Douglas, E. Jonas, and L. Blomqvist, *Assessment of hepatic extraction fraction and input relative blood flow using dynamic hepatocyte-specific contrast-enhanced MRI,* Journal of Magnetic Resonance Imaging **29**, 1323 (2009).

[46] J. L. Ulloa, S. Stahl, J. Yates, N. Woodhouse, J. G. Kenna, H. B. Jones, J. C. Waterton, and P. D. Hockings, *Assessment of gadoxetate DCE-MRI as a biomarker of hepatobiliary transporter inhibition,* NMR in Biomedicine **26**, 1258 (2013).

[47] L. Georgiou, J. Penny, G. Nicholls, N. Woodhouse, F.-X. Blé, P. L. H. Cristinacce, and J. H. Naish, *Quantitative assessment of liver function using gadoxetate-enhanced magnetic resonance imaging,* Investigative Radiology **52**, 111 (2017).

[48] J. Ning, Z. Yang, S. Xie, Y. Sun, C. Yuan, and H. Chen, *Hepatic function imaging using dynamic gd-EOB-DTPA enhanced MRI and pharmacokinetic modeling,* Magnetic Resonance in Medicine **78**, 1488 (2016).

[49] R. N. H. Pugh, I. M. Murray-Lyon, J. L. Dawson, M. C. Pietroni, and R. Williams, *Transection of the oesophagus for bleeding oesophageal varices,* British Journal of Surgery **60**, 646 (1973).

[50] P. Kamath, *A model to predict survival in patients with end-stage liver disease,* Hepatology **33**, 464 (2001).

[51] G. M. Kukuk, S. G. Schaefer, R. Fimmers, D. R. Hadizadeh, S. Ezziddin, U. Spengler, H. H. Schild, and W. A. Willinek, *Hepatobiliary magnetic resonance imaging in patients with liver disease: correlation of liver enhancement with biochemical liver function tests,* European Radiology **24**, 2482 (2014).

[52] E. Talakic, J. Steiner, P. Kalmar, A. Lutfi, F. Quehenberger, U. Reiter, M. Fuchsjäger, and H. Schöllnast, *Gd-EOB-DTPA enhanced MRI of the liver: Correlation of relative hepatic enhancement, relative renal enhancement, and liver to kidneys enhancement ratio with serum hepatic enzyme levels and eGFR,* European Journal of Radiology **83**, 607 (2014).

[53] L. Feng, L. Axel, H. Chandarana, K. T. Block, D. K. Sodickson, and R. Otazo, *XD-GRASP: Golden-angle radial MRI with reconstruction of extra motion-state dimensions using compressed sensing,* Magnetic Resonance in Medicine **75**, 775 (2015).

[54] L. Feng, R. Grimm, K. T. Block, H. Chandarana, S. Kim, J. Xu, L. Axel, D. K. Sodickson, and R. Otazo, *Golden-angle radial sparse parallel MRI: Combination of compressed sensing, parallel imaging, and golden-angle radial sampling for fast and flexible dynamic volumetric MRI,* Magnetic Resonance in Medicine **72**, 707 (2013).

[55] H. S. Park, *Three-tesla magnetic resonance elastography for hepatic fibrosis: Comparison with diffusion-weighted imaging and gadoxetic acid-enhanced magnetic resonance imaging,* World Journal of Gastroenterology **20**, 17558 (2014).

[56] Y. Ding, S.-X. Rao, T. Meng, C. Chen, R. Li, and M.-S. Zeng, *Usefulness of t1 mapping on gd-EOB-DTPA-enhanced MR imaging in assessment of non-alcoholic fatty liver disease,* European Radiology **24**, 959 (2014).

[57] N. K. Lee, S. Kim, J. W. Lee, S. H. Lee, D. H. Kang, G. H. Kim, and H. I. Seo, *Biliary MR imaging with gd-EOB-DTPA and its clinical applications,* RadioGraphics **29**, 1707 (2009).

7

Conclusion and Future work

7.1. CONCLUSIONS

PATIENTS with colorectal cancer are frequently presented with liver metastases for which (partial) resection is often the best therapy. However, the future remnant liver, the remaining part of the liver after resection, should allow adequate liver function to avoid liver failure. This thesis presents methods for the accurate voxel-wise estimation of the future remnant liver's function based on pharmacokinetic modeling of dynamic contrast-enhanced (DCE) MRI. It presents several novel techniques regarding registration, segmentation as well as pharmacokinetic modeling of DCE-MRI data of the liver. In addition, the relation of DCE MRI of the liver and hepatobiliary scintigraphy was studied.

In this chapter, the contributions of the previous chapters are highlighted. Moreover, potentially future work will be discussed.

7.1.1. REGISTRATION

In **Chapter** 2, the registration framework proposed by us integrated a liver segmentation into the ALOST registration framework [1]. The prior segmentation supported ALOST in restricting the search space. The improved registration was demonstrated by better fits of Sourbron's model to the time intensity data after registration. The proposed framework can be easily adapted to other DCE-MRI applications with different contrast agents provided that a segmentation of the organ of interest is available.

In **Chapter** 3, two novel frameworks for 4D registration of DCE MRI data were proposed to reduce the sensitivity of image registration methods to local minima in the objective function. The first framework **S**orting **V**olumes **A**ccording to **D**isplacement (SVAD) imposed an ordering to the images by increasing distance in the superior-inferior direction with respect to a reference image. Subsequently, the images were sequentially registered to the reference image starting with the images with the shortest distance. Hypothetically, the registration of an image was initialized close to the global optimum by combining its registration to the preceding image with the registration of the latter to the reference. The second framework **O**ptimizing **S**tarting **P**oints **A**ccording to **R**obust **F**itting (OSPARF) assumed a linear relation between the mean relative displacement of the liver and the displacement of individual points in the liver. It also aimed to initialize the registration close to the global optimum by iteratively adjusting the initial registration based on this assumed relation. The proposed methods were compared to two state-of-the-art methods that also try to avoid getting trapped in a local minimum. The performance of the registration methods was quantitatively assessed using the residual after fitting of a pharmacokinetic model and the target registration error on synthetically deformed images. The proposed methods outperformed the existing methods in all but a minority of cases. Furthermore, the OSPARF method appeared to have a slight edge over SVAD, although the difference was not large.

7.1.2. SEGMENTATION

In **Chapter** 2 - 4, a segmentation method based on the so-called contrast enhancement map was adopted to segment the liver. As we apply a liver-specific contrast agent, the surrounding organs show less signal enhancement than the liver. Maximal contrast was achieved by subtracting the registered first image of the series from the last image. Subsequently, the liver was segmented based on the resulting "contrast" volume by means of a

level set approach.

In **Chapter** 5, a finer segmentation method was proposed to partition the liver from the DCE-MR images. It consists of two steps. In the first step, a region growing method was applied to segment the hepatic vein (HV), the portal vein (PV) and inferior vena cava (IVC) from the liver. In the second step, skeletons of these segmented vessels were regarded as landmarks to partition functional liver segments. Comparison with state-of-the-art methods showed that our method produced more accurate segmentations of the vessels in the liver. Moreover, our segmentations of functional liver segment had large overlap (measured through the Dice Coefficient) with a manually annotated reference. The proposed segmentation method can easily be adapted to other DCE-MRI or DCE-CT applications with low spatial resolution.

7.1.3. PHARMACOKINETIC MODELING

In **Chapter** 4, we proposed an improved pharmacokinetic model for DCE-MRI of the liver. The novelties of our work comprised:

1) Analytical voxel-wise modeling of the arrival-time of the contrast agent. Orton's model was adopted to represent the liver's dual input functions (hepatic artery and portal vein) and embed them into Sourbron's model. The combined Orton and Sourbron (COS) model was shown to enhance the fitting accuracy as well as the efficiency of the model fitting.

2) Compensation for effects that can be modeled by varying applied flip-angle, e.g. B1-inhomogeneity. A flip-angle potentially deviating from its nominal value due to this effect was modeled by taking into account the displacement of a liver voxel with respect to the first image.

We referred to the approach combining both of the aforementioned novelties as the COS-FLAC model. The validity of our approach was supported by the moderate to strong linear correlation between displacement and deviation in flip angle. The COS-FLAC model was quantitatively assessed by the root mean square error (RMSE) of the residue that remained after fitting the model to the signal in every voxel of the liver. We found that the COS-FLAC model achieved significantly lower RMSE than the COS approach. Furthermore, three model complexity criteria showed that the COS-FLAC model outperformed the COS model in the vast majority of voxels.

7.1.4. CLINICAL FEASIBILITY

In **Chapter** 6, DCE-MRI perfusion parameter liver uptake rate (Ki) derived from our COS-FLAC model with Gd-EOB-DTPA was correlated with the corresponding liver uptake rate (MUR) in ^{99m}Tc-Mebrofenin Hepatobiliary Scintigraphy with SPECT. Strong correlations were found between uptake parameters derived from DCE-MRI and HBS for both total and FRL function (Pearson $r = 0.70$, $P = 0.001$ and $r = 0.89$, $P < 0.001$ respectively). There was a strong agreement between the functional share determined with both modalities (ICC = 0.944, 95%-CI: 0.863-0.978, n = 20). There was a significant negative correlation between liver aminotransferases and bilirubin for both MUR and Ki. The results indicate that DCE-MRI with Gd-EOB-DTPA has the potential to quantitatively measure functional features of the liver.

7.2. FUTURE WORK

DEEP learning has gained enormous popularity in recent years. It is a form of machine learning that enables computers to learn from experience represented by large amounts of annotated data and understand the world in terms of a hierarchy of concepts [1]. Unlike conventional machine-learning techniques, which were limited in their ability to process natural data in their raw form, deep learning is able to learn complicated concepts by building them out of a deep-layered graph of these hierarchies without explicitly transforming the raw data into a suitable internal representation or feature vector [2]. Applying deep learning to DCE-MRI of the liver is interesting and promising. The following topics may be expanded upon in the future.

7.2.1. REGISTRATION

When performing registration, one of the key steps is to design a similarity metric to extract features in corresponding images, which typically requires careful engineering and considerable domain expertise. It might be possible to adopt deep-learning networks to estimate a similarity measures for images to drive an iterative optimization strategy [2]. Alternatively, deep-learning networks could be directly applied to predict transformation parameters [3]. Moreover, with the help of parallel computing in multi-GPUs, it may be possible to realize real-time training of the network.

7.2.2. SEGMENTATION

The deep learning techniques to achieve segmentations can be mainly divided into two categories: convolutional neural network (CNN) and recurrent neural network (RNN). Deep convolutional nets have brought breakthroughs in processing images, video, speech and audio, whereas recurrent nets are often applied to sequential data such as text and speech [4].

1) CNN- backbone methods. Semantic segmentation is one of the key problems in the field of computer vision. It describes the process of associating each pixel of an image with a class label. Many networks have been proposed to do so, such as U-Net [5], SegNet [6], DeepLab [7] and RefineNet [8]. In the biomedical imaging field, segmenting organs of interest in 3D volumes is a challenging task. Quasi- 3D [9] and fully 3D [10] U-Nets have been used to solve this problem. Common inputs for such neural networks are gray-scale images or RGB images (three channels). However, our DCE-MR images are 4D data, i.e. 3D+t (108 dynamics). Upon registration of the DCE series, 108 dynamics can be regarded as 108 channels. Integrating 108 channels into a proper deep neural network might contribute to the segmentation performance.

2) RNN-backbone methods. As mentioned above, our 4D DCE-MRI data is a time series. For each voxel in the abdomen, a Time Intensity Curve (TIC) can be extracted and different profiles correspond to different kinds of tissues / organs. As such, segmenting tissues / organs can be regarded as a sequence classification problem. A popular approach for sequence classification is a gated recurrent network like the Gated Recurrent Units (GRU) approach [11] and the Long Short-Term Memory (LSTM) configuration [12]. Applying these methods in the field of biomedical imaging might certainly be interesting.

REFERENCES

[1] Z. Li, D. Mahapatra, J. A. W. Tielbeek, J. Stoker, L. J. Van Vliet, and F. M. Vos, *Image Registration Based on Autocorrelation of Local Structure,* IEEE Transactions on Medical Imaging **35**, 63 (2016).

[2] X. Cheng, L. Zhang, and Y. Zheng, *Deep similarity learning for multimodal medical images,* Computer Methods in Biomechanics and Biomedical Engineering: Imaging & Visualization **6**, 248 (2016).

[3] S. Miao, Z. J. Wang, and R. Liao, *A CNN regression approach for real-time 2d/3d registration,* IEEE Transactions on Medical Imaging **35**, 1352 (2016).

[4] Y. LeCun, Y. Bengio, and G. Hinton, *Deep learning,* Nature **521**, 436 (2015).

[5] O. Ronneberger, P. Fischer, and T. Brox, *U-net: Convolutional networks for biomedical image segmentation,* in *Lecture Notes in Computer Science* (Springer International Publishing, 2015) pp. 234–241.

[6] V. Badrinarayanan, A. Kendall, and R. Cipolla, *SegNet: A deep convolutional encoder-decoder architecture for image segmentation,* IEEE Transactions on Pattern Analysis and Machine Intelligence **39**, 2481 (2017).

[7] L.-C. Chen, G. Papandreou, I. Kokkinos, K. Murphy, and A. L. Yuille, *DeepLab: Semantic image segmentation with deep convolutional nets, atrous convolution, and fully connected CRFs,* IEEE Transactions on Pattern Analysis and Machine Intelligence **40**, 834 (2018).

[8] G. Lin, A. Milan, C. Shen, and I. Reid, *RefineNet: Multi-path refinement networks for high-resolution semantic segmentation,* in *2017 IEEE Conference on Computer Vision and Pattern Recognition (CVPR)* (IEEE, 2017).

[9] X. Li, H. Chen, X. Qi, Q. Dou, C.-W. Fu, and P.-A. Heng, *H-DenseUNet: Hybrid densely connected UNet for liver and tumor segmentation from CT volumes,* IEEE Transactions on Medical Imaging , 1 (2018).

[10] Özgün Çiçek, A. Abdulkadir, S. S. Lienkamp, T. Brox, and O. Ronneberger, *3d u-net: Learning dense volumetric segmentation from sparse annotation,* in *Medical Image Computing and Computer-Assisted Intervention – MICCAI 2016* (Springer International Publishing, 2016) pp. 424–432.

[11] K. Cho, B. van Merrienboer, D. Bahdanau, and Y. Bengio, *On the properties of neural machine translation: Encoder–decoder approaches,* in *Proceedings of SSST-8, Eighth Workshop on Syntax, Semantics and Structure in Statistical Translation* (Association for Computational Linguistics, 2014).

[12] S. Hochreiter and J. Schmidhuber, *Long short-term memory,* Neural Computation **9**, 1735 (1997).

ACKNOWLEDGEMENTS

It is my greatest pleasure to thank those whose guidance and support have made this thesis possible. First of all, I am deeply indebted to my promoter Prof. **Lucas van Vliet** whose comments and suggestion inspire me greatly. Furthermore, his enthusiasm for research as well as working efficiency have kept me motivated in the past four years. His humor, in particular, has given me so much fun working with him.

I would also like to extend my sincere gratitude to Prof. **Jaap Stoker**, my other promoter, who has made it possible for me to link more to the clinical field. I really appreciate his help and support on my project.

I owe my special thanks to Dr. **Frans Vos** for providing me the access to the medical imaging field as well as to the Netherlands. Medical imaging is a fantastic research area and the Netherlands is a perfect country to study in. I still remember I was a bit shy when having the first progress meeting, he encouraged me by saying, "Chinese students are always too shy to ask questions, and you should be 'annoying'!" Up to now, he must have regretted for encouraging me to be so because I have bothered him so much in the past four years. Thanks to his patience and guidance, I am now able to present ideas and write papers in proper scientific English. Apart from research, he also implicitly encouraged me to practice table tennis by claiming that he was a "Dutch national level" player, although we never had a chance to play together.

I must thank Dr. **Cristina Lavini** for discussing with me about the problems I encountered during my research. Her solid knowledge on MRI, quick response and the ability to switch among Italian, English, German and Dutch have really impressed me a lot. I really enjoy doing my research under her supervision.

My special thanks also go to all the collaborators in AMC: **Thormas**, **Roel**, **Jurgen** and **Fadi**. Without their help, the clinical experiment in my research project would have been impossible.

Dozens of people have helped me immensely in QI group. **Jeroen van Schie**, my former officemate has introduced a lot of fundamental knowledge of DCE-MRI to me and shared his code with me. He has also made it possible for me to start a life in the Netherlands by offering timely help and support. **Hamid**, my current officemate, has made our office a perfect to meditate and work. **Jianfei**, my dear friend, the proverb he taught me by Mencius "If you ask someone for help but fail, go back and reflect yourself" has turned out to be my lifelong motto. **Zhang**, his "heritage" about image registration has been a good starting point for my own research. **Boling**, my buddy, has supported me to go through all the tough periods. We have shared so many moments of happiness, worries as well as food. **Yan**, her recipes prove to be necessary for a picky Chinese to survive the Dutch food. All the culture difference talks with **Joor** have become important breaks between the research tasks. **Robert Moerland** has organized fantastic group activities, and the hot pot night will be my treasured memories. All the members in the table soccer club, **Jos**, **Gyllion**, **Leon**, **Jelle van der Horst**, **Pierre**, and **Joost** have made my free time enjoyable

and meaningful. My time spent with **Kedir**, **Mojtaba** and **Nadya** on table tennis has been irreplaceable in helping me getting rid of all the stress. I also want to thank **Lena**, **Jelena**, **Anna**, **Jeroen Heldens**, **Willem**, **Robert Nieuwenhuizen**, **Richard**, **Babak**, **Robiel**, **Tom**, **Juan**, **Muhammad**, **Rasmus**, **Christiaan** and **Jelle Storteboom** for being supportive.

The staffs in QI have been most helpful. **Mandy** has helped me process the admission procedure for my PhD study. **Annelies** has been most patient and efficient in solving all my problems. **Angela** has done a lot during **Annelies**'s absence. **Ronald** has supported me by providing technical help and his strong roar "coffee" as well. **Ron** has been most kind and even helped me find the missing table tennis table in our faculty. **Bernd**, **Sjoerd**, **Ted**, **Jaap Caro**, **Jeroen Kalkman**, **Piet**, **Dirk** have posed inspiring questions and suggestions during the QI seminars.

My dear Chinese fellows in the Netherlands have made my life here full of love and laughter. I have received so much fun and wonderful memories spending time with **Meng** and **Yin**. I will always cherish the time spent with **Fei** and **Jiao** enjoying their hand-made Shaanxi noodles and playing Mahjong. Those long conversations with **Jin** and **Yun** are really hilarious. I also would like to thank **Jin** for his excellent table tennis skill. Many times of 0-11 score make me realize nothing can be even worse and have to be optimistic. It contributes a lot to my survival of the PhD life. **Wenjie** and **Xiangrong** are my role models of excellent researchers. **Junru** and **Xiaolin**, their adorable son and daughter are such soul consoles for me. I had a great time playing cards with **Xinmin** and **Qian**. **Ding** has contributed a lot by recommending job opportunities. **Zhi** has recommended me many kinds of potato chips. **Zhirui** has helped me settle down in Delft. I have benefited a lot from conversations with **Ziyuan** and **Xuan**. I had fun playing table soccer and table tennis with **Junhai**, **Dong** and **Shan**. I learnt a lot from **Zhe**, **Ying**, **Yifeng**, **Zhongwen**, **Zheng**, **Kefei**, **Xukang** and **Min** when I was having lunch with them in Aula. My dear neighbors **Zhao** and **Wenjuan** took good care of my studio while I was on holiday. **Yingguang**, **Qing**, **Rui** and **Puning** have organized the amazing cycle trip to watch the tulips. I also had a good time with **Yuanyuan**, **Yingguang** and **Qing** in Utrecht and Rotterdam to attend the symposiums together.

My family's consistent love and support have been my inner motive to finish the PhD degree. My dear parents have always supported me without any expectation for return. My dear parents-in-law are really understanding and caring. I greatly appreciate my beloved wife's consideration and efforts in maintaining our long-distance marriage. As I am finishing this PhD thesis, a new journey starts ahead of us. I feel so blessed to be able to spend the rest of my life with her (🐻).

Tian ZHANG
Delft, the Netherlands
June, 2018

CURRICULUM VITÆ

Tian ZHANG

03-Oct-1989	Born in Jurong, Zhenjiang, Jiangsu, China.

EDUCATION

2004–2007	High School Jurong High School, Jurong
2007–2011	B.Sc in Optical Information Science & Technology China University of Mining and Technology, Xuzhou, China *Thesis*: "Study on the Coupling Effect of Strong Electromagnetic Pulses in Three-dimensional Structures"
2011–2014	M.Sc in Optical Engineering Zhejiang University, Hangzhou, China *Thesis*: "Enhanced Finite Difference Time Domain (FDTD) Method and Its Application in Dispersive Thin Layer Graphene"
2014–2018	Ph.D in Biomedical Engineering Delft University of Technology, Delft, The Netherlands *Thesis*: "Image Analysis for DCE-MRI of the Liver"

AWARDS

2008	National Scholarship
2009	First Prize Scholarship of the University
2010	National Scholarship
2013	“SCHOTT” Scholarship

List of Publications

1 **T. Zhang**[1], F. Rassam[1], K. P. Cieslak, C. Lavini, J. Stoker, R.J. Bennink, T. van Gulik, L. J. van Vliet, F. M. Vos[2], and J. H. Runge[2], *Comparison Between Dynamic Gadoxetate-enhanced MRI and ^{99m}Tc-mebrofenin Hepatobiliary Scintigraphy with SPECT for Quantitative Assessment of Liver Function*, European Radiology, 0938-7994, 2019.

2 **T. Zhang**, J. H. Runge, C. Lavini, J. Stoker, T. van Gulik, K. P. Cieslak, L. J. van Vliet, and F. M. Vos, *A Pharmacokinetic Model with Separate Arrival Time for Two Inputs and Compensating for Varying Flip-angle in DCE-MRI with Gd-EOB-DTPA*, submitted to PLOS ONE.

3 **T. Zhang**, J. H. Runge, C. Lavini, J. Stoker, T. van Gulik, K. P. Cieslak, L. J. van Vliet, and F. M. Vos, *Improved Initialization Frameworks for 4D Registration of DCE-MR Images of the Liver based on a Prior Segmentation*, submitted to IEEE Transactions on Biomedical Engineering.

4 **T. Zhang**, Z. Wu, J. H. Runge, C. Lavini, J. Stoker, T. van Gulik, L. J. van Vliet, and F. M. Vos, *A Hybrid Segmentation Method for Functional Liver Partition Based on 4D DCE-MR Images*, Proc. SPIE, vol. 10574. pp. 1057434–105741, 2018.

5 **T. Zhang**, Z. Li, J. H. Runge, C. Lavini, J. Stoker, T. van Gulik, L. J. van Vliet, and F. M. Vos, *Improved registration of DCE-MR images of the liver using a prior segmentation of the region of interest*, Proc. SPIE, vol. 9784. pp. 978443–978448, 2016.

[1] These authors contributed equally to this work
[2] These authors are joint last authors